Politecnico di Torino

Department of Mechanical and Aerospace Engineering

Master Degree in Aerospace Engineering

Master Degree Thesis

Development of a Multi-Purpose Helicopter flight simulator

Supervisors:
Elisa Capello
Pierluigi Capone
Anna Abà

Candidate:
Lorenzo Chmet

Academic year 2022 / 2023

Acknowledgements

This thesis project was made possible thanks to several people that guided and supported me and to whom, I would like to express my sincerest gratitude. In particular, I would like to thank:

Prof. Elisa Capello of the Politecnico di Torino, for choosing me as thesis student, giving me the possibility to work on this intriguing project, and following me in every step to support my work

Prof. Pierluigi Capone and *Anna Abà*, of the Zentrum für Aviatik ZAV, Zürcher Hochschule für Angewandte Wissenschaften (Winterthur, Switzerland), for supervising me all the time with patience and dedication, answering every question I asked and feeding my curiosity with their knowledge

Kopter Group, and in particular *Alessandro Masi* and *Francesco Scorcelletti*, for their trust in sharing their stimulating project with me, letting me work on Kopter's fascinating aircraft and supporting me on several occasions

Prisca Dill, of the ZHAW International Office, for taking care of me during all my time abroad, especially during the incoming phase, and guiding me through all the burocracy

Politecnico di Torino and *Zürcher Hochschule für Angewandte Wissenschaften* for their economic support who helped me a lot during my stay in Switzerland for three months

Abstract

This thesis aims to describe the development of a flight simulation model for a multi-purpose helicopter. The model is developed in the Matlab/Simulink environment and also has the target to be integrated into a real-time flight simulator such as the ReDSim of the ZAV Centre for Aviation at ZHAW, Zurich University of Applied Sciences, in Winterthur, Switzerland, a research and development flight simulator employed for both educational and industrial applications. The study mainly focuses on developing a model for the helicopter tail rotor with its shrouded configuration. Nevertheless, a model for the aerodynamic surfaces and the main rotor wake has also been developed. The first part of the work has been dedicated to the modeling of the ducted tail rotor configuration: in particular, in addition to the expected behavior of a typical tail rotor with an open configuration, the challenge was to describe the behavior of the duct and the reciprocal interaction between the duct and the fan. A model for the airframe, the main rotor head, the horizontal stabilizer, and the vertical fin has also been developed to compute the loads generated by these components during the helicopter mission. A wake model was also formulated to describe the main rotor interference on the aerodynamic surfaces and on the tail rotor. In the end, the models developed have been integrated, defining a comprehensive helicopter model. The thesis presented is part of a wider work, whose goal is to develop a high-fidelity simulation model to support engineering activities such as flight control system (FCS) design.

Contents

List of Figures

List of Tables

Nomenclature

θ	Pitch angle	$[rad]$
ψ	Yaw angle	$[rad]$
φ	Roll angle	$[rad]$
α	Angle of attack	$[rad]$
α_0	Zero-lift angle of attack	$[rad]$
α_{diff}	Duct diffuser angle	$[rad]$
β	Flapping angle	$[rad]$
β_{1c}	Longitudinal flapping angle	$[rad]$
β_{1s}	Lateral flapping angle	$[rad]$
χ	Wake angle	$[rad]$
χ_X	Wake angle in the x-axis direction	$[rad]$
χ_Y	Wake angle in the y-axis direction	$[rad]$
δ_{pedal}	Pedal position	$[\%]$
δ_{tip}	Distance between the blade tip and the internal part of the duct	$[m]$
ε_b	Blade tip clearance	$[rad]$
η_{diff}	Diffuser drag factor	$[n/d]$
η_{inlet}	Inlet drag factor	$[n/d]$
λ	Inflow parameter	$[n/d]$
λ_0	Uniform component of inflow parameter	$[n/d]$
λ_{1c}	Longitudinal component of inflow parameter	$[n/d]$
λ_{1s}	Lateral component of inflow parameter	$[n/d]$
μ	Horizontal advance ratio	$[n/d]$
μ_z	Vertical advance ratio	$[n/d]$
ϕ	Inflow angle	$[rad]$
ψ	Blade azimuth angle	$[rad]$

ρ	Air density	$[kg/m^3]$
θ_0	Collective blade pitch angle	$[rad]$
θ_{twist}	Blade twist angle	$[rad]$
Ω_{TR}	Tail rotor angular speed	$[rad/s]$
BL_{CG}	Center of gravity butt-line coordinate	$[m]$
C_F	Force coefficient	$[n/d]$
C_L	Blade section lift coefficient	$[n/d]$
C_M	Moment coefficient	$[n/d]$
C_d	Blade section drag coefficient	$[n/d]$
D_{exit}	Duct diffuser exit diameter	$[m]$
F_a	Thrust along Z_{HUB} produced by a single ring of the tail rotor	$[N]$
I_{pTR}	Tail rotor polar moment	$[kg\,m^2]$
K_1	Pitch-flap coupling coefficient	$[n/d]$
K_v	Velocity ratio	$[n/d]$
K_{interf}	Wake interference coefficient	$[n/d]$
L_{duct}	Tail rotor duct length	$[m]$
M_a	Moment around Z_{HUB} produced by a single ring of the tail rotor	$[N\,m]$
R_{TR}	Tail rotor radius	$[m]$
R_{duct}	Tail rotor duct radius	$[m]$
SL_{CG}	Center of gravity station-line coordinate	$[m]$
S_{ref}	Reference surface of a component	$[m^2]$
S_{wet}	Surface of a component wetted by the main rotor wake	$[m^2]$
T_{TR}	Rotational matrix from body reference frame to tail rotor hub reference frame	$[n/d]$
$V_\perp$	Airflow speed component perpendicular to the blade section	$[m/s]$
WL_{CG}	Center of gravity water-line coordinate	$[m]$
$\bar{T}$	Thrust share	$[n/d]$
$\mathbf{F_{TR}}$	Tail rotor force	$[N]$
$\mathbf{F_a}$	Total force produced by the aerodynamic elements	$[N]$
$\mathbf{F_{duct}}$	Duct thrust	$[N]$
$\mathbf{F_{fan}}$	Fan thrust	$[N]$

$\mathbf{M_{TR}}$	Tail rotor moment	$[N\,m]$
$\mathbf{M_a}$	Total moment produced by the aerodynamic elements	$[N\,m]$
$\mathbf{M_{fan}}$	Fan moment	$[N\,m]$
$\mathbf{M_{gyro}}$	Gyroscopic moment	$[N\,m]$
c	Chord of the element (blade or surface)	$[m]$
e_x	Wake midline off-axis displacement along the x-axis direction	$[m]$
e_y	Wake midline off-axis displacement along the y-axis direction	$[m]$
k_{eps}	Corrective parameter for tail rotor induced velocity	$[n/d]$
n_b	Number of tail rotor blades	$[n/d]$
p	Roll rate	$[rad/s]$
p_{dyn}	Dynamic pressure	$[N/m^2]$
q	Pitch rate	$[rad/s]$
r	Yaw rate	$[rad/s]$
u, U	Velocity component along the x-axis	$[m/s]$
v, V	Velocity component along the y-axis	$[m/s]$
w, W	Velocity component along the z-axis	$[m/s]$

$$\textbf{Subscripts} = \begin{cases} \text{MR} & \text{Main Rotor} \\ \text{TR} & \text{Tail Rotor} \\ \text{AF} & \text{Airframe} \\ \text{HS} & \text{Horizontal stabilizer} \\ \text{VF} & \text{Vertical fin} \\ \text{RH} & \text{Rotor Head} \\ \text{CG} & \text{Center of gravity} \end{cases}$$

Chapter 1

Introduction

1.1 The aviation era

With the invention of the first airplane by the Wright brothers at the beginning of the XX century, a new technological era arose: the aviation era. By unlocking the ability to fly, new possibilities were available to humanity: airplanes, at their beginning, introduced a new way of traveling, new possible trade routes, and new ways to fight. However, with the development of airplane technology and surfing the research for new technology, humanity's needs led to the invention of a new type of flying vehicle, one that could stay in flight in hover conditions and land and takeoff vertically. Several attempts have been made to invent a stable aircraft with these abilities. One of the first results was achieved by Sikorsky only in 1939 with his $VS-300$. The aircraft was still tethered to the ground and had weights suspended underneath it to help keep it stable, but a 4-cylinder Lycoming engine of $75\,hp$ powered it and allowed it to takeoff and hover. It also had full cyclic pitch control for the main rotor and a single anti-torque tail rotor at the end of a narrow enclosed tailboom which also supported a large under-fin. This aircraft is considered the first helicopter with a driven rotor. Over the years, interest in these types of flying machines has led to the development of helicopters with an increasing level of complexity, also improving performance and capabilities.

1.2 Why helicopters?

Helicopters are noisy, slow, and expensive. So why do we still use them?

The great benefit introduced by helicopters is the ability to provide versatility and access to a wide range of applications due to their ability to hover, fly forwards, backward, and laterally, and land or takeoff in small spaces. Thanks to these perks, they still occupy a significant sector in the aeronautical market. Some helicopter missions are in common with some missions of airplanes, like, for instance, transporting people or extinguishing

Figure 1.1: First flight of the Wright Brothers (1903)

fires. However, helicopters have their own market thanks to their abilities, and so they are used on several occasions:

- Transportation: Helicopters can reach remote or hard-to-access areas that other forms of transportation cannot.

- Emergency response: Helicopters are used for search and rescue operations, medical evacuation, and firefighting. They can quickly carry injured people to a hospital, also thanks to their ability to land and takeoff from the roof of buildings.

- Military operations: Helicopters are used for transport and reconnaissance and are perfect for carrying weapons and soldiers into the battleground.

- Aerial observation: Helicopters are used for surveillance, mapping, and environmental monitoring.

- Security: Police use them for security purposes.

- Construction and maintenance: Helicopters are used for heavy lifting and transporting materials and personnel in construction and maintenance projects. In addition, farmers use them to spread seeds and fertilizers on their fields.

Needless to say, helicopters are aircraft of great importance in the aeronautical sector, and they are also the basis on which several new aircraft have been developed, like tilt-rotors or compound helicopters.

Figure 1.2: The VS-300 of Sikorsky (1939)

1.3 New frontiers for helicopters

Nowadays, the research for new technologies and the boost towards sustainability has also affected the helicopter world and market. Current helicopters need to be more sustainable, more affordable, and with an increased operational capability. Today, these are the high-level requirements for the design of a new helicopter and represent a challenge to succeed in order to be attractive in the market sector. However, trying to be attractive usually reflects in developing new and more complex systems that must be certified in order to be airworthy, and the certification process is more complicated the more safety-critical the newly introduced systems are.

From a sustainability point of view, the new regulation toward net-zero carbon emissions in 2050 pushes helicopter companies to find new ways of cutting emissions within all the product life cycle. One common target is electrifying as much as possible the sector in order to obtain hybrid aircraft that are less polluting and more attractive to the market. Almost 2.5% of global emissions are due to the aeronautical sector, so whatever makes an aircraft a little bit greener must be considered in order to fit the market demand and the stakeholder requirements.

It should be highlighted that nowadays, despite the push towards a greener aeronautical sector, having a complete electric helicopter is impossible since the technology, mostly battery technology, is not advanced enough to sustain a full electric helicopter. The power needed from the rotor is very high and would require a considerable amount of batteries, increasing in this way the weight of the aircraft and, as a consequence, the power the rotor should generate. Modern solutions for eVTOL aircraft found the best compromise in a tilt-rotor aircraft that is able to hover and takeoff and land vertically and work as a propelled aircraft in forward flight. Nevertheless, full-electric helicopters are a far reality, and a hybrid solution is a close-range target for the helicopter sector.

There are several new frontiers in the helicopter world, including:

- Electric and hybrid helicopters: Electric and hybrid power systems are being developed for helicopters to reduce emissions and noise pollution.
- Autonomous helicopters: Autonomous technology is being developed to allow helicopters to fly without human pilots, which could lead to increased safety, efficiency, and cost savings.
- Vertical takeoff and landing (eVTOL) aircraft: Electric vertical takeoff and landing (eVTOL) aircraft are being developed for urban air mobility. These aircrafts combine the vertical takeoff and landing capabilities of helicopters with the speed and range of fixed-wing aircraft.
- Other planet helicopters: new aerial vehicles have been realized to fly in atmospheres other than Earth's.

1.3.1 Airbus Flightlab Helicopter

Airbus Helicopters intends to pursue the testing of hybrid and electric propulsion technologies with its Flightlab demonstrator. The Flightlab is an Airbus-wide initiative, which reflects the company's approach to innovation focused on delivering value to customers. Airbus already has several well-known Flightlabs, such as the A340 MSN1, used to assess the feasibility of introducing laminar flow wing technology on a large airliner, and the A350 Airspace Explorer used to evaluate connected cabin technologies inflight.

Airbus Helicopters' Flightlab provides an agile and efficient test bed to quickly test technologies that could later equip Airbus' current helicopter range and even more disruptive ones for future fixed-wing aircraft or eVTOL platforms.

The Flightlab Helicopter has started flight tests with a backup engine system that will function as an emergency electrical power system in case of turbine failure. The Flightlab helicopter's main gearbox will have a $100kW$ electric motor connected to it to provide electrical power for 30 seconds in the event of engine failure, according to Airbus. The aim is to give pilots extra time to react to a possible failure. This demonstrator represents

Figure 1.3: Airbus Flightlab Helicopter during the flight test (Courtesy of Airbus)

a way towards hybrid-electric propulsion system development, but also for exploring autonomy and other technologies aimed at reducing helicopter sound levels or improving maintenance and flight safety.

1.3.2 Leonardo AWHERO

Rotary Unmanned Air Systems (RUAS) are bringing a new level of capability to civil and military missions. Leonardo's state-of-the-art, unmanned AWHERO is a versatile dual-use platform that can operate day and night, over land and sea. It is a reliable, cost-effective solution for diverse roles and is the only RUAS in its class designed with safety features such as systems redundancy.

AWHERO can perform a wide range of utility applications, including disaster relief, environmental monitoring, firefighting, and pipeline or powerline monitoring. It is also an ideal solution for security missions such as traffic enforcement, surveillance, patrol, and aerial monitoring of sensitive targets. Military operators can call on AWHERO to perform a spectrum of the battlefield and maritime missions, including Intelligence, Surveillance, Target Acquisition and Reconnaissance (ISTAR), force protection, combat support, route clearance, cargo re-supply, anti-piracy, maritime security, and Beyond Line of Sight (BLOS) communications relay for other unmanned systems.

Figure 1.4: AWHERO during the flight test (Courtesy of Leonardo)

The AWHERO unmanned rotorcraft is designed to international aeronautical standards: it is $3.7\,m$ long, $1.2\,m$ high, and $1.05\,m$ wide, with a folded rotor. The system can be stowed in a $20\,ft$ container and transported by air, land, and sea platforms. The vehicle's empty and maximum takeoff weights are $120\,kg$ and $205\,kg$, respectively. Up to $85\,kg$ of useful load, including payloads and fuel, can be carried on board the UAS. The helicopter features a three-blade main rotor and skid-type landing gear mounted on the fuselage. The landing gear allows the vehicle to safely perform takeoff and landing from rugged terrains or maritime vessels. The UAV incorporates several advanced features, including a triple-redundant flight control and navigation system, an independent flight termination system, a dual-redundant electrical system, automatic failure management, a global positioning system (GPS), and automatic takeoff and landing capability. The vehicle's maritime capabilities include automatic and semi-automatic deck takeoff, landing, and easy deck handling. Powered by a heavy fuel engine burning JP-5, JP-8, and Jet A-1 fuels, the AWHERO unmanned helicopter can fly at a maximum cruise speed of $90\,knots$. The UAS can reach altitudes of $10,000\,ft$ and endure for up to six hours with a payload weight of $35\,kg$.

AWHERO can be teamed with crewed aircraft from a permanent shore base or forward-deployed operating base. Operating alongside AW159 and AW101 helicopters, AWHERO significantly enhances the maritime operational effect and tactical reach during littoral and

Figure 1.5: First main wing transition flight test of the Phoenix 2 (Courtesy of Lilium GmbH)

blue-water operations.

1.3.3 Lilium jet of Lilium Aviation

The Lilium Jet is a vertical takeoff and landing electrically powered prototype (eVTOL) designed by Lilium GmbH.

The initial design included forward-folding wings in order to let the aircraft be piloted as a VTOL and recharged in only a few hours. The first half-scale demonstrator, the *Falcon*, flew in 2015. On April 2017, the unmanned first flight of the two-seat Eagle full-size prototype took place at the Mindelheim-Mattsies airfield in Bavaria, Germany. The five-seat unmanned Lilium Jet first flew in May 2019. By October 2019, after 100 flights, it could transition from vertical to horizontal flight, reaching over $100\,km/h$ ($54\,kn$). On June 6, 2022, Lilium announced it had made its first main wing transition flight test with the *Phoenix 2* eVTOL technology demonstrator at its ATLAS Test Flight Center in Spain. The company stated that completing the main wing transition means the airflow going over the flaps attaches and becomes smooth, allowing the lift to be generated by the wing rather than by the motors. The company completed the main wing transition flight at a speed of 70 knots (130 km/h, 80 mph). Lilium's seven-seat electric jet's timeline is to start production in 2023 with 25 copies. Its next goal is to produce 250 aircraft in 2024, followed by 400 aircraft in 2025. In addition, Lilium has plans to manufacture a 16-seat eVTOL jet for production in 2027 and a 50-seat eVTOL jet for 2030.

The Lilium Jet uses thrust-vectoring via its swiveling ducted fans to provide vertical

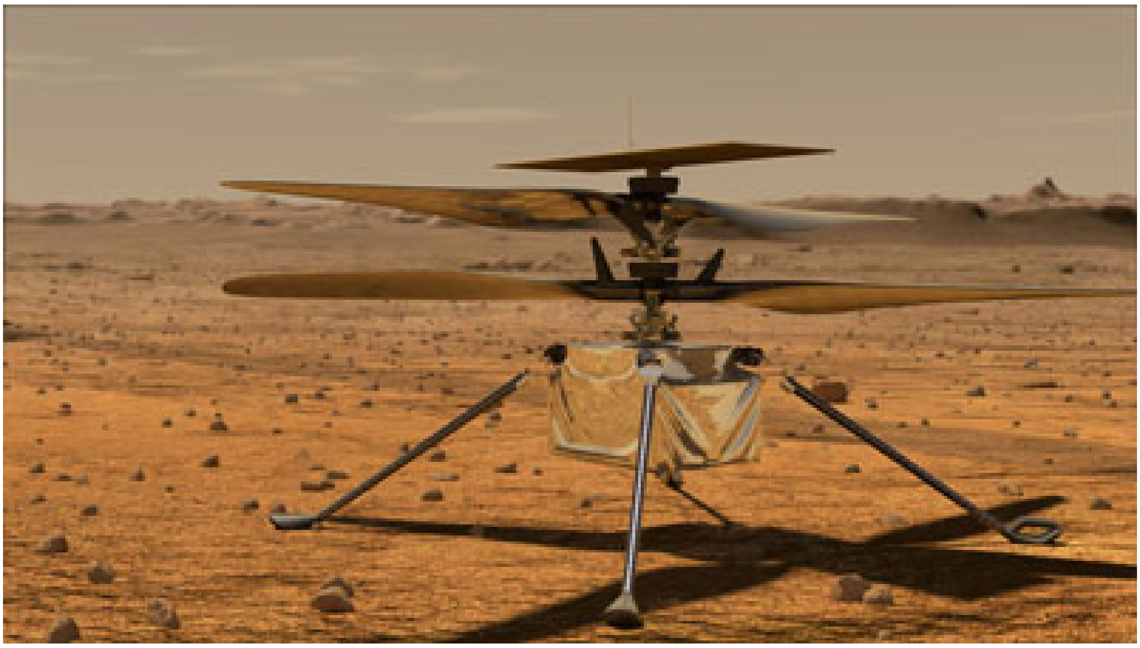

Figure 1.6: Rendering of the Mars Helicopter Scout (Ingenuity) on Mars

thrust for takeoff and landing. These same fans then slowly rotate towards rear facing as the Jet accelerates and converts to its forward flight mode. Electric jet engines are based on the traditional design that powers 95% of commercial aircraft. However, they are more straightforward because they rely on just a single ”stage” rotor/stator system driven by an electric motor. The production Lilium Jet is intended to accommodate six passengers and one pilot. It is powered by 36 electric motors, six on each of the two front wings and twelve on each rear wing. The engines are installed above twelve tiltable rear flaps. The target range is $280km$ $(150nmi)$. Its 36 electric ducted fans are powered by a $1MW$ $(1,300hp)$ lithium-ion battery, but less than $200hp$ $(150kW)$ is required to cruise.

1.3.4 Mars Helicopter Scout (Ingenuity)

The Mars Helicopter, Ingenuity, is a technology demonstration to test powered, controlled flight on another world for the first time. It hitched a ride to Mars on the Perseverance rover. Once the rover reached a suitable ”airfield” location, it released Ingenuity to the surface so it could perform a series of test flights over a 30-Martian-day experimental window.

The planet’s atmospheric density is about $1/100$ that of Earth’s at sea level, or about the same as $87,000ft$ $(27,000m)$, an altitude never reached by existing helicopters. This density reduces even more in Martian winters. To keep Ingenuity aloft, its specially shaped blades of enlarged size must rotate between 2400 and $2900rpm$, or about 10 times faster than what is needed on Earth. The helicopter uses contra-rotating coaxial rotors about $1.2m$ $(4ft)$ in diameter, each controlled by a separate swashplate that can affect both collective and cyclic pitch.

The helicopter was intended to perform a 30-day technology demonstration, making five flights at altitudes ranging 3–5 m (10–16 ft) for up to 90 seconds each. The expected lateral range was exceeded on the third flight, and the flight duration was exceeded on the fourth. The flights proved the helicopter's ability to fly in the extremely thin atmosphere of Mars, over a hundred million miles from Earth, without direct human control. Because radio signals take 5 to 20 minutes to travel between Earth and Mars depending on planetary positions, Ingenuity must operate autonomously, performing maneuvers planned, scripted, and transmitted to it by NASA's Jet Propulsion Laboratory.

The helicopter completed its technology demonstration after three successful flights. For the first flight on April 19, 2021, Ingenuity took off, climbed to about 10 $feet$ (3 $meters$) above the ground, hovered in the air briefly, completed a turn, and then landed. It was a significant milestone: the first powered, controlled flight in the extremely thin atmosphere of Mars, and, in fact, the first such flight in any world beyond Earth. After that, the helicopter successfully performed additional experimental flights of incrementally farther distances and greater altitudes.

Chapter 2

The AW09 helicopter

2.1 General characteristics

The helicopter considered for developing the flight simulator model is the *AW09*, developed by the Swiss company, *Kopter Group*, acquired by Leonardo in 2020. This next-generation, high-performance, single-engine helicopter offers the built-in versatility to tackle multiple missions.

The AW09 has advanced avionics that allows for enhancing safety and situational awareness. The helicopter airframe employs a high-visibility cockpit and is also entirely composed of a lightweight composite structure to ensure crash resistance. It features excellent performance thanks to its Safran Arriel 2K, which incorporates next-generation technology, including no time-life limit, reduced fuel consumption, and a modern dual FADEC.

The main rotor is a five-blade fully composite system that provides excellent maneuverability, low vibrations for smoother flight, and high ground clearance for enhanced safety on the ground. It also has a shrouded tail rotor that ensures the highest safety levels, minimizing the risk of harming ground personnel and accidental contact with obstacles and objects. The aerodynamic design of the rotor fairing additionally increases the anti-torque thrust during flight and provides superior performance. The tail rotor design, featuring 10 unevenly spaced blades, provides extremely low noise emission levels, low maintenance, and high damage tolerance.

2.2 Helicopter history

The first design was developed in 2002 by a mechanical engineer and commercial helicopter pilot. He saw that the light single-engine helicopter market had not seen any all-new designs in decades, and he conducted market research that indicated a viable demand for a new rotorcraft in the class of MTOM lower than 2.5 *tonn*. In 2007, Marenco Swisshelicopter

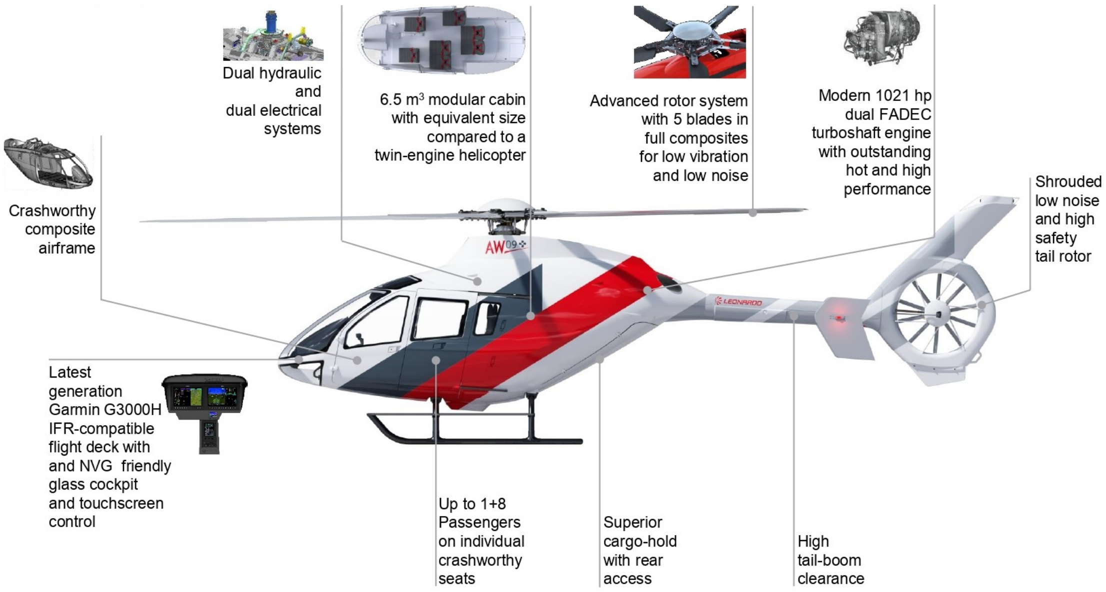

Figure 2.1: The AW09 Helicopter (Courtesy of Kopter Group AG) [2]

Maximum Takeoff Weight (MTOW) - Internal	2850 kg / 6284 lbs
Maximum Takeoff Weight (MTOW) – External	3000 kg / 6614 lbs
Cargo hook rating	1500 kg / 3300 lbs
Capacity	1 Pilot + up to 8 Passengers
Power plant	Honeywell HTS 900
Maximum Takeoff Power (TOP)	760 kW / 1020 hp
Fast cruise speed	260 km/h / 140 kts
Maximum range	800 km / 430 nm
Maximum endurance	Up to 5 h

Table 2.1: *AW09* Main Characteristic [12]

was born to develop the rotorcraft.

By 2009, sufficient financing had been secured from investors, which allowed for the SH09 to be formally launched that year with the designation SKYe SH09 in reference to the year that development on the project officially commenced. A small number of people worked on the project, initially a team of nine; however, in 2016, the company had over 100 employees. Company operations in Switzerland have been split between the towns of Wetzikon, where design work is centered, and Mollis, where assembly and flight testing operations are conducted; a third facility in Germany handles compliance verification. In 2011, in Orlando, Florida, a pre-production prototype of the SH09 was displayed at Heli-Expo 2011, marking its first public introduction. The first prototype was completed in 2013 and took off for the first time at Mollis on October 2014, performing five hover phases at 2 meters above the ground for about 20 minutes total. The second prototype flew for the first time in February 2016. In 2018, the company was renamed Kopter Group, and the helicopter's name was changed to SH09. On April 2020, Kopter was purchased by Leonardo. From June to October 2020, the third prototype made several flights, some of which were held in Sicily, Italy, to test the aircraft's behavior in a hot environment and to evaluate the behavior of a new rotor installed in January of that year. On January 2021, the third prototype resumed flight operations equipped with an elongated rotor shaft, a new tail rotor design, a new transmission, modified skids, relocated fuel tanks to increase cabin space, flight controls moved from inside to outside the rotor shaft, and Garmin G3000H avionics. On April 2021, the helicopter was named AW09, consistent with the rest of Leonardo's production but using only two digits instead of the usual three to let Kopter Group maintain its identity.

2.3 The AW09 innovation

The operations that involve the helicopter produced by *Kopter Group* are mainly in the civil sector and reflect the typical operations of a multi-purpose helicopter: the AW09, thanks to its large cabin, is perfect for transporting passengers but also for medical and search and rescue applications. The other type of operation concerns law enforcement as well as utility applications.

Kopter, with the AW09, wants to develop a new innovative aircraft, also considering the market requirement for an aircraft that is more sustainable, more affordable, and with an increased operational capability. Kopter doesn't want to create a completely electric helicopter because, nowadays, the technology is not ready yet for this giant leap. His solution to come across the new regulation and requirements for what concerned emission is introducing a hybrid helicopter whose level of hybridization will evolve in time with the evolving of the energy storage technology (Figure 2.2).

The closest step in the strategy is adding an electric backup to the internal combustion engine. This backup works as an emergency electrical power system in case of turbine failure. This is a small but essential step in the development of hybrid helicopters because the benefit is not only lowering emissions but, as in this case, also extending the operating capabilities. A single-turbine helicopter, in fact, is certified in Category B, and this involves that upon engine failure at any time during the flight, a forced landing is required. However, a hybrid architecture may offer at low altitudes, a safety level superior to Category A rotorcrafts.

As can be seen in Figure 2.3, in case of an engine failure inside the H-V curve, the backup electrical propulsion system can take over in order to ensure continuous safe flight out of the avoid zone and, in the end, safely landing with the reserve energy.

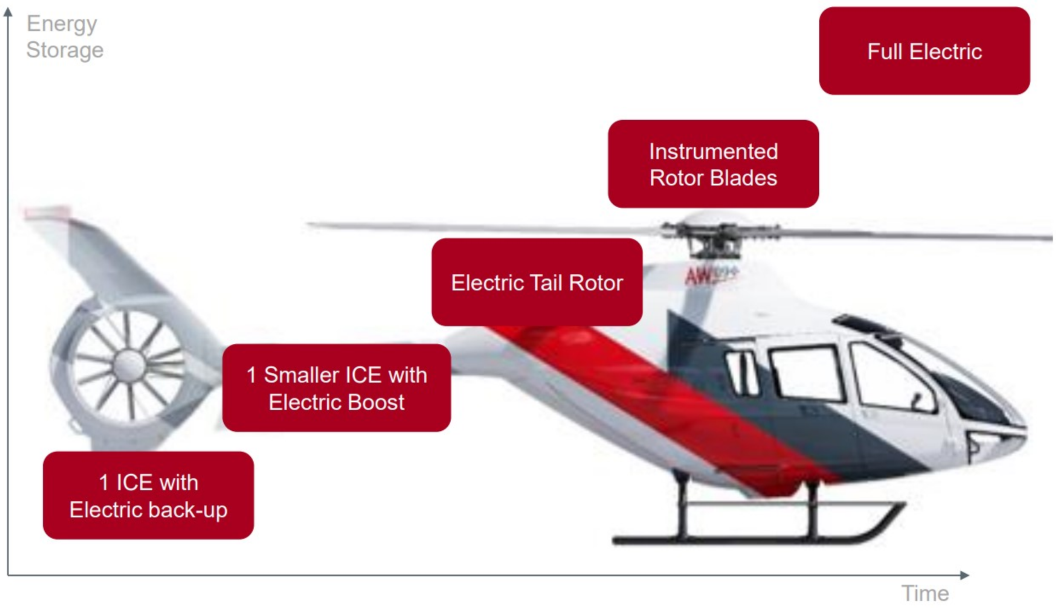

Figure 2.2: Kopter Innovation Strategy
(Courtesy of Kopter Group AG) [2]

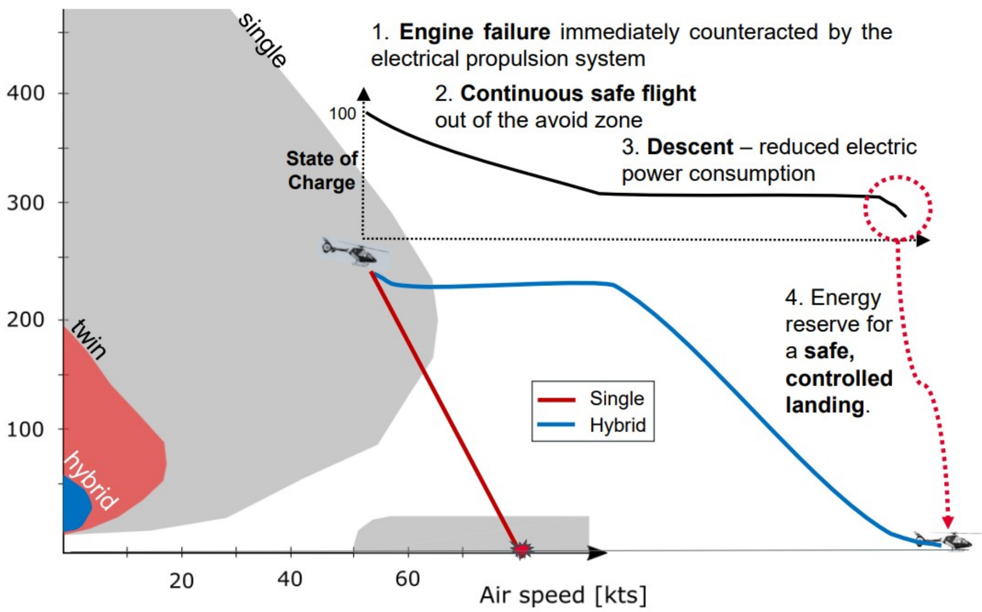

Figure 2.3: Engine failure inside the H-V Curve
(Courtesy of Kopter Group AG) [2]

- Mitigate operational risks
- Improve public acceptance
- Larger range of landing sites following an engine failure:
  - More time-to-descent and maneuvering range
  - Reduced cockpit stress
  - Improving the landing site decision, e.g., also considering obstacle clearance
- No more autorotation landings following an engine failure since the hybrid system can support normal landing
- Suppressed (reduced) H-V curve:
  - recovery and safe landing from almost all flight attitudes
  - Better power rating than a twin-engine helicopter with One-Engine-Inoperative
- True engine redundancy
  - No common cause of failure due to, e.g., fuel contamination
  - No common mode failure

Table 2.2: Safety-related benefits of electric backup

- Higher efficiency propulsion that allows lowering the operating cost
- Lower CO2 output
- Performance and handling same as normal ”turbine” landing:
  - Reduced training requirement
  - No need for a One-Engine-Inoperative training mode
- Simplified emergency take-off and expanding procedures
  - No need to define a Landing Decision Point (LDP)
  - Easier pilot training and reduced cockpit workload

Table 2.3: Training and environmental benefits of electric backup

Adding a backup electric propulsion system to the helicopter is, therefore, connected to several benefits. Among these, the most significant are the safety-related benefits, listed in Table 2.2, and the training and environmental benefits, listed in Table 2.3.

2.4 The role of flight simulation

A flight simulator is a device whose primary purpose is to artificially re-create the aircraft's in-flight behavior. Over the years, the role of flight simulation has become increasingly important; the main advantages associated with this technology are:

- Safe application, because the flight simulator allows simulating critical situations which might be riskier if performed on the real aircraft (e.g., aggressive maneuver or operation out of the flight envelope).
- Cost effectiveness, because the cost associated with the operation with a flight simulator is much more affordable if compared to flying with the real aircraft, and this is also very important considering the pilot training.
- Extended operative range, because the flight simulator allows studying the vehicle and training the pilots out of the flight envelope.
- Low environmental impact, because the emissions related to the flight simulation are zero while flying the real aircraft involves a considerable environmental impact.

The core of the flight simulation is the mathematical model, which describes how the aircraft works in order to reproduce its behavior. For the development of a flight simulator, there is usually a trade-off between the complexity (i.e. the computational cost) of the math model, and the need to run in real-time.

There are high-fidelity simulators based on a very accurate mathematical model which reproduces in every single detail the characteristics of the system. These flight simulators are associated with a high computational cost and high delays in the aircraft model response, so they are used for research purposes.

However, real-time simulators are the most common because they are used in online operations, such as the training of pilots. These simulators are characterized by a less accurate mathematical model in order to keep the delays under certain limits and can be used in research applications as well as in man-in-the-loop applications. The man-in-the-loop applications involve the presence of a pilot that interacts within the flight simulator. These applications are related to the training of the pilots, but they also allow the test pilot to evaluate the workload and handling qualities of the aircraft, both without automatic

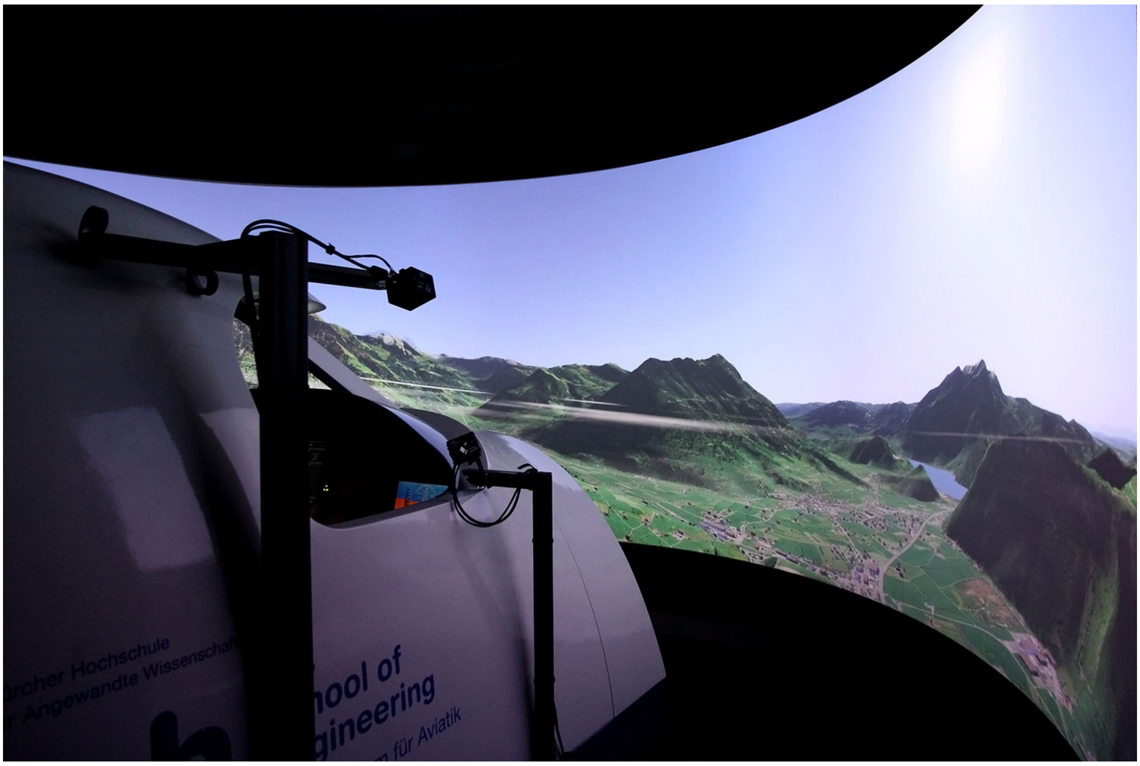

Figure 2.4: ReDSim flight simulator (Courtesy of ZAV)

control enhancing systems and with various control configurations, helping designers in the selection of the most suitable Stability and Control Augmentation System (SCAS).

Ultimately, an important role of flight simulation is also to contribute to the development of the aircraft flight control system. First, it is possible to improve the fidelity of the developed simulation model through the use of parameter estimation, which is the process of calculating the parameter values of a model from measured data. By improving the fidelity of the model, it is later possible to support the design and validation of a flight control system.

Chapter 3

Development of the mathematical model

3.1 Tail rotor mathematical model

As introduced in the previous chapter, the tail rotor of the studied helicopter has a ducted configuration. Although the primary function of the element is balancing the main rotor torque and providing directional control, the presence of the shroud affects how the tail rotor works, in addition to providing protection to the fan blade and thus enhancing the safety of the helicopter itself and the ground staff.

This thesis aims not to discuss the positive and negative aspects of a shrouded tail rotor summarized in Ref [10].

3.1.1 Reference Frame

One of the first steps in approaching the modeling of a system is the adoption of a reference frame system. The primary reference frame chosen for the tail rotor model implemented is the one reported in Figure 3.1. This reference frame is called the *hub reference frame* and is fixed and centered in the tail rotor hub.

- X_{Hub} is in the hub plane and positive forward;
- Y_{Hub} is in the hub plane and positive upwards;
- Z_{Hub} is perpendicular to the hub plane and positive starboard.

Thus, in nominal conditions, the tail rotor generates a thrust whose direction is opposite to Z_{Hub}, and at the same time, the induced velocity on the rotor is in the same direction as Z_{Hub}.

The rotation matrix from the conventional body reference frame to the tail rotor hub

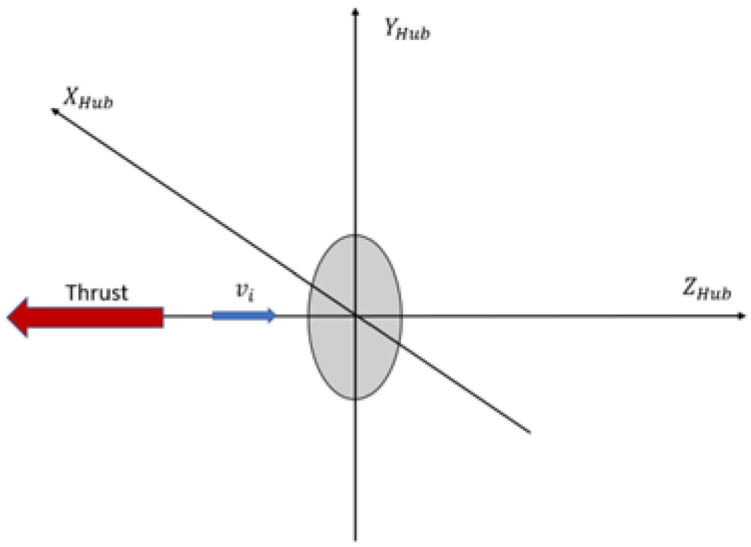

Figure 3.1: Tail rotor Hub reference frame

reference frame is:

$$T_{TR} = \begin{bmatrix} 1 & 0 & 0 \\ 0 & 0 & -1 \\ 0 & 1 & 0 \end{bmatrix}$$

3.1.2 Hub Loads

The tail rotor model's main output is the loads. In particular, the loads are evaluated in the Hub reference frame introduced in the previous section. For the evaluation of the forces and moments produced by the component, for simplicity's sake, the author divided the tail rotor into its components: the fan and the duct.

Fan

The fan is the rotating element of the tail rotor. A modified blade element theory is used to describe the aerodynamic behavior of the fan. The main principle of this modified blade element theory is to discretize the fan disc in a finite number of rings of the same area and calculate the load contribution of each ring. For each ring, a blade section is considered with a length equal to the width of the ring. The blade chord, twist, and aerodynamic coefficients are evaluated in the middle of the section considered.

This approach has the effect of neglecting several things, like the fact that the fan blades are not equally spaced and also the effect of the increased speed in the advancing blade and the decreased speed in the backward blade in forward flight. Although the blade spacing is very important in terms of acoustic emission, the effect on the aerodynamic behavior is

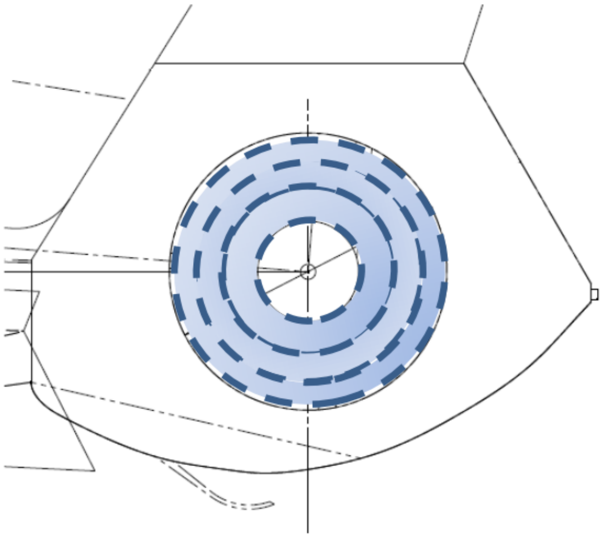

Figure 3.2: Discretization of the fan in 3 rings [7]

almost null. Instead, the increasing and decreasing blade speed with the azimuth position in forward flight can be neglected since the shroud protects the fan, so the tail rotor in-plane velocities do not affect the fan's aerodynamic behavior.

Figure 3.3 represents an airfoil's generic aerodynamic behavior.

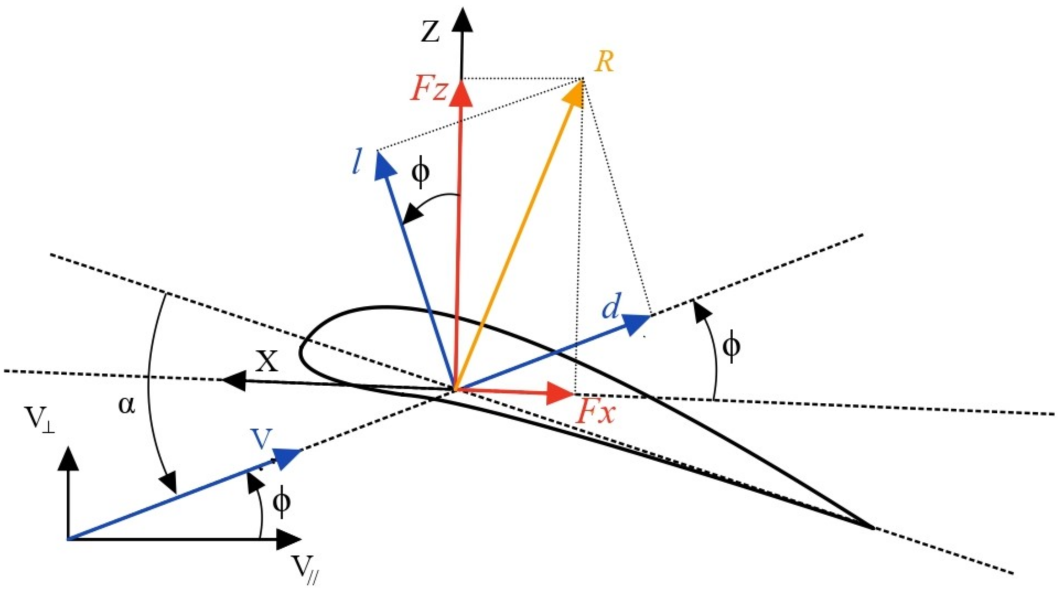

Figure 3.3: Generic aerodynamic behavior of an airfoil

As can be seen, it is assumed that only a lift and a drag force are produced while the pitching moment is neglected. For the blade section of each ring, the aerodynamic angle of attack is computed to evaluate the forces generated. This angle is generally calculated as follows:

$$\alpha = \theta_0 + \theta_{twist} + K_1\beta - \alpha_0 + \phi \tag{3.1}$$

The different contributions are:

- θ_0 is the collective blade pitch angle commanded by the pilot through the pedal. The tail rotor is controlled only with a collective pitch, while the cyclic terms are not present;

- θ_{twist} is the blade twist angle and is a function of the position along the blade. A polynomial law is used to evaluate this angle;

- $K_1\beta$ is the term due to the pitch-flap coupling. However, since $K_1 = tan(\delta_3)$ and δ_3 is null, this term is not considered in the model;

- α_0 is the blade section angle of attack corresponding to zero-lift;

- ϕ is the blade section inflow angle

This last angle identifies the direction of the airflow on the blade section and can be expressed as:

$$\phi = \arctan\left(\frac{V_\perp}{V_{||}}\right) \tag{3.2}$$

The velocities that appear are the airflow speed perpendicular to blade section $V_\perp$ and the airflow speed parallel to blade section $V_{||}$. The first is a function of the aircraft motion and the fan inflow speed:

$$V_\perp = -(V_i - w_{Hub})$$

The parallel component is instead a function of the angular velocity of the fan:

$$V_{||} = \Omega_{TR} r$$

where r is the section position along the blade. As discussed previously, the aircraft's forward and vertical velocities are neglected since the shroud protects the fan.

To simplify the model, the blade flapping dynamic is considered negligible since a flap hinge is not present for the tail rotor blade, and the blade is also considered a rigid body.

Since the aerodynamic coefficients are a function not only of the angle of attack but also of the Mach number, this last is also calculated for the blade section of each ring as:

$$Mach = \frac{\sqrt{V_{||}^2 + V_\perp^2}}{v_{sound}} \tag{3.3}$$

Thus, the aerodynamic lift coefficient C_L and the aerodynamic drag coefficient C_D are evaluated with a double linear interpolation.

$$C_L = C_L(\alpha, Mach) \qquad\qquad C_D = C_D(\alpha, Mach)$$

Finally, the fan hub loads are evaluated. The forces components are calculated as follows:

$$\mathbf{F_{fan}} = \begin{bmatrix} 0 \\ 0 \\ \sum\limits_{Rings} F_a \end{bmatrix} \tag{3.4}$$

where F_a is the thrust produced by each ring and is expressed as follows:

$$F_a = -t_{tiploss}\,\frac{1}{2}\,\rho\,n_b\,(h\,chord)\,(C_L\,\cos(\phi) + C_D\,\sin(\phi))\,(V_\perp^2 + V_{||}^2)$$

In the formula appears some parameters which are:

- $t_{tiploss}$, the tip-loss factor that considers the aerodynamic loss at the tip of the blade and so improves the model fidelity;
- n_b, the number of blades of the fan;
- h, the width of each ring.

As can be seen, the fan is considered to produce a force only along Z_{Hub} because the shroud protects the fan, and, as a consequence, the flow is considered to be axial-symmetric. The force along Z_{Hub} is obtained by summing the forces produced by each ring.

Similarly, the moments generated by the fan are evaluated:

$$\mathbf{M_{fan}} = \begin{bmatrix} 0 \\ 0 \\ \sum\limits_{Rings} M_a \end{bmatrix} + \mathbf{M_{gyro}} \tag{3.5}$$

where:

$$M_a = -t_{tiploss}\,\frac{1}{2}\,\rho\,n_b\,(h\,chord)\,r\,(-C_L\,\sin(\phi) + C_D\,\cos(\phi))\,(V_\perp^2 + V_{||}^2)$$

$$\mathbf{M_{gyro}} = I_{pTR}\begin{bmatrix} p_{TR} \\ q_{TR} \\ r_{TR} \end{bmatrix} \times \begin{bmatrix} 0 \\ 0 \\ \Omega_{TR} \end{bmatrix} = \begin{bmatrix} I_{pTR}\,q_{TR}\,\Omega_{TR} \\ I_{pTR}\,p_{TR}\,\Omega_{TR} \\ 0 \end{bmatrix}$$

In this case, the overall fan moments produced are a sum of the aerodynamic moments due to the blade aerodynamics and the inertial moments related to the gyroscopic effects.

Duct

The duct is a complicated element to model accurately without computational fluid dynamic analyses. However, these analyses are expensive in terms of computational cost and inadequate for a real-time flight simulator. For this reason, it has been chosen to describe its behavior by evaluating the thrust share, which is the ratio between the thrust produced by the fan and the total thrust produced by the tail rotor:

$$T_{share} = \bar{T} = \frac{F_{fan_z}}{F_{TR_z}}$$

This ratio could be expressed as a function of the geometry as shown in Ref [5]:

$$\bar{T} = 1 + \varepsilon_B \left(\frac{K_V}{2} + \frac{\eta_{inlet} + \eta_{diffuser}}{2\,K_V} - 1 \right) \tag{3.6}$$

The geometric parameters that appear in the formula are:

- The blade tip clearance ε_B evaluated as a function of δ_{tip}/R_{duct};
- The inlet drag factor η_{inlet} evaluated as a function of r_{inlet}/R_{duct};
- The diffuser drag factor η_{diff} evaluated as function of α_{diff}, R_{duct} and L_{duct},

Furthermore, in the formula above appears the velocity ratio, K_V, which is not a geometric parameter and will be discussed later in a proper section.

In this way, it is considered that the duct generates only a force along Z_{Hub} expressed as a function of the thrust share and the fan thrust:

$$\mathbf{F_{duct}} = \begin{bmatrix} 0 \\ 0 \\ F_{fan_Z}\left(\frac{1}{\bar{T}} - 1\right) \end{bmatrix} \tag{3.7}$$

Figure 3.4 shows that the point of application of the thrust produced by the shroud depends on how the pressure is distributed along the inlet. However, the model implemented for the duct cannot evaluate the pressure distribution because this last depends on several factors, primarily the aerodynamic conditions. Thus, it has been chosen to consider that the point of application of the thrust of the shroud coincides with the fan center and so the origin of the tail rotor Hub reference frame. This approximation leads to neglecting some moments produced by the duct, which, however, are negligible.

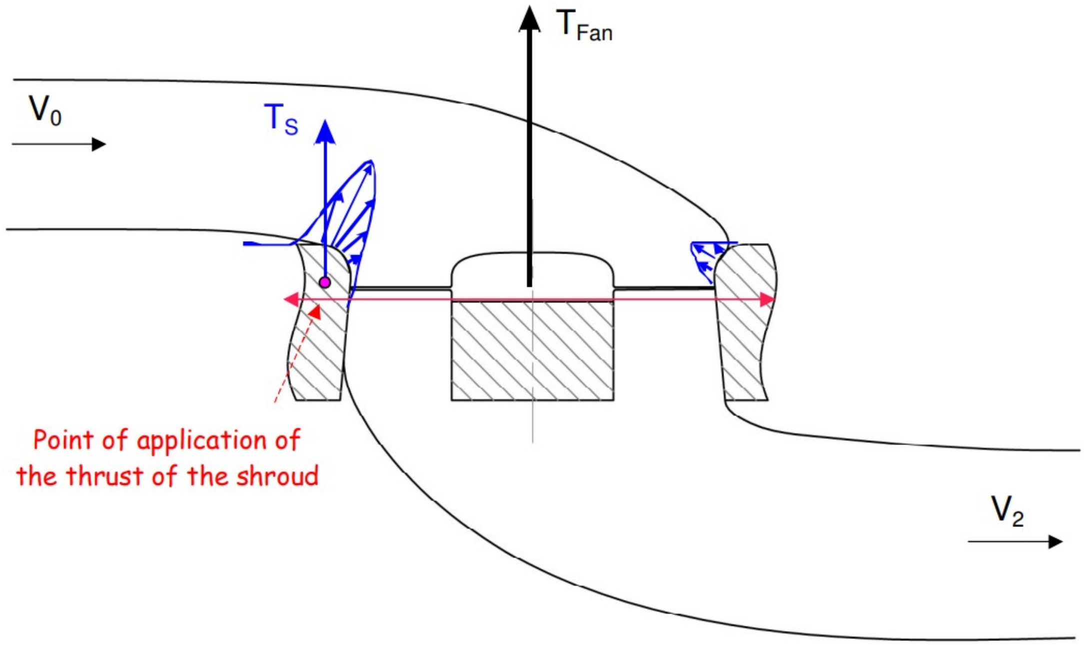

Figure 3.4: Point of application of the duct force in the reality [4]

Total loads

After studying the fan and the duct separately it is possible to express the force and moments developed by the whole tail rotor. The total loads produced are evaluated as follows:

$$\begin{aligned} \mathbf{T_{TR}} &= \mathbf{F_{fan}} + \mathbf{F_{duct}} \\ \mathbf{M_{TR}} &= \mathbf{M_{fan}} \end{aligned} \tag{3.8}$$

3.1.3 Dynamic inflow

The inflow computation is modeled according to the formulation introduced by Pitt-Peters [9]. This formulation assumes for the non-dimensional flow velocity induced by the rotor the following distribution:

$$\lambda = \frac{V_{inflow}}{\Omega_{TR} R_{TR}} = \lambda_0 + \frac{r}{R}\lambda_{1s}\,sin(\psi) + \frac{r}{R}\lambda_{1c}\,cos(\psi)$$

The rotor inflow velocity is defined in a reference frame centered in the Hub reference frame and with an x-y plane parallel to the tip-path plane. The rotation matrix between the two reference systems is:

$$T_{HA} = \begin{bmatrix} \cos(\beta_{1c}) & \sin(\beta_{1s})\, sin(\beta_{1c}) & \cos(\beta_{1s}) \\ 0 & \cos(\beta_{1s}) & -\sin(\beta_{1s}) \\ -\sin(\beta 1c) & \cos(\beta_{1c})\sin(\beta_{1s}) & \cos(\beta_{1c})\cos(\beta_{1s}) \end{bmatrix}$$

The formulation proposed by Pitt-Peters defines a correlation between the inflow velocity components and the aerodynamic loads generated by the rotor:

$$M_{pp} \begin{Bmatrix} \dot{v_0} \\ \dot{v_{1s}} \\ \dot{v_{1c}} \end{Bmatrix} + L_{pp}^{-1} \begin{Bmatrix} v_0 \\ v_{1s} \\ v_{1c} \end{Bmatrix} = \begin{Bmatrix} C_t \\ C_l \\ C_m \end{Bmatrix} \tag{3.9}$$

where:

- v_0, v_{1s}, and v_{1c} are the inflow velocity components in a reference frame parallel to the tip-path plane but with the X axis aligned with the aircraft speed:

$$\begin{Bmatrix} v_0 \\ v_{1s} \\ v_{1c} \end{Bmatrix} = \begin{bmatrix} 1 & 0 & 0 \\ 0 & \cos(\beta_h) & -\sin(\beta_h) \\ 0 & \sin(\beta_h) & \cos(\beta_h) \end{bmatrix}$$

  where β_h is the sideslip angle.

- C_t, C_l, and C_m are non-dimensional coefficients corresponding respectively to the aerodynamic vertical force, rolling moment, and pitching moment generated by the rotor in the same reference frame of the inflow velocity components v_0, v_{1s}, and v_{1c};

- The matrices M_{pp} and L_{pp} derive from semi-empirical consideration and are based on the momentum theory. They are defined as follows:

$$M_{pp} = \frac{1}{\Omega} \begin{bmatrix} \frac{128}{75\pi} & 0 & 0 \\ 0 & -\frac{16}{45\pi} & 0 \\ 0 & 0 & -\frac{16}{45\pi} \end{bmatrix}$$

$$L_{pp} = \begin{bmatrix} \frac{1}{2v_t} & 0 & \frac{15\pi}{64v_t}\tan\frac{\chi}{2} \\ 0 & -\frac{4}{v_m(1+\cos(\chi))} & 0 \\ \frac{15\pi}{64v_t}\tan\frac{\chi}{2} & 0 & -\frac{4\cos(\chi)}{v_m(1+\cos(\chi))} \end{bmatrix}$$

  where:

$$v_t = \sqrt{\mu^2 + (\lambda_0 - \mu_z)^2}$$

$$v_m = \frac{\mu^2 + (\lambda_0 - \mu_z)(2\lambda_0 - \mu_z)}{v_t}$$

$$\chi = \arctan \frac{\mu}{\lambda_0 - \mu_z}$$

With μ and μ_z the horizontal and vertical advance ratios defined as:

$$\mu = \frac{\sqrt{u^2 + v^2}}{\Omega R} \qquad \mu_z = \frac{w}{\Omega R}$$

However, this formulation has been slightly modified in the model implemented considering the following facts and hypothesis:

- The tail rotor is controlled only in pitch;
- The flapping dynamic is ignored;
- Just the fan loads are considered for the computation of the coefficients C_t, C_l, and C_m, also knowing that the gyroscopic moments are not aerodynamic but inertial.

From these considerations, it is possible to assume a uniform inflow acting on the fan and thus ignore λ_{1s} and λ_{1c}.

Furthermore, the Pitt-Peters formulation has also been corrected since it was initially elaborated for an open rotor configuration. To consider the effect of the closed rotor, it has been considered that the velocity ratio K_v (see related chapter) is not equal to 2 as in the standard open configuration, but it changes according to operating conditions. For these considerations, the final formulation is the one reported here:

$$\dot{\lambda_0} = -A\lambda_0 + BC_t \tag{3.10}$$

where:

$$A = \frac{9600\Omega_{TR}\pi\cos(\chi)v_t}{255\pi^2\tan^2(\frac{\chi}{2})(\cos(\chi)+1) + 8192\cos(\chi)}$$

$$B = \frac{75\Omega_{TR}}{128\pi} \qquad C_T = \frac{T_{fan_z}}{\rho V_{tip}^2\pi^2}\frac{1}{K_v/2}$$

3.1.4 Duct and fan interaction

The most challenging part of the work has been understanding how the two components of the tail rotor, the duct and the fan, acted among themselves. The difficulty of this interaction is mainly caused by the duct, whose behavior, as introduced in the relative section, depends a lot on external conditions. Several solutions have been tried with

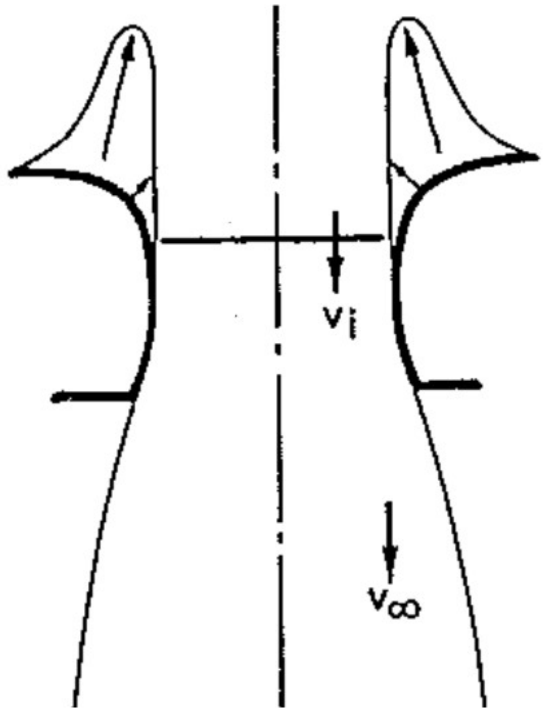

Figure 3.5: Stream tube for a ducted fan

always the focus of keeping the model as simple as possible. In the end, two main features have been implemented in the model to simulate the reciprocal action between the two components: the introduction in the model of the velocity ratio and the correction of the induced velocity on the fan.

Velocity ratio

The velocity ratio represents the velocity increment between the disk and the far wake. Figure 3.5 shows the stream tube for a rotor and the velocity ratio is expressed as:

$$K_v = \frac{v_\infty}{v_i}$$

For an open rotor configuration, the downstream velocity in the wake v_∞ is usually twice the induced velocity at the fan v_i. However, this is not valid for a shrouded rotor because the duct interferes with the aerodynamics and can change the stream tube. In hover, for example, the downstream velocity in the wake for a ducted tail rotor is almost equal to the induced velocity at the rotor, so K_v is close to 1.

In the previous section, this ratio was introduced in the computation of the forces produced by the duct and in the computation of the inflow acting on the fan. There is, in fact, a strong correlation between the velocity ratio and the thrust share. In hover conditions, when K_v is close to 1, the thrust share of a ducted tail rotor is usually close to 50%, which means that the duct produces a force almost equal to the one produced by the fan. Out of hover conditions, however, with the increasing helicopter speed, the duct gradually loses its ability to generate thrust since the aerodynamics on the duct are not stationary. So the thrust share increases as the duct is less efficient and at the same time, the velocity ratio also increases and tends toward the value of 2, the value for the open rotor configuration.

In hover and nominal thrust conditions (flow from the inlet to the diffuser), the velocity ratio is evaluated as a function of the geometry as shown in Ref [5] with the following formulation:

$$K_v = \frac{1}{n(1+0.4\,\alpha_{diff})}$$

where:

$$n = \frac{D_{exit}^2}{(D+2\delta_{tip})^2}$$

In hover and reverse thrust conditions (flow from the diffuser to the inlet), the velocity ratio is evaluated considering the average thrust share from the bench test result in addition to the geometry.

Based on the values of thrust share obtained by a reference model provided by *Kopter* for several trim points, a polynomial law has also been implemented to consider, as discussed above, the increasing of K_v with the helicopter velocity:

- For the nominal thrust condition, a third-degree polynomial law was chosen:

$$K_{v_{ntc}} = a_1\,V^3 + b_1\,V^2 + c_1\,V + d$$

- For the reverse thrust condition, a second-degree polynomial law was chosen:

$$K_{v_{rtc}} = a_2\,V^2 + b_2\,V + c_2$$

Furthermore, since the two curves intersect at a certain velocity, it has been considered that the velocity ratio follows the law of the nominal thrust condition after that velocity. Figure 3.6 shows the behavior of the two laws.

Induced velocity correction

Although in the inflow subsystem a uniform inflow λ_0 is evaluated, in the fan subsystem, the induced velocities are corrected to consider the effect of the duct. In fact, it has been shown by CFD analysis, bench test data, and literature[1] that the latter produces an

[1]Ref [10][7]

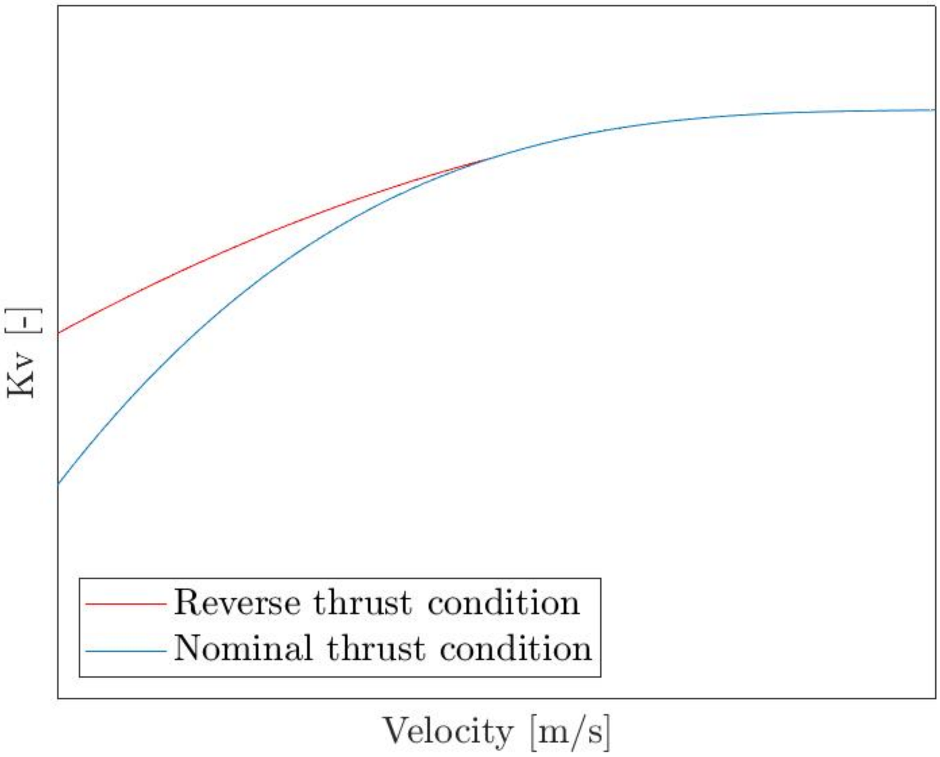

Figure 3.6: Velocity ratio behavior with helicopter velocity

acceleration of the induced velocity along the blade that is more intense the closer they are to the duct. So the correction introduced consists of assuming a linear distribution of the induced velocity along the blade:

$$V_i = \lambda_0 \Omega_{TR} R_{TR} + m(\theta)\, k_{eps} \frac{r}{R_{TR}} \tag{3.11}$$

The terms that appear in the formulation are:

- λ_0 is the non-dimensional induced velocity evaluated by the dynamic inflow model;
- $m(\theta)$ represents the slope of the linear distribution and is expressed as a function of the blade collective pitch. This function has been evaluated from the comparison with the bench test data;
- k_{eps} is a parameter introduced to consider that, as also discussed in the previous section, the effect of the duct is reduced in forward flight and, as a consequence, the acceleration introduced by the duct on the induced velocity is less effective. k_{eps} is a parameter ranging between 0 and 1: in hover condition is equal to 1, instead with the increasing of the helicopter velocity, it decreases. In this way, for high speeds,

k_{eps} is close to 0 because the duct has a minimal effect for those conditions.

Considering a linear distribution of the induced velocity along the blade represents an approximation since, in reality, the boundary layer on the duct interacts with the blade's tip and produces a collapse in velocities rather than an acceleration. However, the approximation is considered valid since the collapse at the blade tip is usually for just the very last part and the results obtained by the implemented model correspond to the reference model as it will be illustrated in Chapter 5.

Figure 3.7 shows the behavior of the induced velocity along the blade for several pedal positions. It can be seen that in nominal thrust conditions, when the flow acts from the inlet to the diffuser, the slope is positive, while in reverse thrust conditions, when the flow act from the diffuser to the inlet, the slope becomes negative. This is consistent since the overall effect is always a higher velocity at the blade tip compared to the blade root.

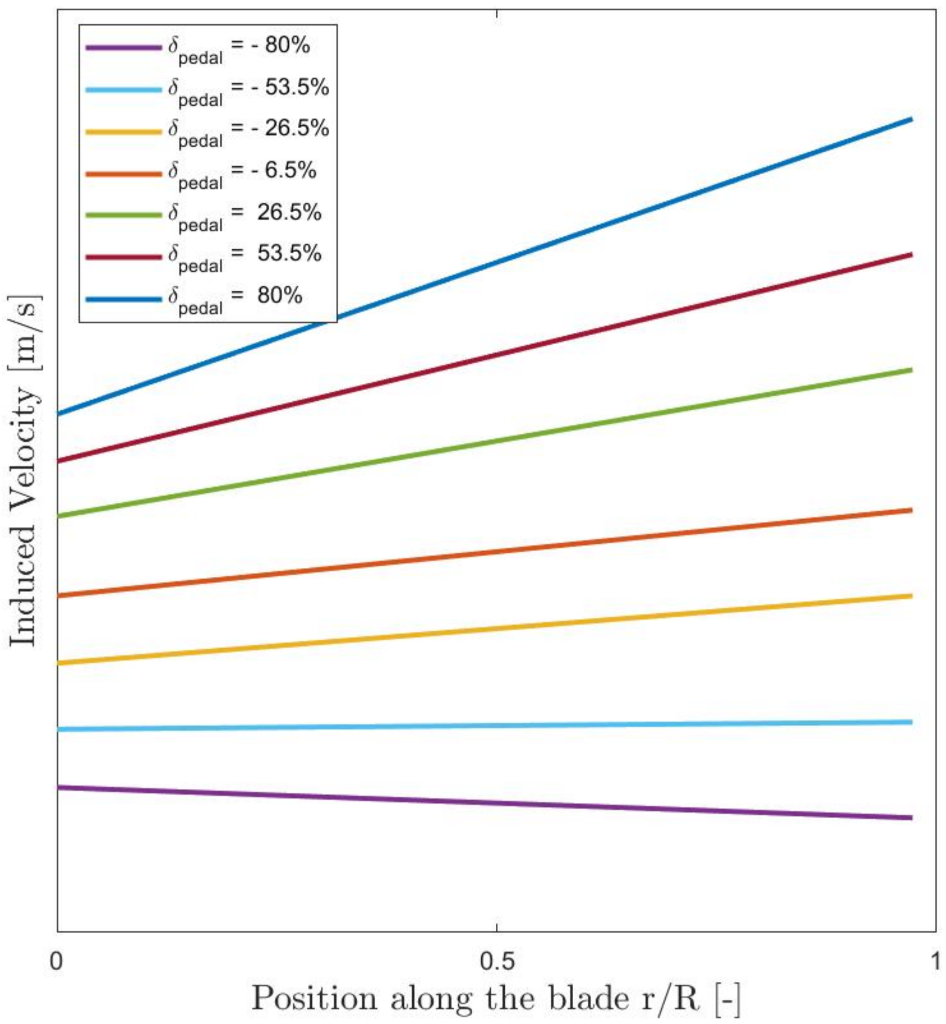

Figure 3.7: Induced velocity distribution along the blade with the pedal position

3.2 Aerodynamics surfaces model

The aerodynamic surfaces are an important part of the helicopter and are responsible for the stability of the aircraft but they are also the main source of drag on the vehicle. In particular, the helicopter surfaces modeled are the following:

- Horizontal stabilizer, responsible for the longitudinal stability of the aircraft;
- Vertical fin, responsible for the lateral and directional stability of the aircraft;
- Airframe, which is the main body of the helicopter, and inside which are present the payload, the systems, and other important elements;
- Main rotor head, which is the part of the main rotor that includes the shaft and the hub, is a source of drag during the helicopter motion.

3.2.1 Reference Frame

First of all, the reference frame for each component was defined. For simplicity's sake, the vertical fin frame, airframe frame, and main rotor head frame are similar. The origins are different, but the axis directions are the same:

- X in longitudinal body-fixed direction, pointing forward.
- Y in lateral body-fixed direction, pointing starboard.
- Z in vertical body-fixed direction, pointing downwards.

Figure 3.8 shows the reference frame of the vertical fin to visualize the axis direction, but in Appendix A, all the reference frames are reported. In the vertical fin reference frame, it can also be seen that the vertical fin has an initial incidence angle different from 0: this is needed to compensate for the effect of the wake of the main rotor, and in this way, the stability of the helicopter is improved. For the horizontal stabilizer, the reference frame is slightly different:

- X in longitudinal body-fixed direction, pointing forward.
- Y in lateral body-fixed direction, pointing port.
- Z in vertical body-fixed direction, pointing upwards.

In Figure 3.9 is shown the reference frame of the horizontal stabilizer to visualize the axis direction. As for the vertical fin, it can also be seen an initial incidence angle different from 0: the purpose is the same as the one for the vertical fin, compensating for the effect of the wake of the main rotor to enhance the stability of the helicopter.

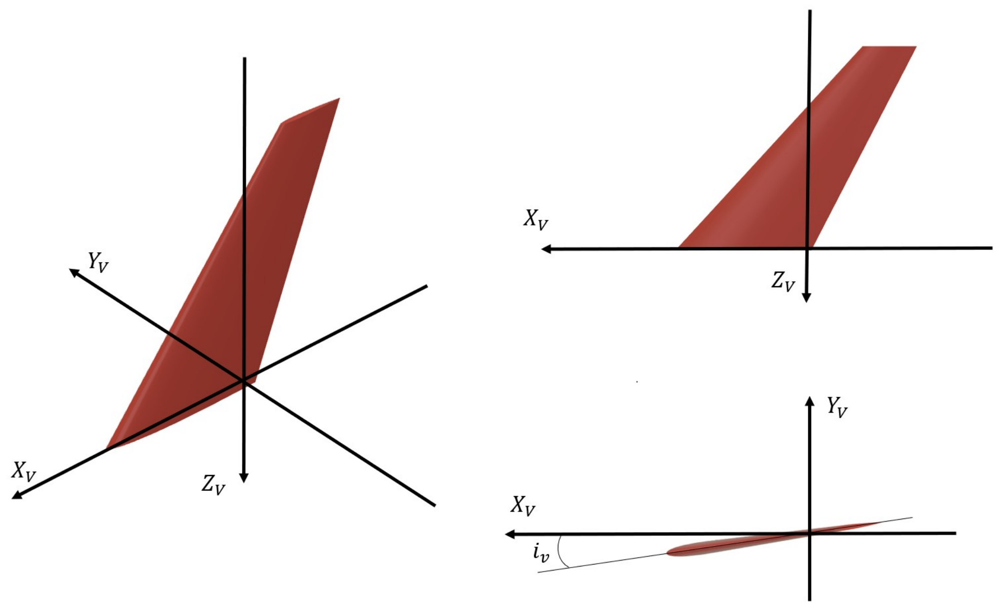

Figure 3.8: Reference frame for vertical fin

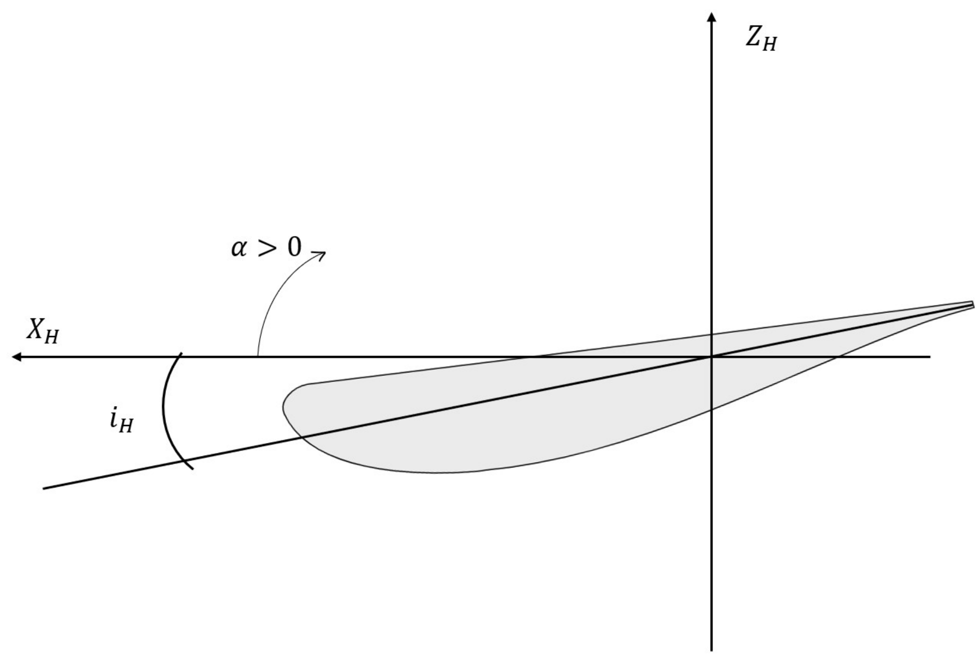

Figure 3.9: Reference frame for horizontal stabilizer

3.2.2 Aerodynamic load computation

For the calculation of the loads produced by each component, the model implemented starts to calculate the local velocities, u_{local}, v_{local} and w_{local}, for each surface considering the aircraft motion (translational and rotational) but also the induced velocity on the components due to the aircraft angular motion and the distance from the helicopter centre of gravity. Furthermore, the induced velocity due to the main rotor wake is also considered.

With the velocities obtained and also considering the air density, the local dynamic pressure is evaluated as follows:

$$p_{dyn_{local}} = \frac{1}{2}\rho V_{local}^2 = \frac{1}{2}\rho\left(u_{local}^2 + v_{local}^2 + w_{local}^2\right) \tag{3.12}$$

Subsequently the local aerodynamic angles of incidence α_{local} and sideslip β_{local} are evaluated as follows:

$$\alpha_{local} = \arctan\left(\frac{w_{local}}{u_{local}}\right) \qquad \beta_{local} = \arctan\left(\frac{v_{local}}{\sqrt{u_{local}^2 + w_{local}^2}}\right) \tag{3.13}$$

The model for the horizontal stabilizer is, however, slightly different. Indeed it is supposed that this component is not dependent on the lateral velocity v_{local} and thus neither from the angle of sideslip. For this component, in addition to the local angle of attack, is instead evaluated the local Mach number as:

$$Mach_{HS} = \frac{\sqrt{u_{HS}^2 + w_{HS}^2}}{v_{sound}} \tag{3.14}$$

And, also the dynamic pressure is:

$$p_{dyn_{HS}} = \frac{1}{2}\rho\left(u_{HS}^2 + w_{HS}^2\right)$$

The other components are supposed not dependent on the Mach number since the max helicopter speed is $140\,kts$, and the horizontal stabilizer is the component most affected by the downwash due to the wake of the main rotor.

After calculating the local dynamic pressure and the local aerodynamic angle, through some 2D look-up tables, the forces and moments coefficient are evaluated. These coefficients have been obtained by Computational Fluid Dynamics (CFD) analysis and by wind tunnel experiments. The forces and moments coefficients are then used to evaluate the real forces and moments generated by each component with the following equation:

$$F_{i_{local}} = p_{dyn_{local}} S_{ref} C_{F_i} \tag{3.15}$$

$$M_{i_{local}} = p_{dyn_{local}} S_{ref}\, c\, C_{M_i} \tag{3.16}$$

where S_{ref} and c represent, respectively, the surface's reference area and the reference cord, while $i = x, y, z$.

For each component, the forces along the three axes, X, Y, and Z, and the moments around the three axes are evaluated. The loads are also reported to the helicopter's center of gravity. Thus, to obtain the barycentric moments, the forces are multiplied with a vectorial product with the distance between the CoG and the reference frame origin of the component. For instance, the body frame moments for the vertical fin are evaluated as follows:

$$M_{VF\_BF} = \begin{bmatrix} M_{xVF} \\ M_{yVF} \\ M_{zVF} \end{bmatrix} + \begin{bmatrix} r_{xVF} \\ r_{yVF} \\ r_{zVF} \end{bmatrix} \times \begin{bmatrix} F_{xVF} \\ F_{yVF} \\ F_{zVF} \end{bmatrix}$$

In the end, the forces and the moments generated by each component are summed together to obtain the overall aerodynamic loads:

$$\begin{aligned} \mathbf{F_A} &= \mathbf{F_{HS}} + \mathbf{F_{VF}} + \mathbf{F_{AF}} + \mathbf{F_{RH}} \\ \mathbf{M_A} &= \mathbf{M_{HS}} + \mathbf{M_{VF}} + \mathbf{M_{AF}} + \mathbf{M_{RH}} \end{aligned} \tag{3.17}$$

3.3 Main rotor wake model

The main rotor is an essential element of a helicopter and is responsible for generating the force needed to sustain the aircraft in its mission. However, the main rotor dynamics also produce a wake that inevitably interacts with most of the parts of the helicopter.

Describing the interference generated by the wake on the aerodynamic surfaces is not straightforward since the wake generated by a rotating wing has a complex structure. CFD analysis and complex iteration with a high computational cost would give a detailed description of the wake behavior and interference with the helicopter components. Still, since the work focuses on developing a model for real-time simulation, a much simpler approach must be followed.

For these considerations, the author has developed a model based on the Theory of Froude. In this way, the wake behavior description is much simpler but still reliable. The wake in the model is assumed to act on the aerodynamic surfaces, which are the airframe, the rotor head, the horizontal stabilizer, and the vertical fin, but also on the tail rotor.

3.3.1 Wake building

The first step in the model is the building of the wake geometry. To complete this work, two laws derived from the Theory of Froude are used (Ref [6]):

$$\frac{v_i(d)}{v_i(0)} = 1 + \frac{d/R}{\sqrt{1+(d/R)^2}} \tag{3.18}$$

$$\frac{R(d)}{R(0)} = \sqrt{\frac{\sqrt{1+(d/R)^2}}{d/R+\sqrt{1+(d/R)^2}}} \tag{3.19}$$

The first law represents the induced velocity at some distance d downstream (or upstream) of the main rotor disk. The second law instead estimates the radius of the stream tube always at some distance downstream (or upstream) of the main rotor disk.

In the hover case, the wake is, therefore, vertical, as shown in Figure 3.10.

However, with the helicopter movement, the steamtube changes its geometry; to define this change, it must be considered the departure or wake angle defined as:

$$\chi = \arctan\left(\frac{u_a}{w_a}\right)$$

In hover, the value of w_a is the induced velocity w_w, and u_a is 0: thus, the wake angle is

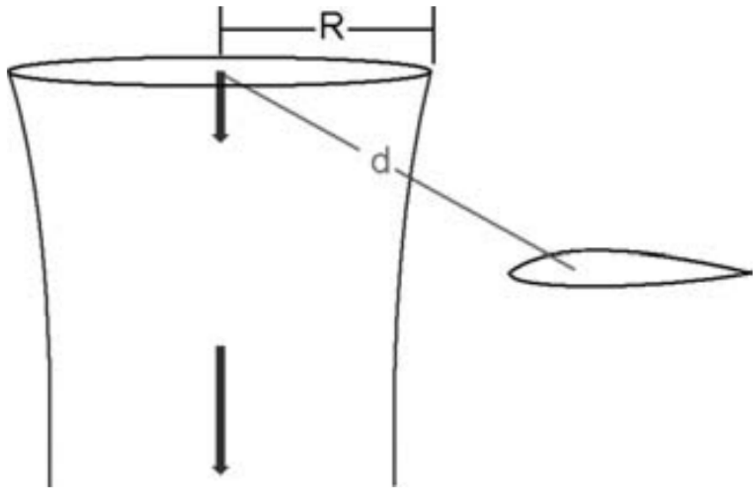

Figure 3.10: Main rotor wake in hover condition [6]

90° at the disc and all along the midline of the streamtube. As the forward speed increases, the wake angle moves away from the vertical, as shown in Figure 3.11.

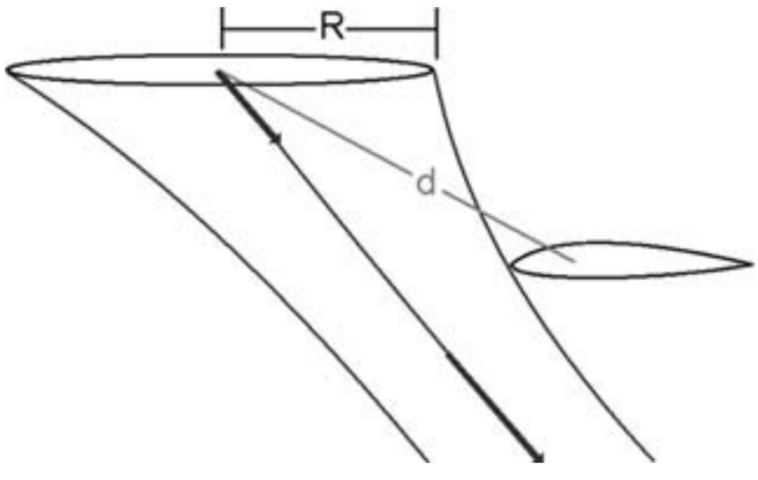

Figure 3.11: Main rotor wake with forward speed [6]

In addition, because the induced velocity in the ultimate wake increase to $2w$, the wake angle will also change: ignoring the contraction of the stream tube but considering the wake acceleration, the wake has a geometry as shown in Figure 3.12.

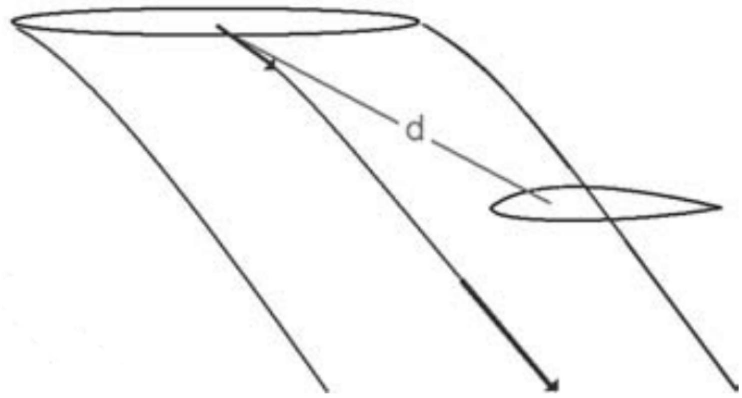

Figure 3.12: Wake acceleration [6]

In the end, another effect must be considered: the main rotor's mast is tilted in the forward direction. This tilt angle influences the wake development, as shown in Figure 3.13, where the contraction of the streamtube and the wake acceleration are not considered.

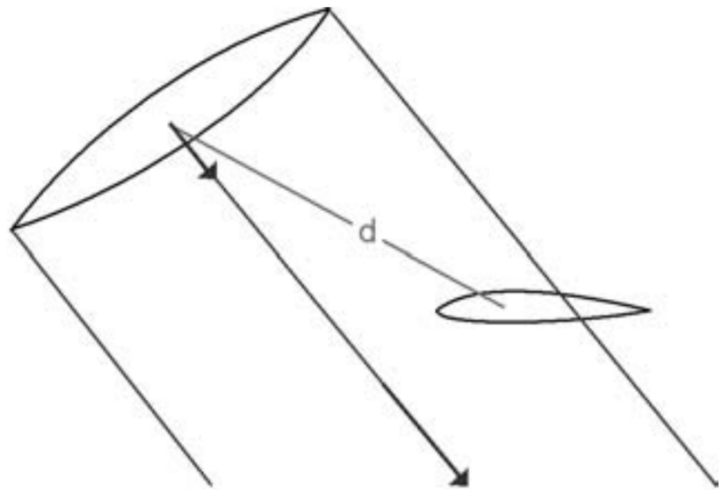

Figure 3.13: Wake with mast tilted [6]

Considering the effects presented and discussed above, the wake geometry is built in this way:

1. The body-axis velocities are resolved in the main rotor hub axis (coincident with the rotor hub reference frame A.5) considering the mast tilt angle, aircraft angular velocities, and the mast's distance from the helicopter center of gravity.

2. The aerodynamic velocity is computed at the hub and at several downstream positions measured in the axial direction by adding to the mast axis velocity the axial induced velocity computed using the induced velocity ratio $v_i(d)/v_i(0)$.

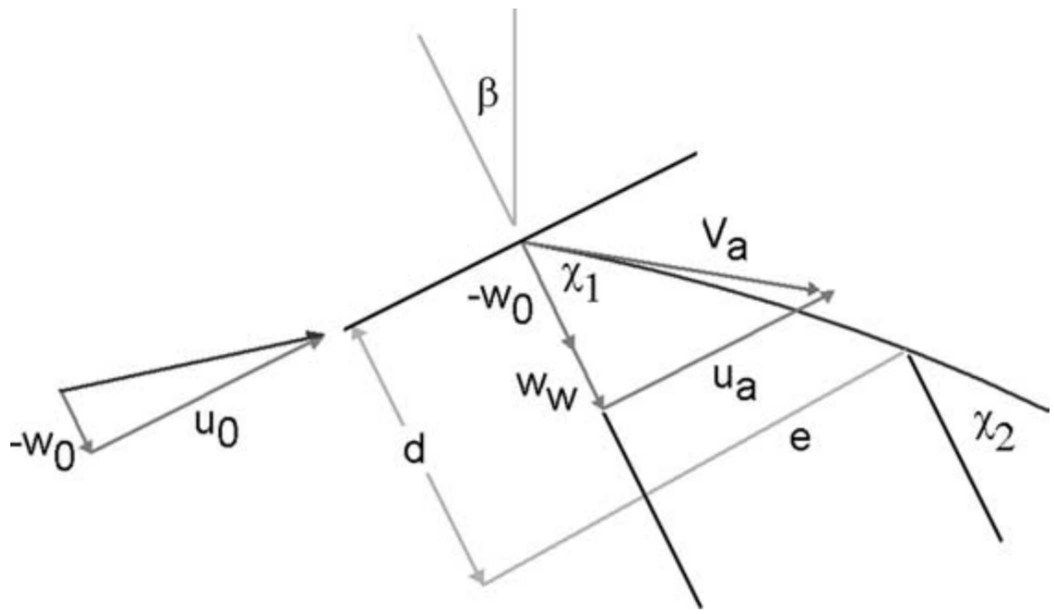

Figure 3.14: Wake midline computation [6]

3. For each station, two wake angles are computed:

$$\chi_X = \arctan\left(\frac{u_a}{w_a}\right) \qquad \chi_Y = \arctan\left(\frac{v_a}{w_a}\right)$$

4. The off-axis displacement of the wake midline in each direction is estimated by the integral

$$e_x = \int_0^d \tan(\chi_X)ds \qquad e_y = \int_0^d \tan(\chi_Y)ds$$

where s is measured along the mast axis. This step is shown in Figure 3.14.

5. After obtaining the midline geometry, the radius contraction $R(d)/R(0)$ is used to estimate the wake radius for each station. The wake radius is then centered on the midline, and the section for each station is considered normal to the main rotor axis and parallel to the main rotor disk.

The wake geometry is thus obtained, and all the essential effects are considered.

3.3.2 Interference coefficient

To define how severe is the interference of the wake on the aerodynamic surface, an interference coefficient is evaluated: this interference coefficient is based on the portion of the surfaces of each component wetted by the wake compared to the component surface.

In general, the interference coefficient is thus defined as follows:

$$K_{interf} = \frac{S_{wet}}{S_{ref}} \tag{3.20}$$

For each component, a reference area is then evaluated:

- For the horizontal stabilizer, the reference area is the planform area given by the product of wingspan per chord.
- For the vertical fin, the reference area is also the planform area considering the fin as a parallelogram.
- For the tail rotor, the reference area is expressed as the disk area.
- For the airframe, an ellipsoid surface is defined with the main dimensions of the fuselage

An interference coefficient is not evaluated for the rotor head since this component is always entirely affected by the rotor wake.

Defining the position of the reference areas and knowing the geometry of the wake, the wetted surface for each component is evaluated by computing the amount of reference surface inside the wake.

3.3.3 Wake induced velocity

The calculation of the wake-induced velocity is the last step and represents the output of the main rotor wake model. With the model introduced, the wake influences the various components by inducing a downwash component whose direction is parallel to the mast and with a module given by the ratio $v_i(d)/v_i(0)$ multiplied by the main rotor-induced velocity. The downwash component on each element is then multiplied by the interference factor to decrease the wake effect if the aerodynamic surface is not entirely inside the wake.

The model developed is very simple and ignores some critical effects of the wake, like the vorticity; however, this approximation is inevitable to avoid using a model with a high computational cost.

Chapter 4

Implementation of the Simulink model

Once the models of the tail rotor, wake, and aerodynamic surfaces were defined, a representative model of the helicopter's flight mechanics was created. Since the ZHAW flight simulators (the ReDSim and the HiSim) work using the MATLAB/Simulink® environment, the simulation model has been developed accordingly.

The structure of the implemented helicopter model is the same as the structure of the models already realized within the *ZAV*, such as the one created for the *Implementation of a real-time simulation model of a tilt-rotor aircraft* [1].

4.1 Helicopter model

The top-level architecture of the helicopter model is organized as shown in Figure 4.1. It can be seen that the input *U*, which represents the controls from the pilot interface and from the actuation system model eventually mixed in a mixer, is sent as inputs to the main rotor and tail rotor model. The subsystem called *Weight & Balance* computes the aircraft's moments of inertia and center of gravity position. Five blocks evaluate the forces and moments produced by all the major components of the aircraft:

- The *Main Rotor* block evaluates the forces and moments developed by this component as well as the wake downwash acting on the aerodynamic surfaces and the tail rotor.

- The *Tail Rotor* block evaluates the forces and moments developed by the tail fan and the forces produced by the shroud.

- The *Aeordynamics* block evaluates the forces and moments produced by the airframe, the rotor head, the vertical fin, and the horizontal stabilizer.

- The *Landing gear* block evaluates the loads produced by the helicopter skid.

- The *Gravity* block evaluates the gravity force acting on the helicopter in terms of intensity and direction.

The forces and moments evaluated within the different subsystems are then summed in a specific block. The helicopter loads are then fed to the *Equation of motion* block, which evaluates the helicopter dynamics and cinematics, i.e., the position, the attitude, and the linear and angular velocities and accelerations, and feeds back these values to the other subsystems. The helicopter motion is also fed to the *Environment* subsystem, which evaluates the standard parameters of the atmosphere like the air temperature, the air density, and helicopter Mach number. These environmental parameters are used in almost all the other blocks.

Among the blocks presented, the *Tail Rotor* block, the *Aerodynamics* block, and the *Main Rotot Wake* block inside the *Main rotor* block have been developed by the author. The other subsystems were not part of this thesis work.

4.2 Tail rotor

4.2.1 Model architecture

The tail rotor model architecture reflects the different parts discussed in the chapter relative to the tail rotor model. From Figure 4.3, it can be seen that in the proper tail rotor model, there are three main subsystems, which are:

- The *Fan Forces and Moments* subsystem, where the loads produced by the tail fan are evaluated.

- The *Duct Forces* subsystem, where the forces produced by the shroud of the tail rotor are evaluated.

- The *Inflow* subsystem, which is influenced by both the Fan and the Duct subsystem, since the first provides the Fan thrust while the second provides the velocity ratio. The inflow subsystem evaluates the induced velocity on the fan through the use of the inflow dynamic equation and then feeds the velocities back to the Fan Forces and Moments subsystem.

The forces and moments produced by the Fan and the forces produced by the duct are then summed and converted into the body reference frame in order to be summed with the loads evaluated in the other blocks. These loads represent the main output of the tail rotor model block.

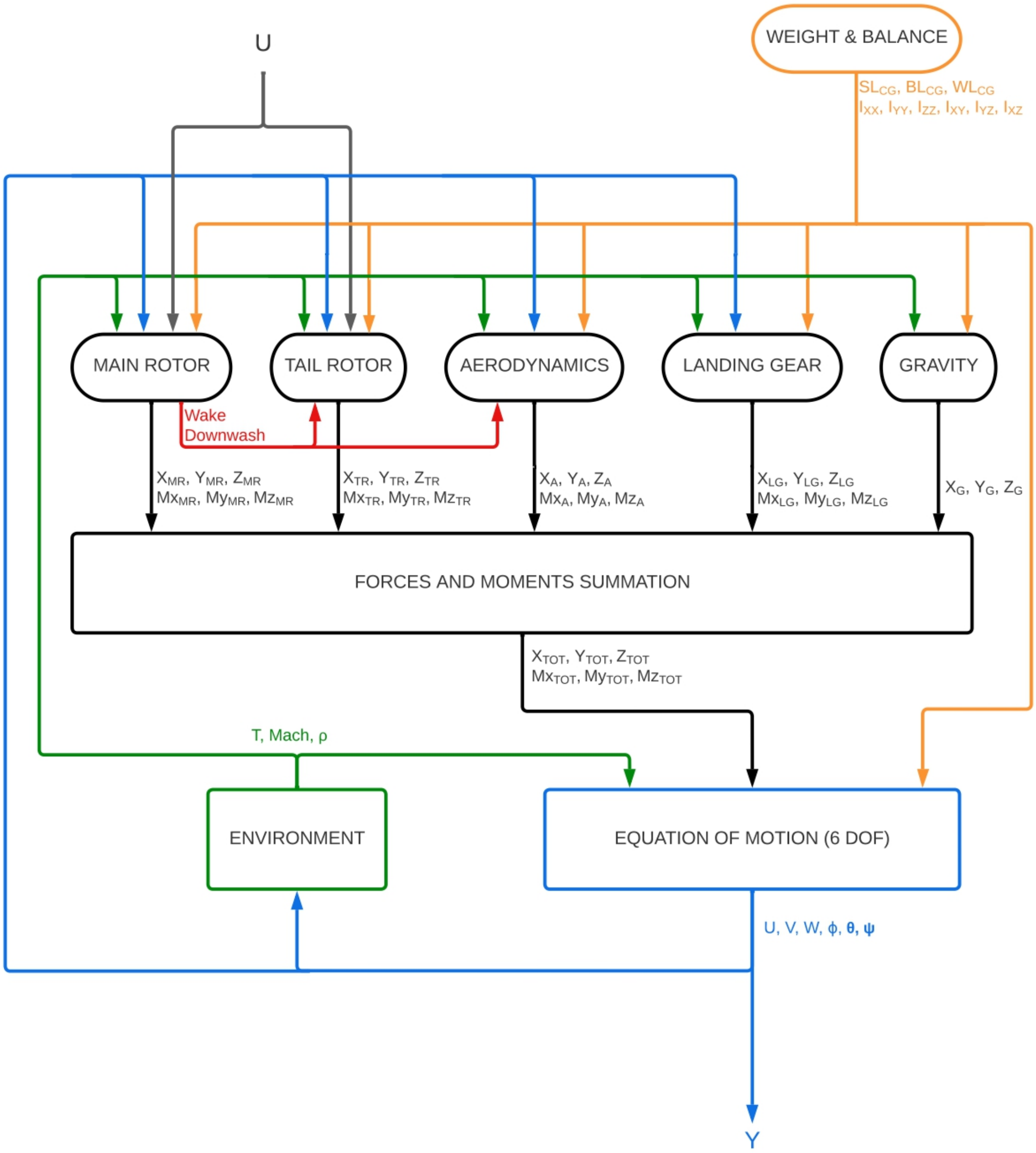

Figure 4.1: Top-level architecture of the helicopter model

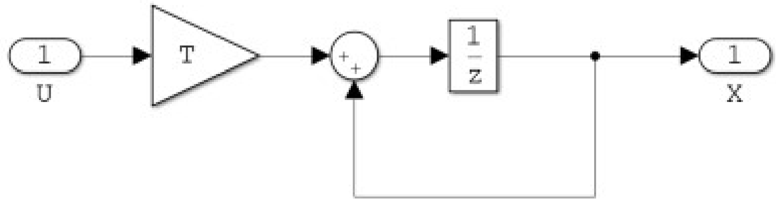

Figure 4.2: Euler Explicit Integrator scheme

Before the proper tail rotor model, instead, the local velocities are evaluated considering the helicopter motion, the main rotor wake influence, and the helicopter's center of gravity position. Besides these last factors, the other inputs to the system are the environmental parameters, particularly the air density and Mach number, but also the control, which is the pedal position, coming from the pilot or the actuation system.

4.2.2 Integration of the inflow dynamic equation

The inflow dynamic equation to be resolved in the Inflow subsystem are differential equation. To comply with real-time requirements, all simulation is time-discrete, which means that time is supposed to move forward in steps of equal duration, and the simulator solves model equations successively. As a result, discrete-time-step solvers must be implemented. Using a simple first-order Forward Euler Method has been chosen to solve the equation. The explicit formulation of the Euler Method is as follows:

$$y_{n+1} = y_n + h f(t_n, y_n) \tag{4.1}$$

In the Equation, h represents the simulation sampling time. With blocks, this first-order discrete integrator has the architecture shown in Figure 4.2

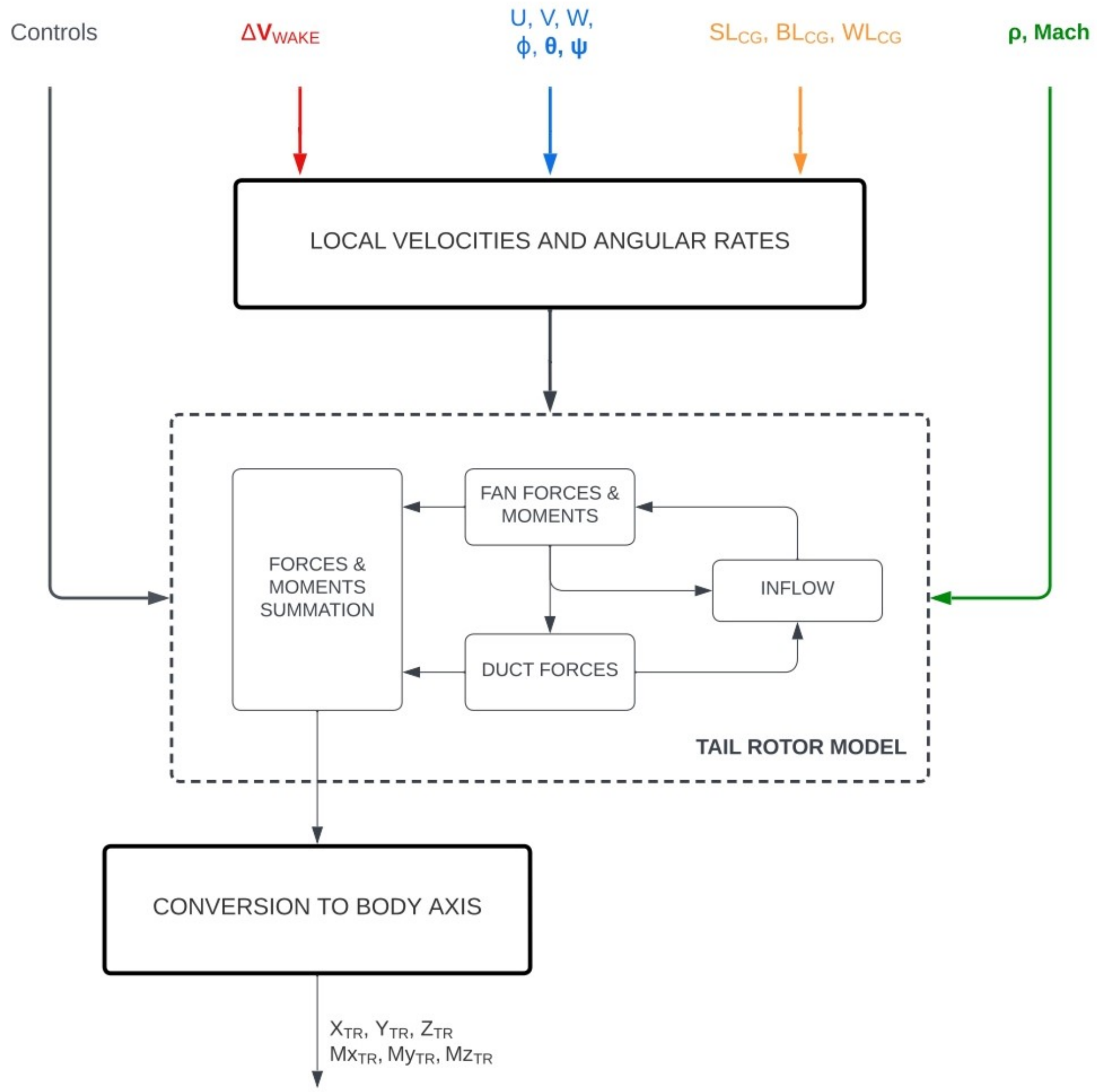

Figure 4.3: Scheme representing the tail rotor model

4.3 Aerodynamics

The *Aerodynamics* block contains the four subsystems representing the main helicopter aerodynamic surfaces that produce loads during the flights.

The model's overall structure is presented in Figure 4.4. It can be seen that the main inputs to the system are:

- The helicopter motion, which influences the flow velocities on each component.
- The air density.
- The helicopter's center of gravity position.
- The main rotor wake downwash effect on the several aerodynamic components.

All these inputs are fed to all the component models. The outputs of the models, which are the loads produced and evaluated in the body reference frame by each surface, are then summed in a dedicated block. The overall aerodynamic loads represent the outputs of the aerodynamics block.

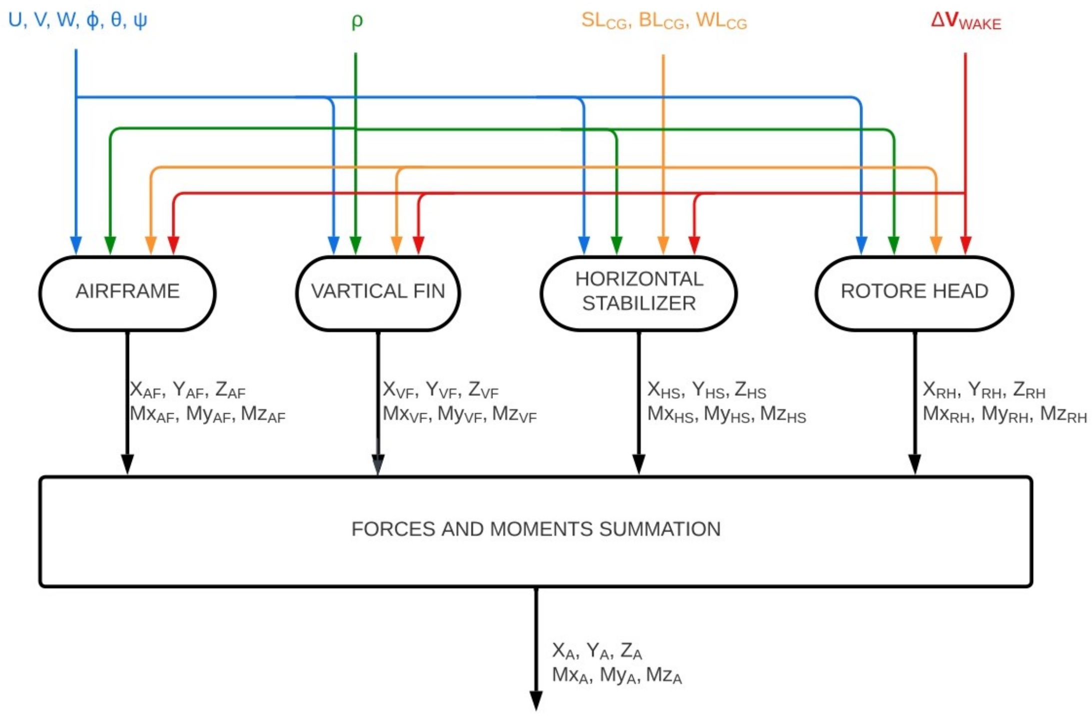

Figure 4.4: Scheme of the Aerodynamic model

4.3.1 Airframe, Rotor Head and Vertical Fin model architecture

As discussed in Chapter 3.2, the general model of an aerodynamic component calculates the loads evaluating the local dynamic pressure and aerodynamic angles.

Figure 4.5 shows the structure of the Airframe, Rotor Head, and Vertical Fin model. For each component, the local velocities are first evaluated considering the helicopter motion, the main rotor wake downwash, and the helicopter's center of gravity position. These velocities are used to evaluate the local angle of attack and the local angle of sideslip of each aerodynamic surface. In addition, together with the air density, it is evaluated the local dynamic pressure. Thanks to a 2D look-up table, the aerodynamic angles allow the evaluation of the aerodynamic coefficients. Ultimately, the forces and moments in the body reference frame are calculated with the aerodynamic coefficients, the local dynamic pressure, and the helicopter's CoG position.

4.3.2 Horizontal Stabilizer model architecture

The model developed for the horizontal stabilizer, as seen in Chapter 3.2, is slightly different from the others since the air compressibility is considered owing to its position directly under the main rotor. Thus, in this case, the model is the same, but instead of the sideslip angle, the local Mach number is evaluated, and, with the local velocities, the 2D Look-up tables allow obtaining the aerodynamic coefficients from these two parameters. The scheme for the Horizontal stabilizer is shown in Figure 4.6.

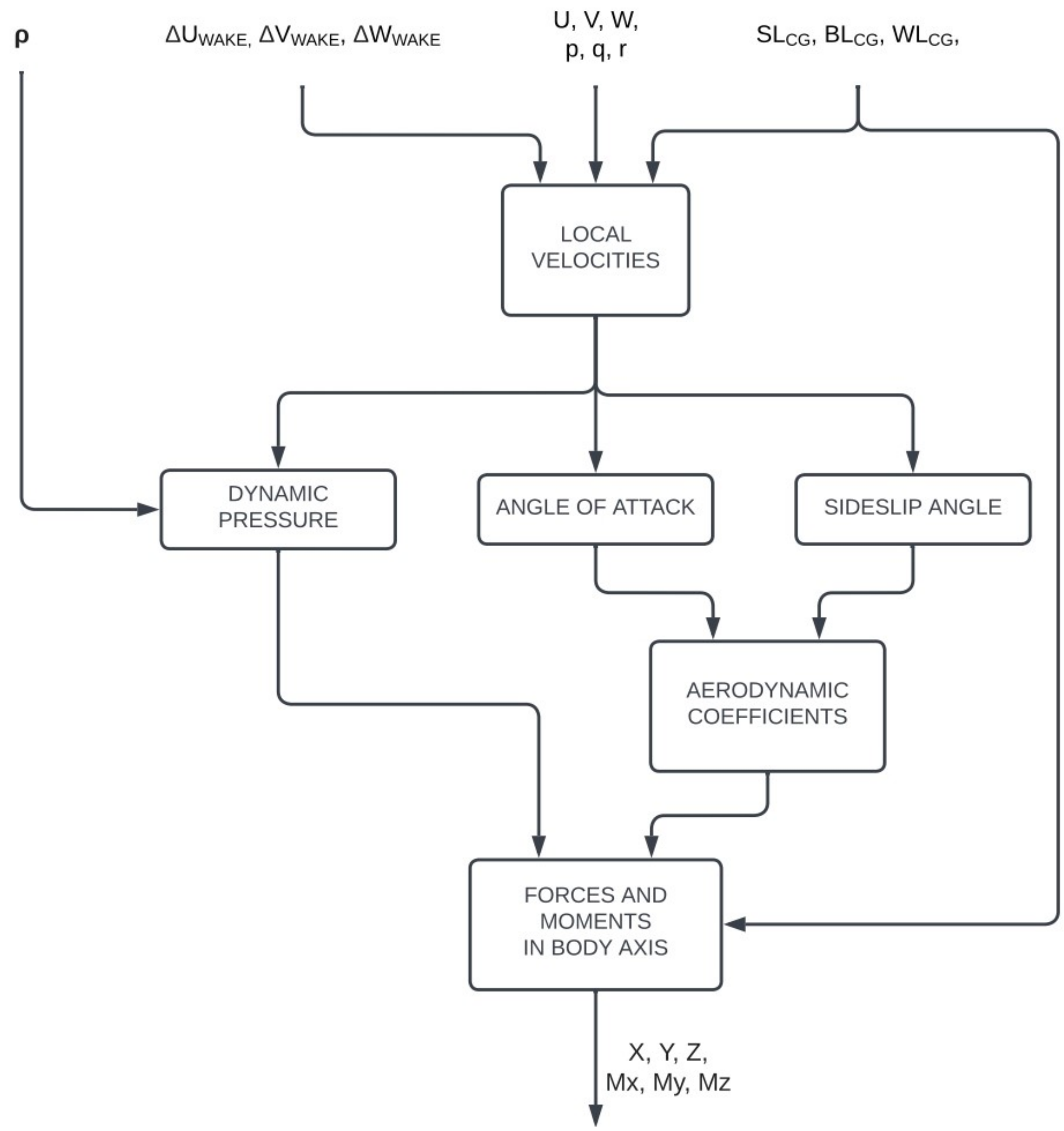

Figure 4.5: Scheme of the Airframe, Rotor Head, and Vertical Fin model architecture

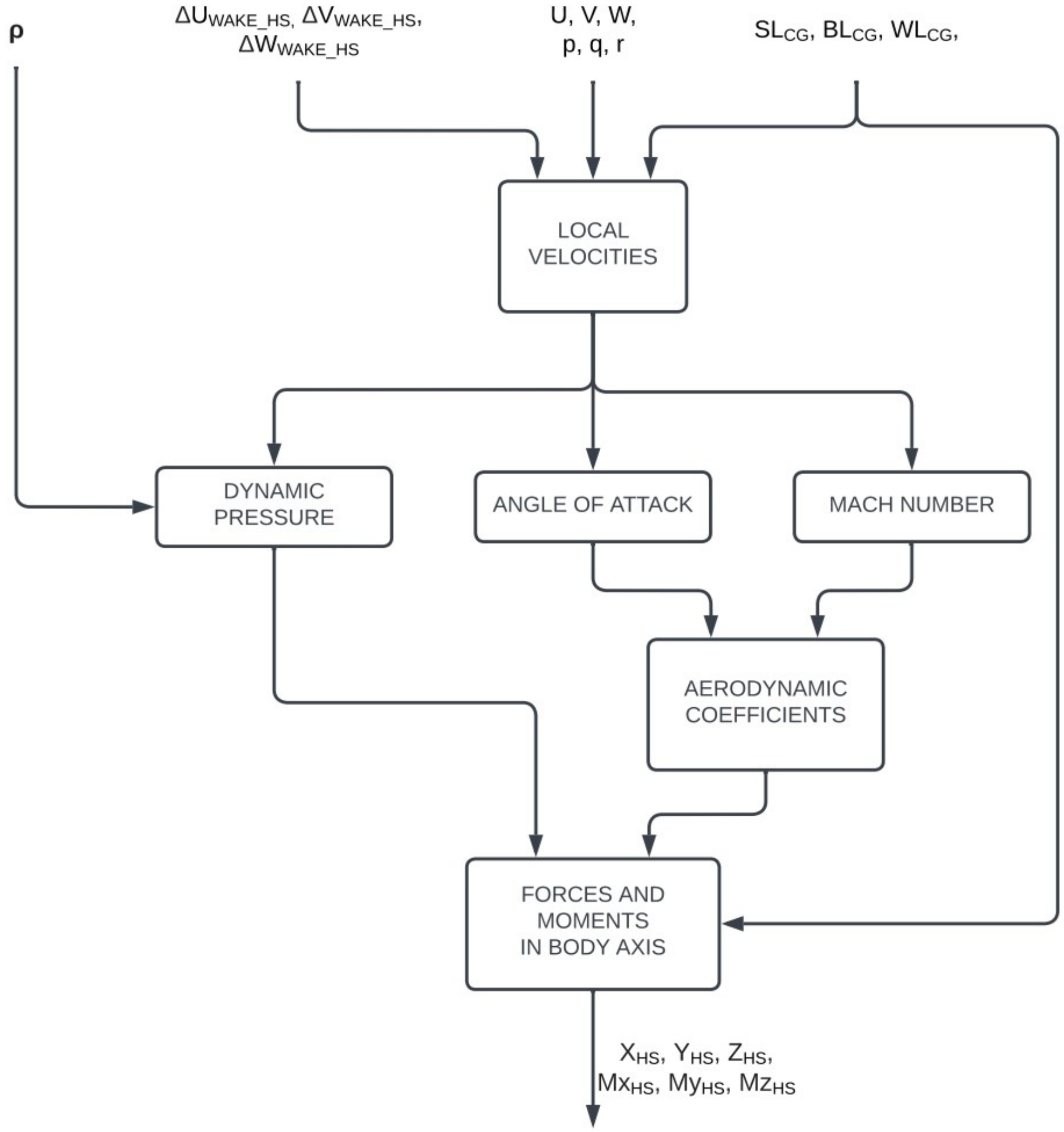

Figure 4.6: Scheme representing the Horizontal Stabilizer model architecture

4.4 Main rotor wake

The *Wake* block is responsible for evaluating the main rotor wake effect on the other helicopter components. This block is contained inside the *Main Rotor* block since it strictly depends on the main rotor parameters. As shown in Figure 4.7, the structure follows the step shown in the relative chapter 3.3. The *Wake* block is composed of three main subsystems:

- The *Wake building* block, where the geometry of the wake is built in terms of midline position and wake radius for different stations considered along the main rotor axis.
- The *Interference* block, which evaluates the interference for each component considering the total surface area of the component and the area wetted by the wake.
- The *Downwash* block, which evaluates the downwash components in terms of velocity on each surface. The components are evaluated in the body reference frame.

The input of the system is the main rotor-induced velocity parameter λ_{MR} together with the local velocities of the main rotor, which are evaluated in the main rotor hub reference frame considering the helicopter motion and the helicopter's center of gravity position. As already discussed, the system outputs are the wake-downwash components in the body reference frame in terms of velocity on each surface.

Figures 4.8 and 4.9 show the wake structure in a generic hover case. These figures highlight how the components are considered for the interference coefficient evaluation:

- For the horizontal stabilizer, the plan surface area is considered, and it is assumed that this surface is parallel to the aircraft $X-Y$ plane.
- For the vertical fin, the plan surface area is considered, and it is assumed that this surface is contained in the aircraft $X-Z$ plan.
- For the tail rotor, a circle area is considered with a radius equal to the fan radius, and it is assumed that this surface is contained in the aircraft $X-Z$ plane.
- For the airframe, a 3D surface is considered, but for simplicity's sake, the airframe is assumed as an ellipsoid instead of considering the real geometry.
- For the rotor head, since this component is part of the main rotor and, as a consequence, is always affected by the main rotor wake, it is assumed that the interference coefficient is always 1, which means that all the rotor head surface is wetted.

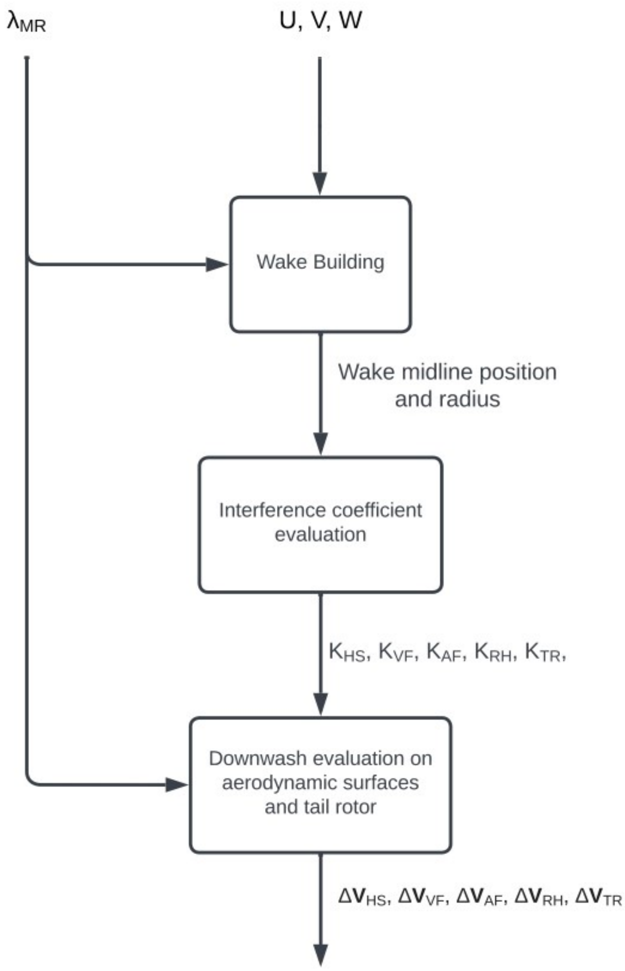

Figure 4.7: Scheme of the main rotor wake model

The downwash components of the wake in the body reference frame are evaluated at specific points on the surface, and it is assumed that over the entire surface, there is the same downwash evaluated at the specific point. This approximation is valid for some components like the vertical fin or the rotor head but is less accurate for components such as the airframe, which is very large, and its different parts are subjected to different downwash.

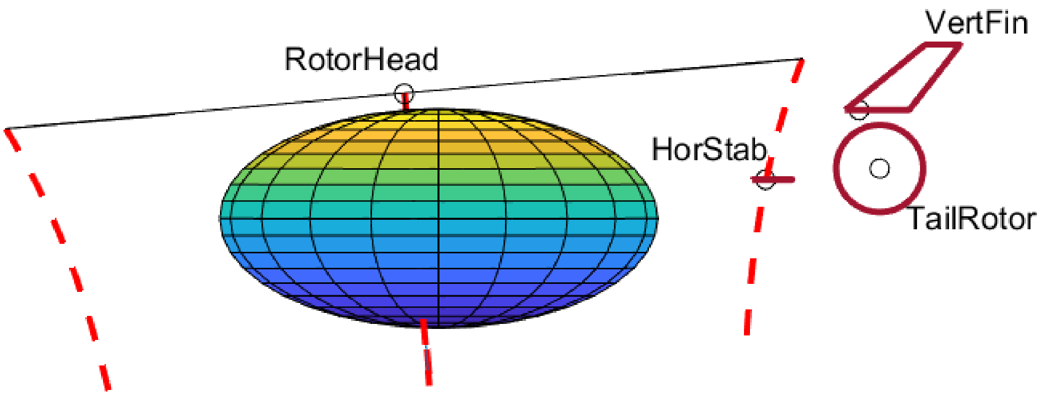

Figure 4.8: Lateral view of the wake

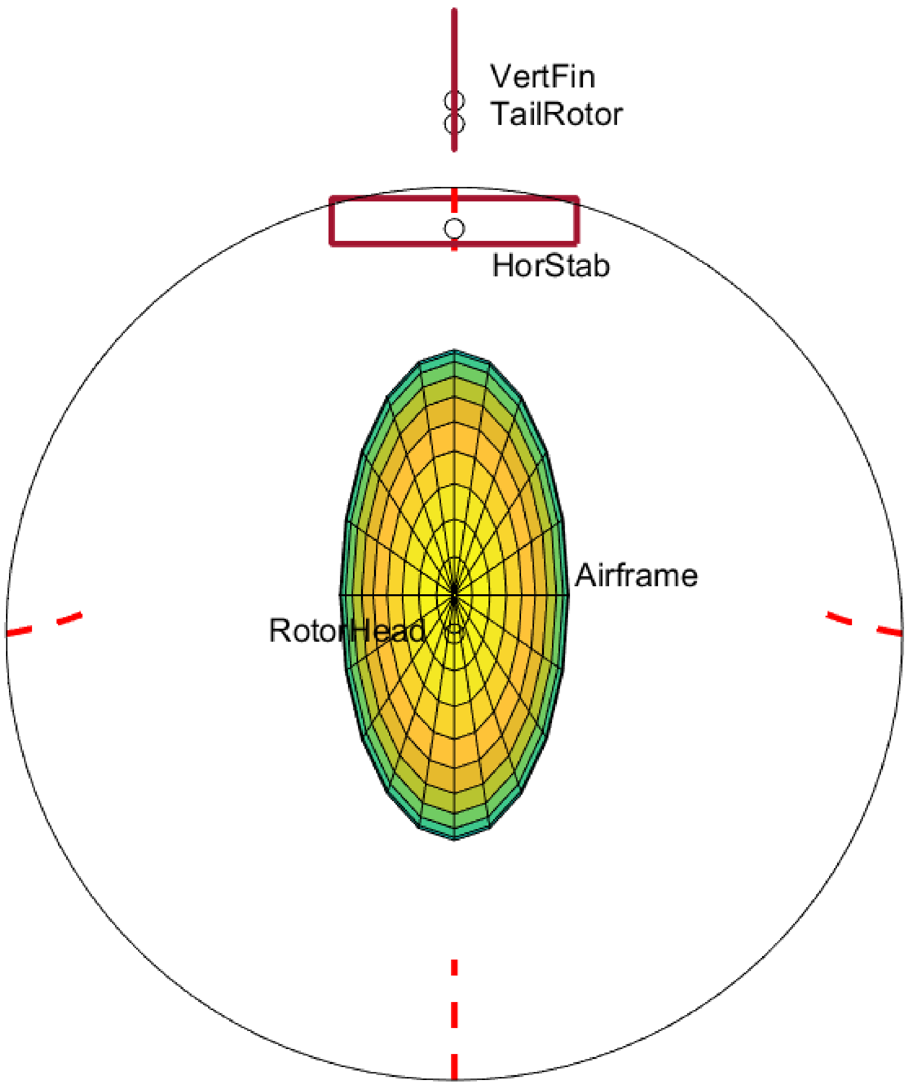

Figure 4.9: Top view of the wake

Chapter 5

Main results

After the implementation of the mathematical models in MATLAB/Simulink®, it has been possible to obtain some results. Unfortunately, a simulation of the complete helicopter was not possible since only the *Tail Rotor* model, the *Aerodynamics* model, and the *Main Rotot Wake* model have been developed by the author. The other components were not part of the author's assignments but will be the objects of another thesis, and the integration was out of the scope of this work. Only the result of the implemented components will be shown in this chapter. In particular, the model of the tail rotor will be shown first, and it will be analyzed isolated to show its behavior in different conditions; lastly, some trim points in hover and forward flight conditions will be studied through the comparison with a reference model.

5.1 Isolated Tail Rotor

The first analysis of the model of the ducted tail rotor is carried out, considering this component is isolated from the rest of the helicopter. This analysis provides an opportunity to show the main performance of the tail rotor and to check whether its behavior is similar to predictions reported in the literature or made by other simulation tools.

5.1.1 Hover condition

The first result that can be studied is the tail rotor behavior when the aircraft is not moving, no external wind is present, and the main rotor wake influence is neglected. So, in this case, the tail rotor stands still in the air.

Figure 5.1 shows some results of thrust and torque as a function of the pedal position. In each plot are reported the data from the simulation of the implemented model as well as data measured from a bench test. It can be seen that, in general, the results of the tail rotor model implemented follow the trend of the results of the bench test. The significant deviations appear in the modeling of the duct thrust: for high positive pedal positions, and when the duct thrust is close to zero, the model fails to follow the real behavior, and the duct thrust is overestimated. However, since the errors are minor, the effect on the tail rotor's total thrust is negligible, and the overall relative error is under 5%. Another effect the model does not capture is the hysteresis visible in the measured data: for simplicity's sake, it has been chosen not to consider this effect.

Regarding the torque results, the model tends to overestimate the torque response for positive pedal positions slightly. In contrast, for negative pedal positions, the data of the implemented model suggest an underestimation of the torque response. The relative error for these cases is at most 10%.

5.1.2 Tail rotor movement

The next step in analyzing the tail rotor model implemented is the study of its behavior when the helicopter is moving or, in the general case, that same air is flowing on the tail rotor due to external wind or main rotor wake influence. Therefore, a velocity vector expressing the velocity of the tail rotor hub reference frame is defined:

$$\mathbf{V_{TR}} = U\mathbf{i} + V\mathbf{j} + W\mathbf{k}$$

Where the vector **i**,**j**, and **k** identify the directions of the three axes of the tail rotor Hub reference frame.

It is reminded, however, that the tail rotor is always considered isolated.

The results presented in the following sections have been obtained to study and map the mathematical model developed, although they have not been validated with any source of experimental data.

Pure forward flight

The first analysis consists in assuming a velocity along the X_{Hub} axis of the tail rotor reference frame: thus, in this case, only the component U of $\mathbf{V_{TR}}$ is assumed, while V and W are considered null. This analysis is intended to study the behavior of the tail rotor when the helicopter is in pure forward flight.

In Figure 5.2, the charts of the trust and torque are reported. These characteristics are evaluated as functions of the external velocity U and the pedal position. It can be seen that with the increasing forward velocity, the tail rotor thrust and torque increase considering the same pedal position, except for high positive and negative pedal positions where a stall region appears. Furthermore, the typical flat region visible when the external velocity is null ($U = 0$) and the thrust is close to zero slightly disappears when a velocity is present ad the tail rotor is out of hover conditions.

Another interesting parameter to study is the thrust share, introduced in Chapter 3.1 as the ratio between the fan thrust and the total thrust of the tail rotor. Figure 5.3 shows how the pedal position and external velocity influence this parameter. First of all, it can be seen that when there is no external wind ($U = 0$), this parameter switches between two values, and there is a consistent jump: this is due to the fact that the duct is more efficient when there is no external velocity and the helicopter is in hover conditions, and so the switch from normal thrust conditions to reverse thrust conditions is more significant. With the increasing velocity along X_{Hub} axis, two effects can be identified: the first is that the thrust share generally increases, meaning that the contribution of the duct to the tail rotor thrust is lowering. The second effect is that the jump between normal thrust conditions and reverse thrust conditions decreases until there is no jump anymore: this is because the thrust share is strictly related to the velocity ratio and its behavior with the external velocity, shown and discussed in Section 3.1.4 in Figure 3.6.

Pure lateral flight

Another interesting analysis is studying the behavior of the implemented tail rotor model when a velocity component is present along Z_{Hub}. Thus, only the component W of the velocity $\mathbf{V_{TR}}$ is assumed, while U and V are considered null. With this analysis is possible to study the effect that the aircraft's lateral movement has on the tail rotor.

In Figure 5.5, the plots of the thrust and torque are reported. As in the previous section, these characteristics are evaluated as a function of the external velocity W and the pedal position. It can be seen that, in general, for positive values of W (meaning that the relative air is flowing from the diffuser to the inlet), the thrust increase in modulus for positive pedal positions under nominal thrust conditions. At the same time, the thrust decreases in reverse thrust conditions with negative pedal positions. This is due to the fact that in nominal thrust conditions, the external velocity is opposite to the induced velocity of the tail rotor. In contrast, the two velocities are in the same direction in reverse thrust conditions. This result is in accordance with the momentum theory for an open rotor in a vertical climb, which expressions are given in reference [8].

It is reminded that in nominal thrust conditions, the thrust is negative because it is opposite to Z_{Hub} while the induced velocity is positive because it is in the same direction as Z_{Hub}.

It must also be noted that when the induced velocity and the external velocity are comparable but in the opposite direction, in reality, a vortex region appears, and the model does not capture this non-linearity. Another strange behavior appears when the thrust is close to zero. It can be seen that for conditions where W is not null, the curves pass two times the X axis, and so for two times, they are close to zero. This problem will be explained in the next section, where this effect is more visible.

Lastly, it is possible to study the thrust share. Figure 5.4 shows how this parameter is affected by the lateral velocity of the helicopter. It can be seen that in hover conditions, ($W = 0$), there is the lowest thrust share because, in this condition, the duct is much more efficient. The velocity affects the tail rotor performance by decreasing the duct efficiency, so the thrust share increases with the increase of the velocity W. It can also be noted that for the same value in modulus of velocity, the thrust share jump between identical values. The difference is the pedal position at which the jump occurs, and this is due to the direction of the external velocity and its direction compared to the direction of the induced velocity: in nominal thrust condition, when the velocity W is positive, the relative flow velocity is negative, and so it is in the opposite direction of the induced velocity of the fan. This effect delays the transition between nominal and reverse thrust conditions, so the jump of the thrust share occurs at much negative pedal positions.

Effect of the helicopter sideslip angle β

In this last section, it is evaluated the general behavior of the tail rotor with velocity components along X_{Hub} and along Z_{Hub}: so, in this case, the velocity is $\mathbf{V_{TR}} = U\mathbf{i} + W\mathbf{k}$. The component $V\mathbf{j}$ is neglected for simplicity's sake and because U and V are both defined as in-plane velocity, and they have the same effect on the tail rotor behavior. However, since this analysis aims to study the helicopter sideslip angle effect on the tail rotor, it is considered a constant velocity $U = 80\,kts$, and W is changed to vary the angle β.

In Figure 5.6, the charts of the thrust and torque are reported. As in the previous sections, these characteristics are evaluated as functions of the velocity $\mathbf{V_{TR}}$ and pedal positions. In these results, it is possible to see both the effect already seen in the previous section of the forward and lateral velocity of the helicopter. For high positive pedal positions, the stall region is present, and it can also be seen that, considering a specific pedal position, the thrust increase in modulus for positive pedal positions, which means nominal thrust conditions. At the same time, it decreases in reverse thrust conditions with negative pedal positions.

Figure 5.8 also highlight the detail of the tail rotor thrust already introduced in the previous section, but it is much more visible here. It can be seen that when a W component is present, the curves reach the value of zero thrusts for two pedal positions, and one of these two positions is always the same for every curve. This behavior is bizarre, and it is because, in that pedal position zone, the induced velocity is zero or is opposite to the velocity W. In particular, the point that is in common between every curve is reached when the induced velocity and W are equal but in opposite directions. At the same time, the other zero is the one that is due to the induced velocity reaching the value of zero. Between the two zeros, there's a region where the velocity component along Z_{Hub} is greater in modulus than the induced velocity, so the tail rotor works as a *windmill*. Figure 5.9 shows how the increasing of the descent velocity affects the tail rotor behavior: as it can be seen, in slow descent conditions, when the induced velocity is greater than the velocity W, the descent velocity has the effect of creating a vortex region that, with the increasing of W, lead to a vortex ring region conditions where some vortex are generated at the blade tip. In moderate and fast descent, when the external velocity W exceeds the induced velocity, the flow produces a torque on the shaft, which begins to drag the rotor. That's what happens in the region between the two zeros. Nevertheless, this is a very critical zone in the polar since the velocities are minimal and the opposite direction of W and the induced velocities produces a vortex region which is an aerodynamic instability and is not predictable accurately by the model. The results obtained for this region must be taken carefully.

The thrust share plot is the last interesting chart to examine in this section. Figure 5.7 report how this parameter change for every case. It can be seen that no jumps are present, meaning that the thrust share is very high, and the duct contribution to the total tail rotor thrust is minimal. This is due to the high value of the module of $\mathbf{V_{TR}}$ that also implies that the law for the velocity ratio is the same for nominal and reverse thrust conditions (Figure 3.6). In the end, for the same reasons discussed above, the thrust share for a velocity along Z_{Hub} in a positive direction is the same for a velocity along Z_{Hub} in a negative direction.

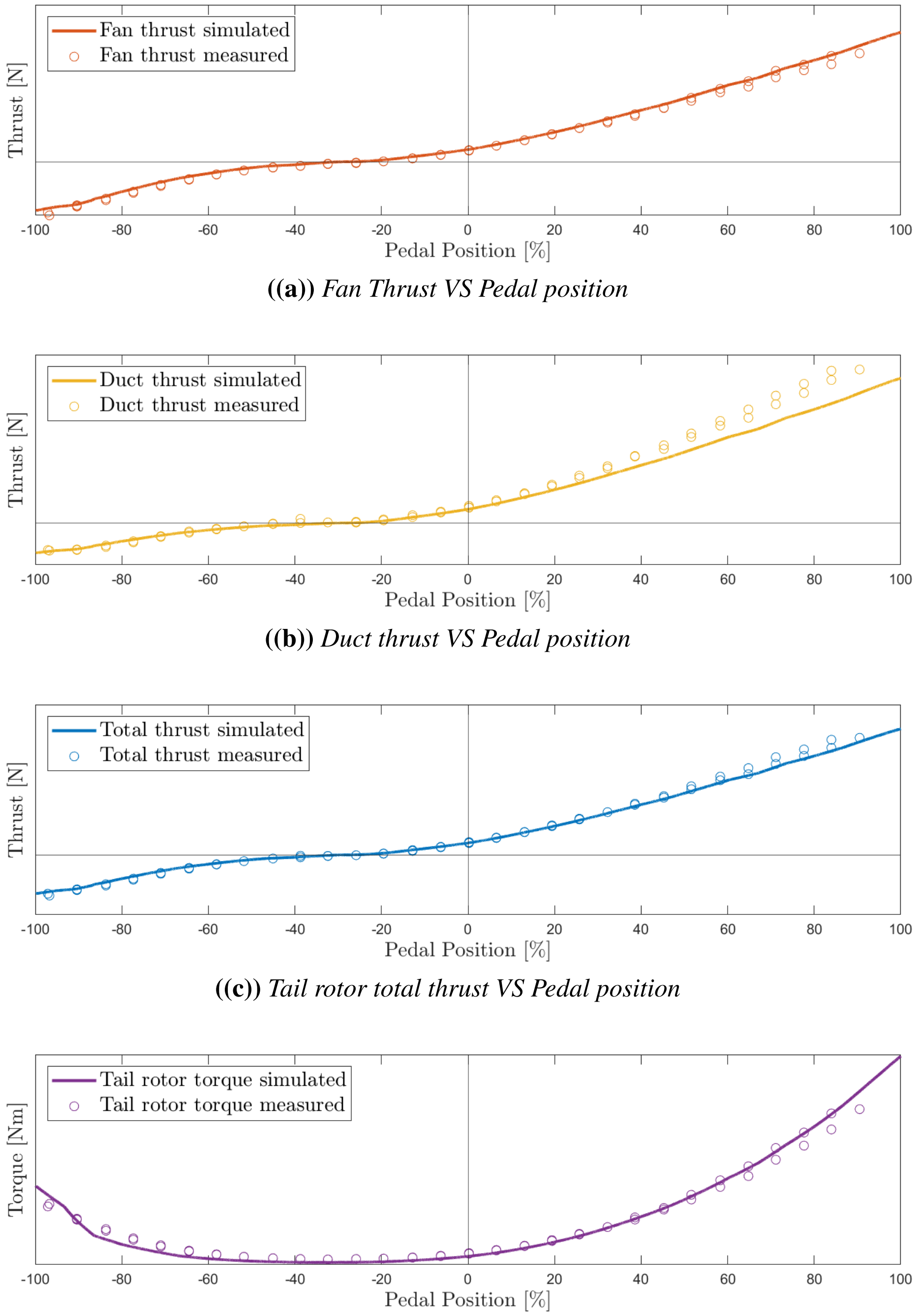

((a)) *Fan Thrust VS Pedal position*

((b)) *Duct thrust VS Pedal position*

((c)) *Tail rotor total thrust VS Pedal position*

((d)) *Tail rotor torque VS Pedal position*

Figure 5.1: Isolated tail rotor in hover conditions

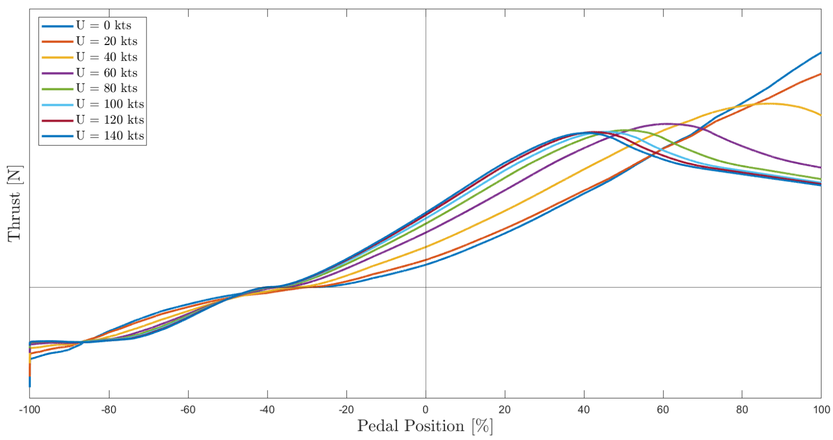

((**a**)) *Tail rotor thrust VS Pedal position VS U*

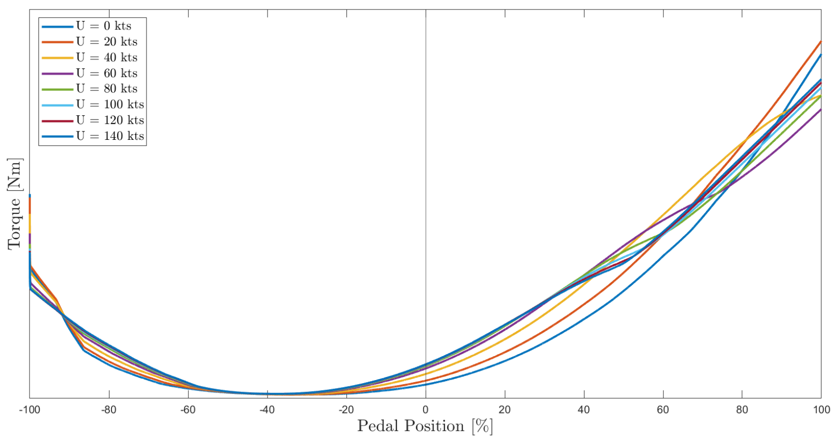

((**b**)) *Tail rotor torque VS Pedal position VS U*

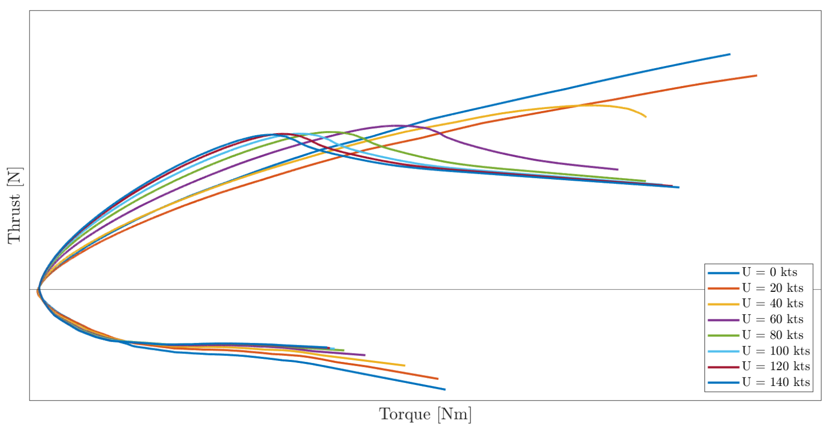

((**c**)) *Tail rotor thrust VS Tail rotor torque VS U*

Figure 5.2: Isolated tail rotor with a velocity component along X_{Hub}

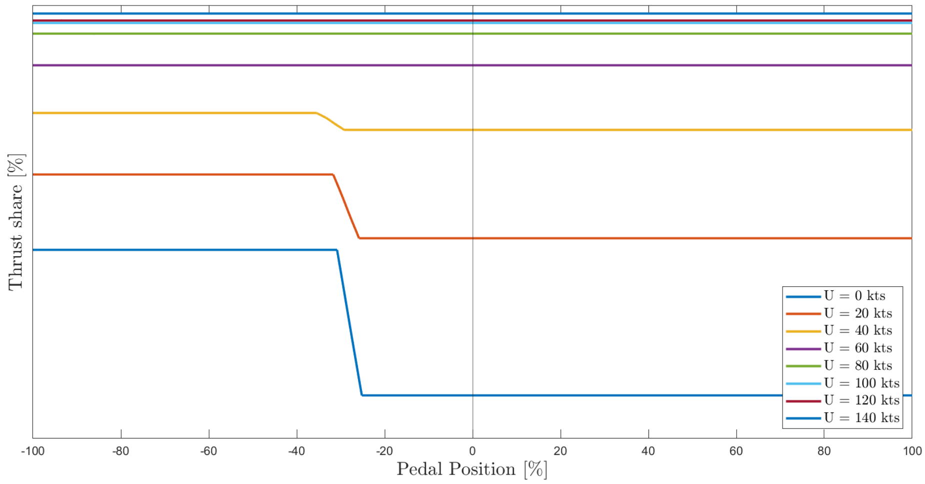

Figure 5.3: Thrust share with pedal position and external wind along X_{Hub}

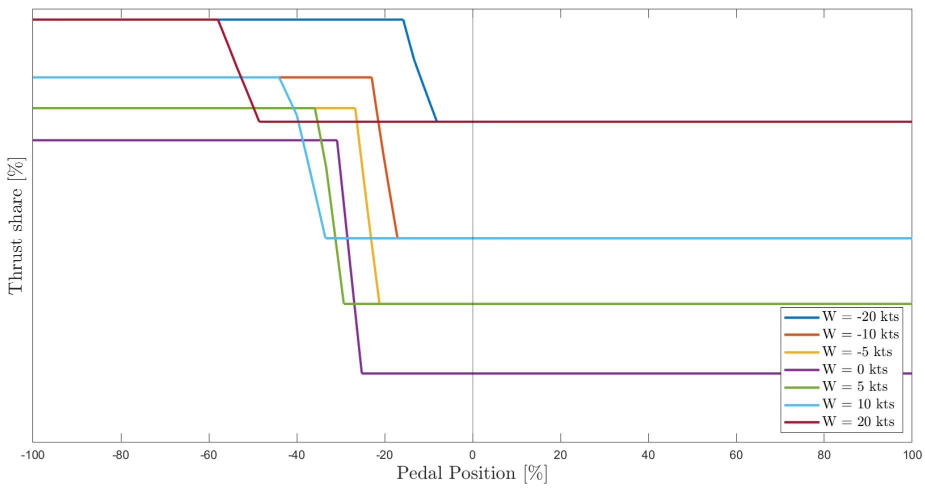

Figure 5.4: Thrust share with pedal position and external wind along Z_{Hub}

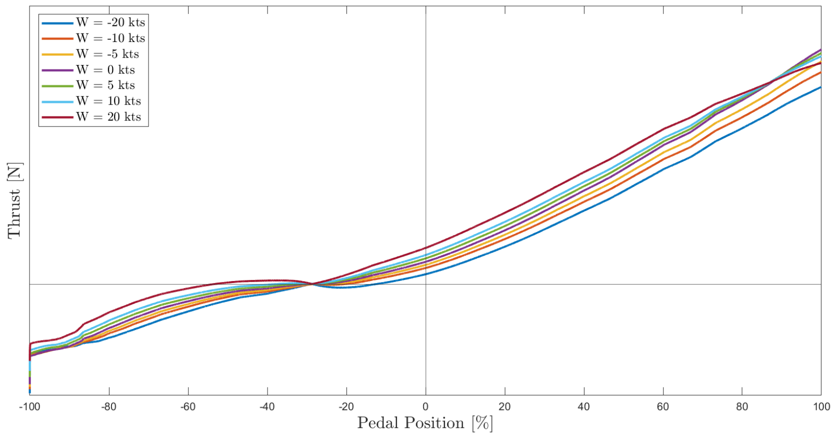

((a)) *Tail rotor thrust VS Pedal position VS W*

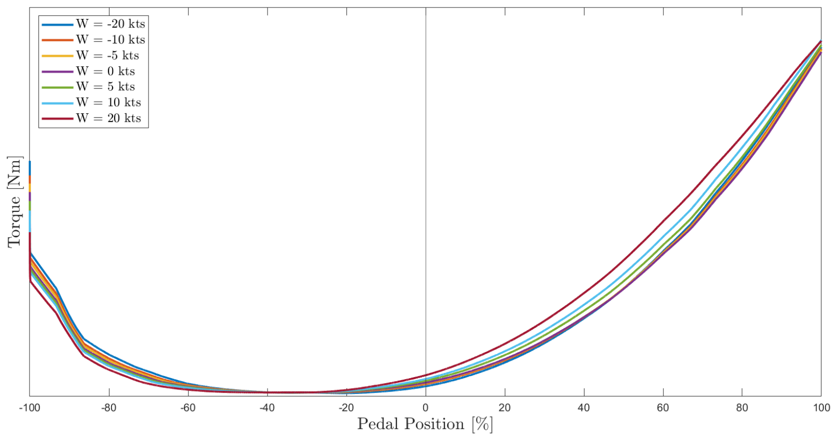

((b)) *Tail rotor torque VS Pedal position VS W*

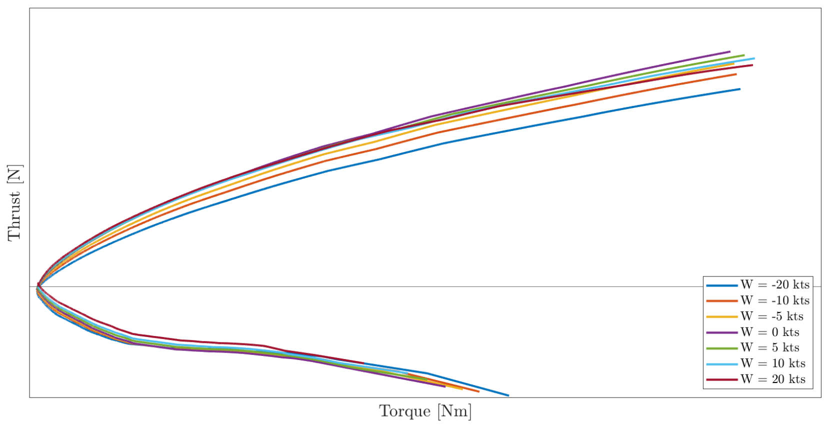

((c)) *Tail rotor thrust VS Tail rotor torque VS W*

Figure 5.5: Isolated tail rotor with a velocity component along Z_{Hub}

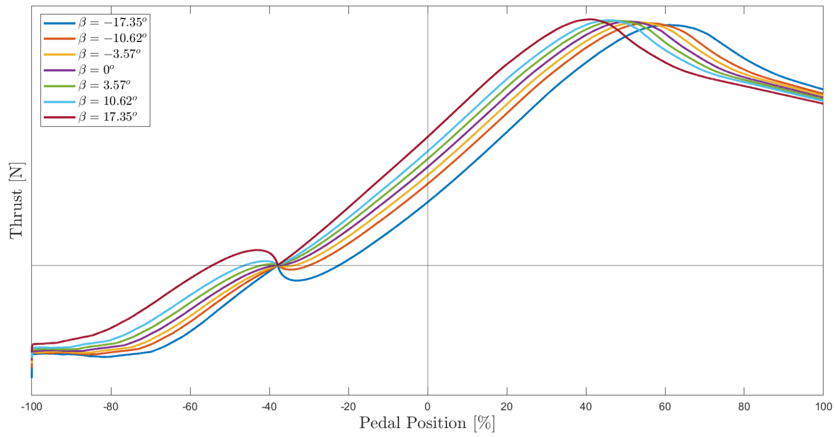

((a)) *Tail rotor thrust VS Pedal position VS* β $(U = 80\,kts)$

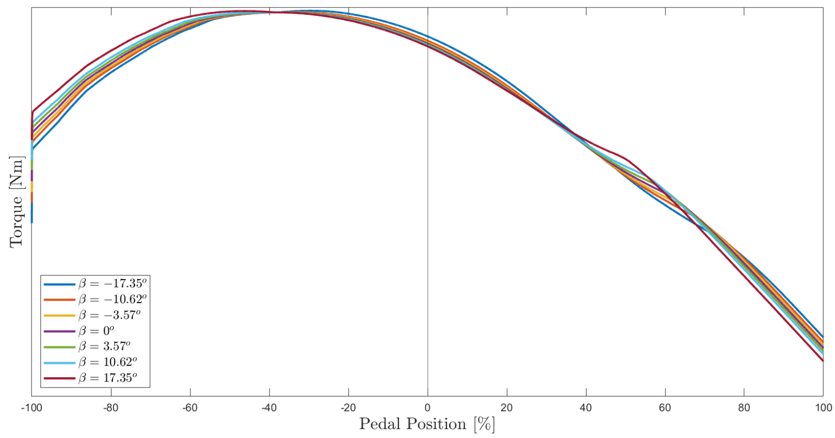

((b)) *Tail rotor torque VS Pedal position VS* β $(U = 80\,kts)$

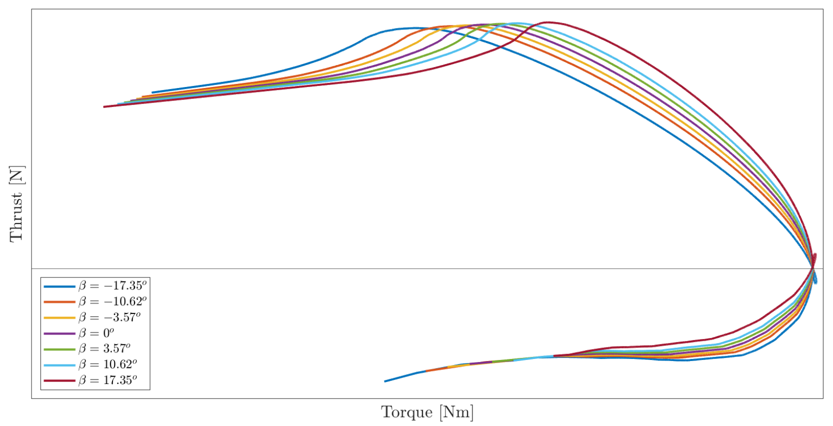

((c)) *Tail rotor thrust VS Tail rotor torque VS* β $(U = 80\,kts)$

Figure 5.6: Isolated tail rotor with velocity components along X_{Hub} and Z_{Hub}

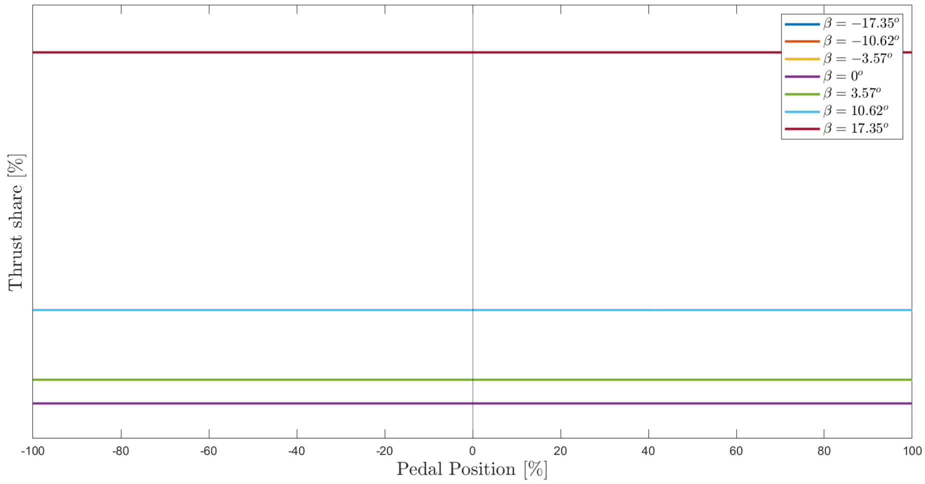

Figure 5.7: Thrust share with pedal position and external wind along X_{Hub} and Z_{Hub} $(U = 80\,kts)$

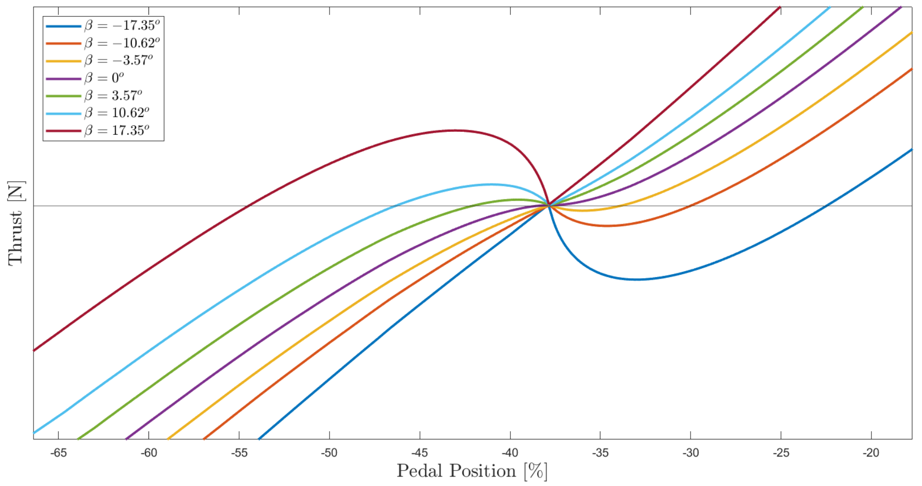

Figure 5.8: Detail of the tail rotor thrust in helicopter sideslip conditions

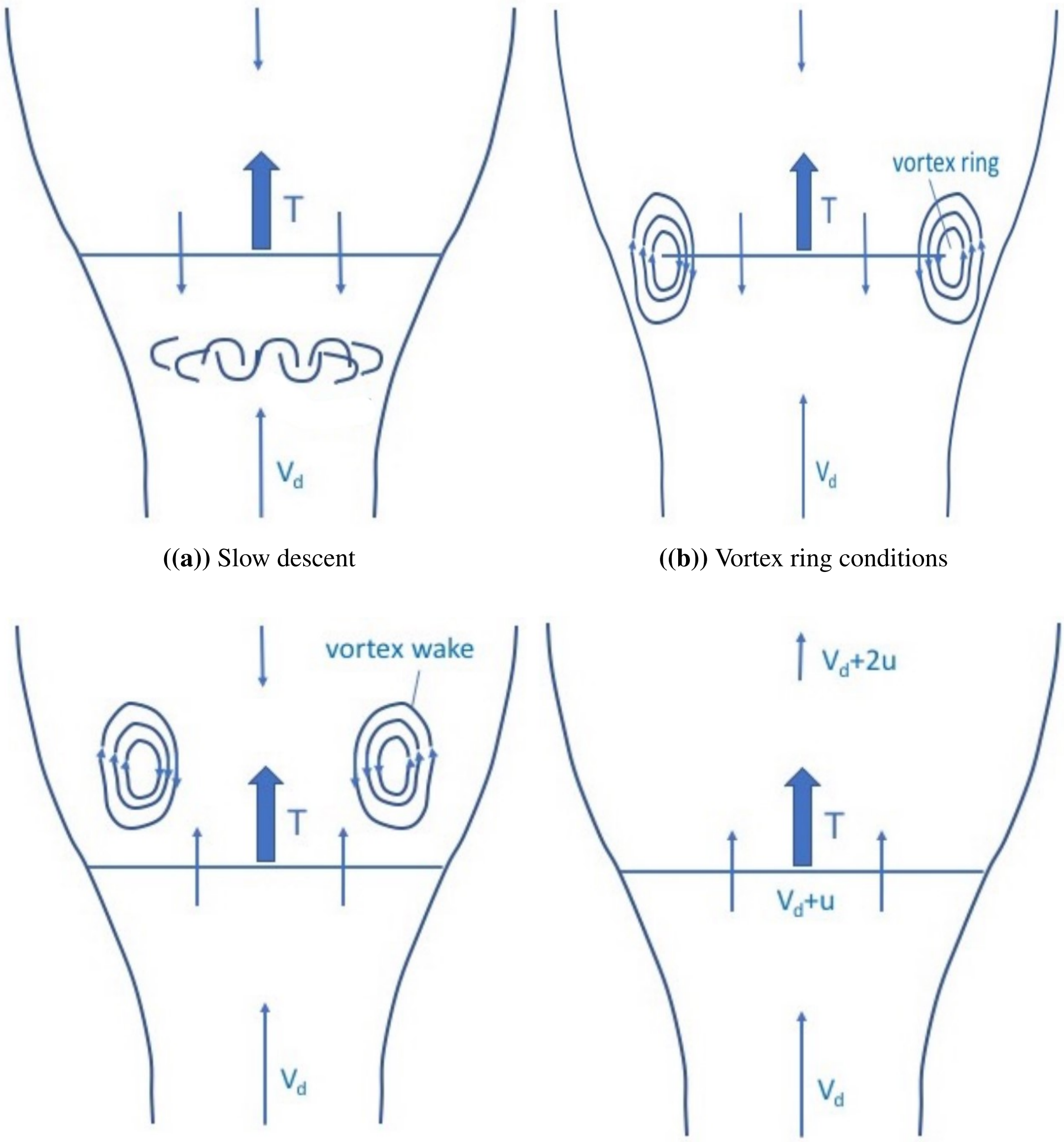

((**a**)) Slow descent ((**b**)) Vortex ring conditions

((**c**)) Moderate descent ((**d**)) Fast descent

Figure 5.9: Generic rotor behavior with the increase of the descent velocity V_d

5.2 Trim points in Hover conditions

After studying the isolated rotor, it is possible to evaluate the behavior of all the models implemented when the helicopter is in hover conditions. Since the trim points can't be evaluated because the helicopter model hasn't got the main rotor model, the results for hover conditions will be obtained with a reduced model where just the wake model, the aerodynamics surfaces, and the tail rotor are present. Appendix B presents and discusses this reduced model.

A comparison with a Flightlab model of the AW09 developed by Kopter Group has been made to validate the model. That model is quite accurate and best fits the result of some flight tests, so it will be considered as the reference for the comparison of the results.

5.2.1 Wake model results

The first result that can be studied is the wake interference on the different aerodynamic surfaces and the tail rotor.

Figures 5.11 to 5.15 compare the interference of the implemented model with the reference model. In every figure, the local flow velocity components for each element are plotted, and the helicopter velocities components with respect to the body reference frame are also shown. These values are based on 50 hover trim points evaluated by Flightlab, the reference model. For this analysis, the helicopter body frame velocities and the main rotor inflow evaluated by the reference model are given to the implemented wake model to evaluate the incremented velocities on the elements. Since the reference model doesn't evaluate a local velocity for this component, only for the tail rotor is plotted just the helicopter body frame velocity and the local interference velocity evaluated by the implemented model of the wake.

Figure 5.10 shows the wake geometry in hover conditions. It is possible to see that the tail rotor and the vertical fin are out of the main rotor wake. Thus, the implemented model doesn't evaluate a downwash on these elements. This fact can also be seen in Figure 5.12 and in Figure 5.15 where the curves of the implemented model overlap the curves of the helicopter body frame velocity. Furthermore, since the implemented wake model evaluate only a downwash whose components are parallel to the X_{BODY} and Z_{BODY} axis of the body reference frame, for each element, a velocity increment on the local Y axis never appears, and the curve of the implemented model overlaps the curve of the helicopter body frame velocity along Y_{BODY}.

Some further considerations can be made for the elements on which the wake acts. For the horizontal stabilizer (Figure 5.11), it can be seen how the W component is much more significant for the implemented model, meaning a much more intense downwash. The U component, instead, for the implemented model is higher than the body frame velocity, while the one of the reference model is lower. This fact is due to the type of wake model used: while the implemented model is simple and based on the Froude theory, the reference model uses a free wake model, which is much more complex and also evaluates the vorticity of the wake. For the airframe (Figure 5.13) and for the rotor head (Figure 5.14), the U component of the implemented model is always smaller than the one of the reference model. In contrast, the W component of the airframe for the implemented model is slightly above the reference model. The W component for the rotor head is, instead, comparable for both models.

5.2.2 Loads results

After studying the wake interference on the helicopter parts, it's possible to analyze the loads produced by these parts in hover conditions.

Figures 5.16 to 5.23 show the forces and moments generated by every element, expressed in components along the body reference frame X_{BODY}, Y_{BODY} and Z_{BODY}. For each plot, on the x-axis there are the same trim cases in hover evaluated by Flightlab, the reference model. From the figures, it can be seen that a general error between the implemented model and the reference model is always present, and that is due mainly to the different wake models. However, it must be noted that the errors have been evaluated as follows:

$$err_F\% = \frac{[ReferenceModel] - [ImplementedModel]}{Weight} \cdot 100 \qquad \text{for the Forces}$$

$$err_M\% = \frac{[ReferenceModel] - [ImplementedModel]}{Weight \cdot d_{TR}} \cdot 100 \qquad \text{for the Moments}$$

Where $Weight$ is the helicopter weight and d_{TR} is the distance between the tail rotor and the aircraft's center of gravity.

In hover conditions, some loads are close to 0 so it is not strange to see very low errors for some components like, for instance, the vertical fin (Figure 5.17): this component doesn't produce any significant force in hover conditions so the errors are low because the value of the forces produced is very low if compared to the aircraft weight.

From the chart that shows the overall forces generated by the aerodynamic surfaces (Figure 5.20), it can be seen that a significant error appears in the force along Z_{BODY}. This error is not negligible and is also the cause of some discrepancies in the pitch moment M_Y evaluated by the implemented and the reference models (Figure 5.21). This error on the force along Z_{BODY} is related to the difference in the W component of the downwash on the airframe shown in Figure 5.13, which affects the overall behavior of the model considerably. The airframe, in fact, is the only component that presents an error higher than 1%.

For the tail rotor, there are also some errors, as can be seen from Figure 5.22 and 5.23: the main tail rotor force that is developed along Y_{BODY} axis evaluated by the implemented model don't overlap correctly the force along the same axis evaluated by the reference model, and that's a source of errors for the roll moment MX but most importantly for the yaw moment MZ. The forces evaluated along X_{BODY} and Z_{BODY} are instead very similar and comparable.

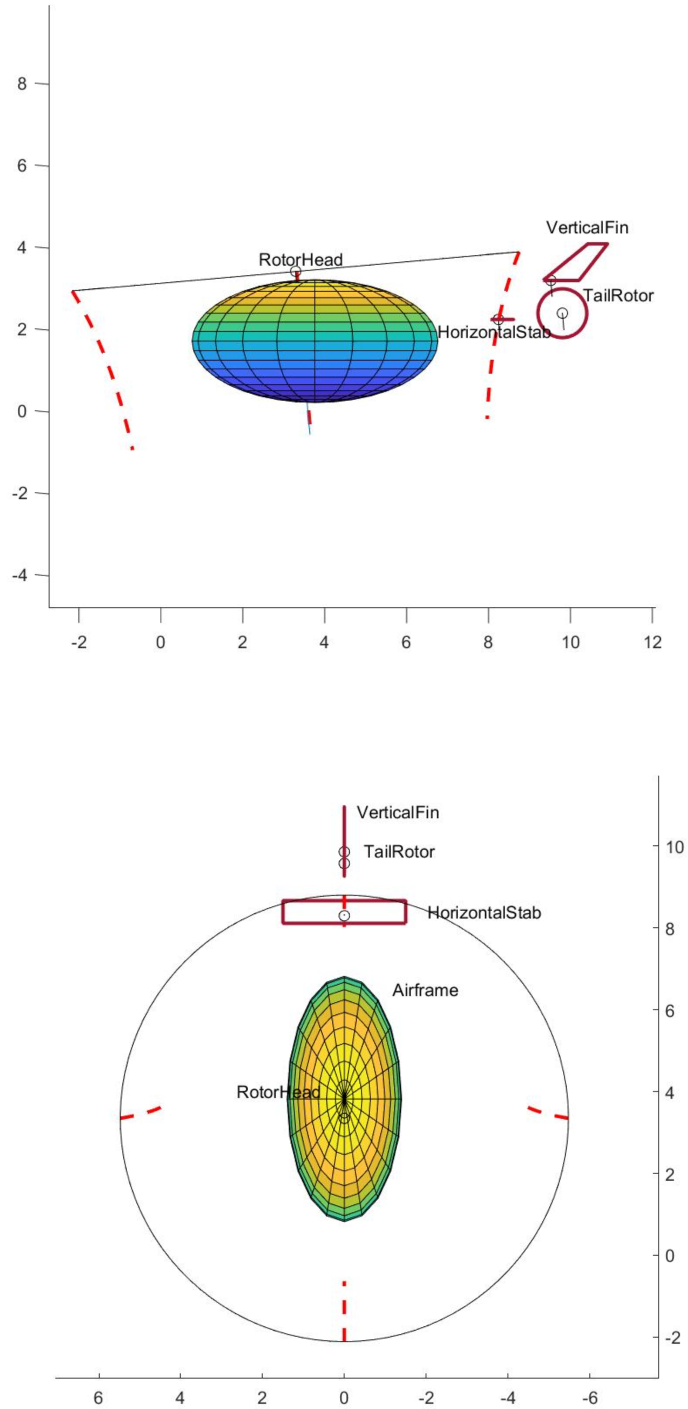

Figure 5.10: Wake geometry in hover conditions

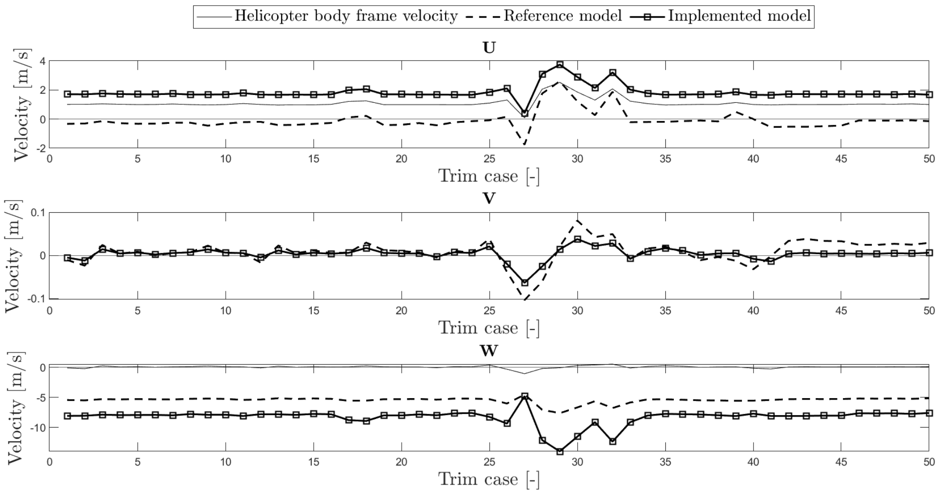

Figure 5.11: Wake interference on the horizontal stabilizer in hover

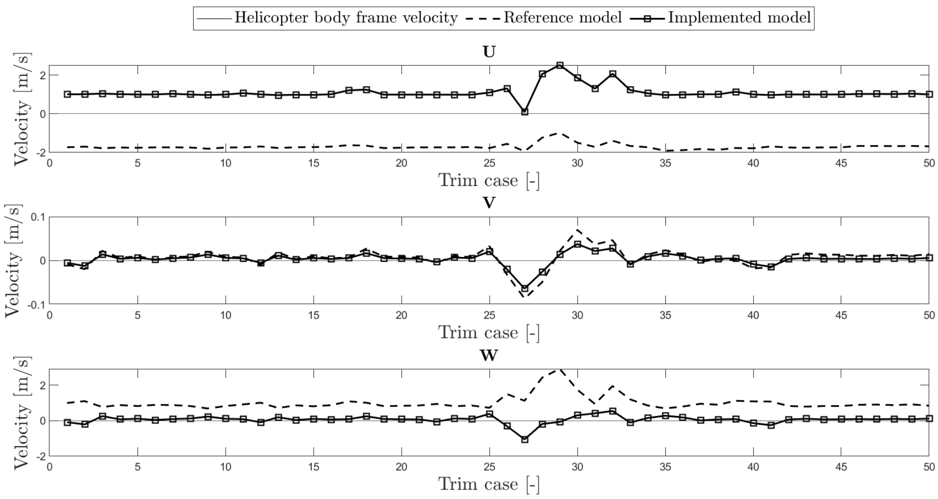

Figure 5.12: Wake interference on the vertical fin in hover

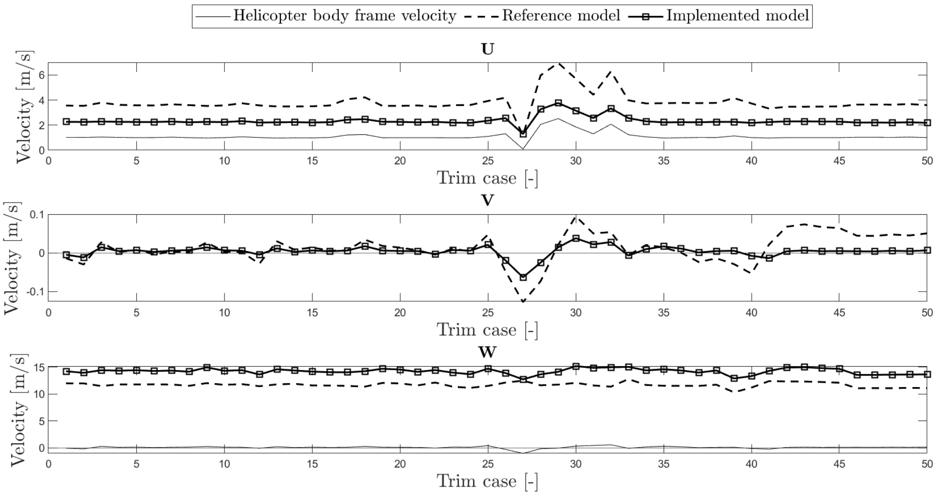

Figure 5.13: Wake interference on the airframe in hover

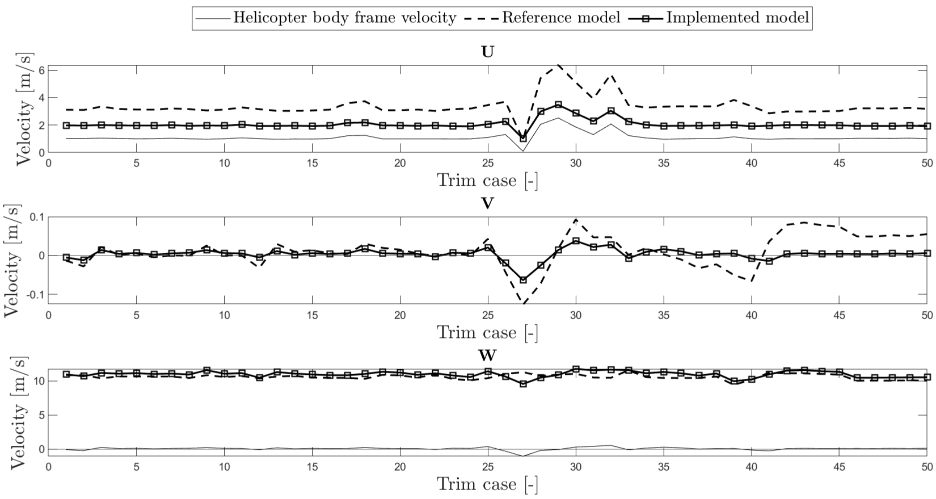

Figure 5.14: Wake interference on the rotor head in hover

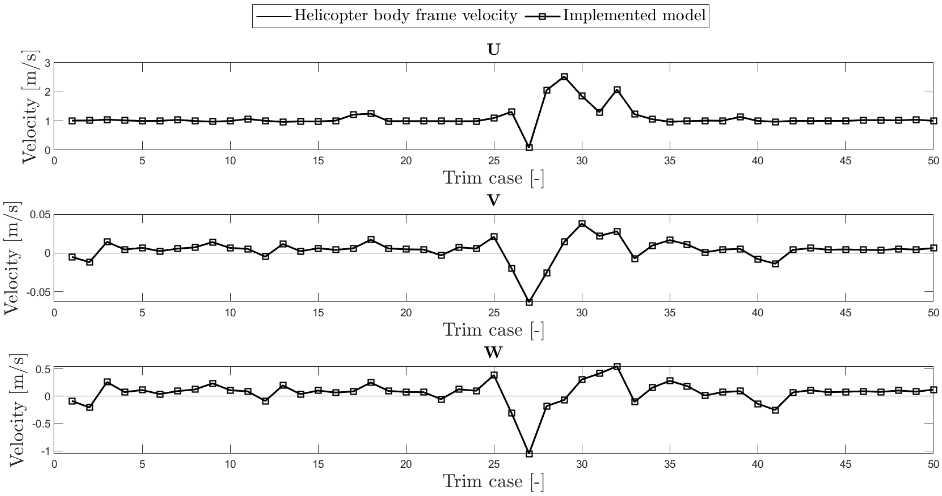

Figure 5.15: Wake interference on the tail rotor in hover

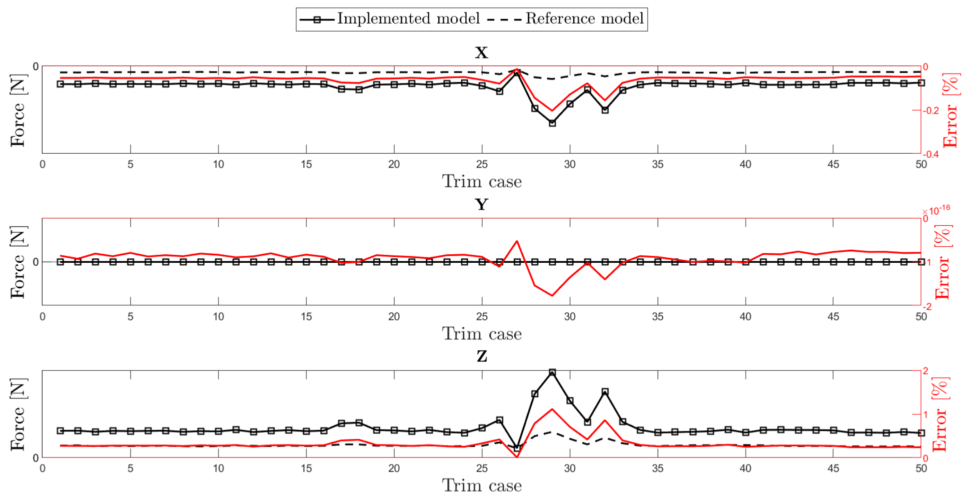

Figure 5.16: Forces produced by horizontal stabilizer in hover

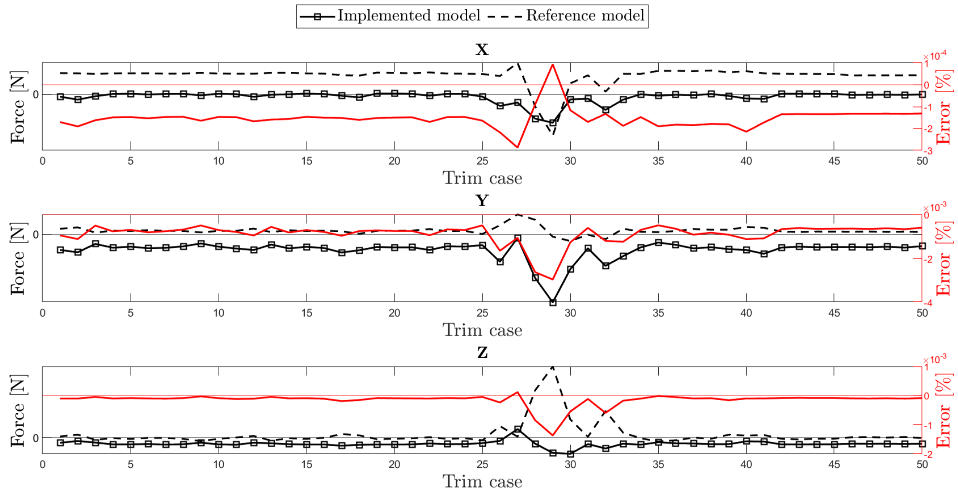

Figure 5.17: Forces produced by vertical fin in hover

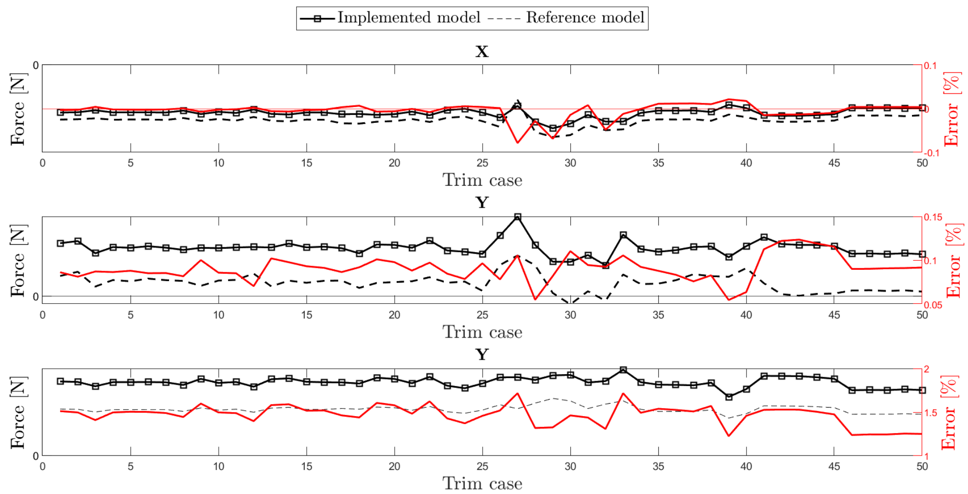

Figure 5.18: Forces produced by airframe in hover

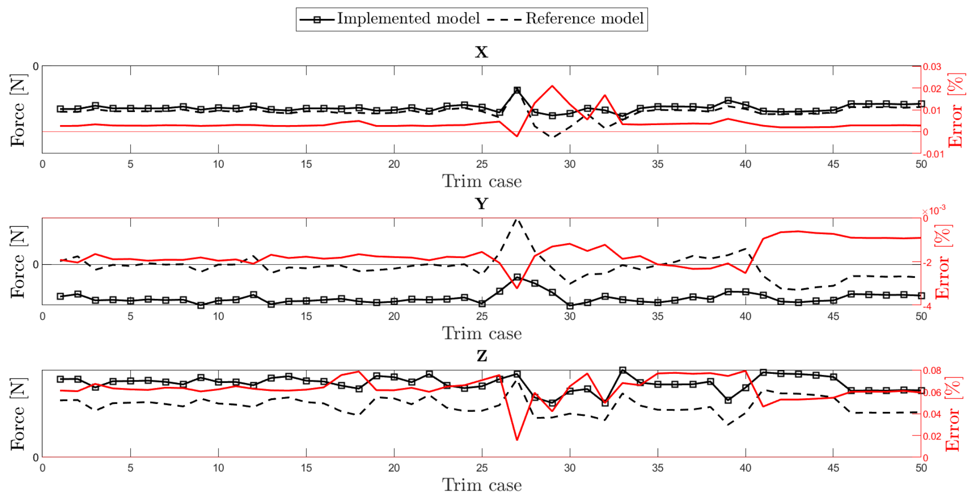

Figure 5.19: Forces produced by rotor head in hover

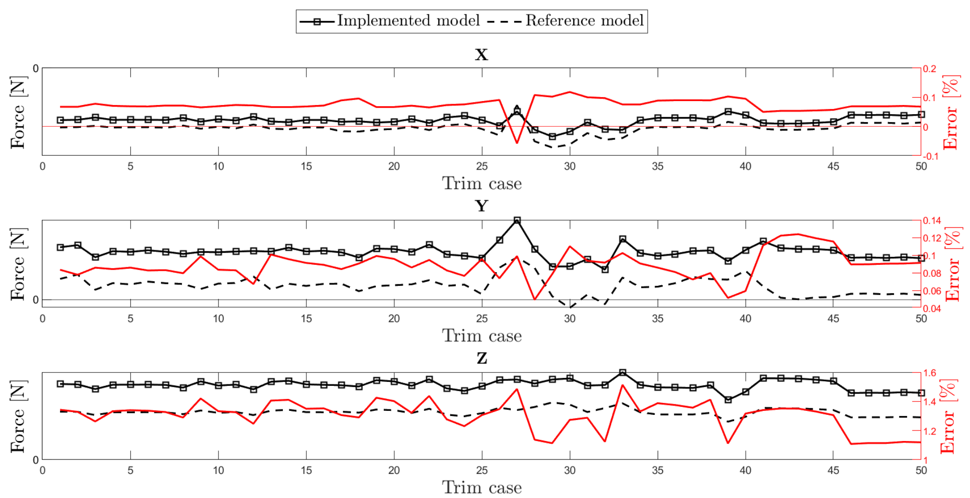

Figure 5.20: Forces produced by every aerodynamic surface in hover

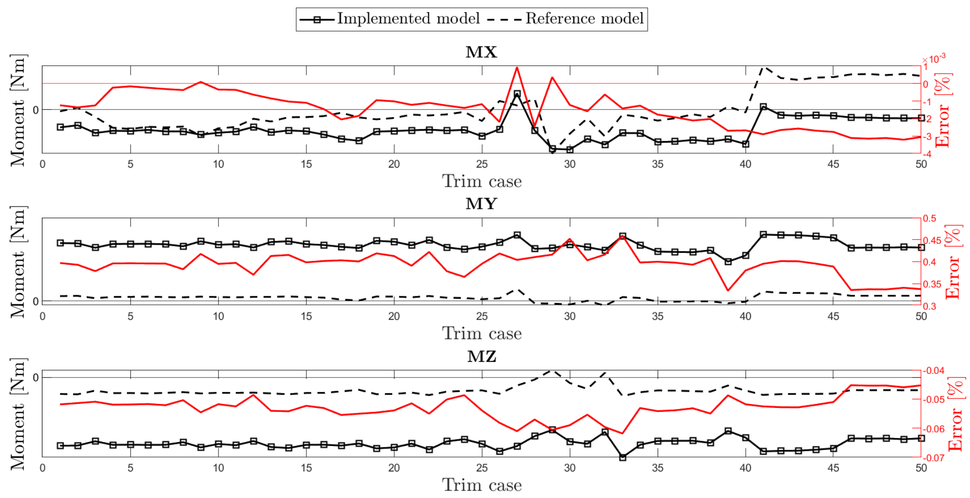

Figure 5.21: Moments produced by every aerodynamic surface in hover

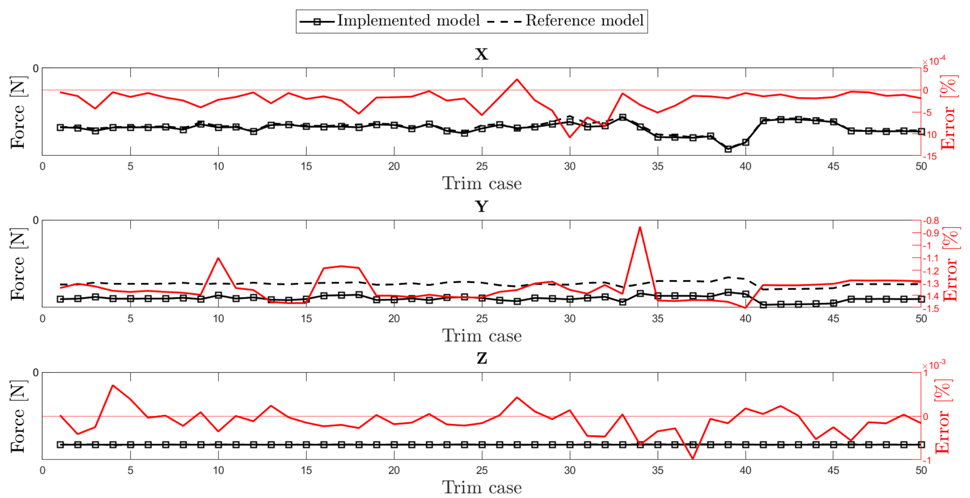

Figure 5.22: Forces produced by tail rotor in hover

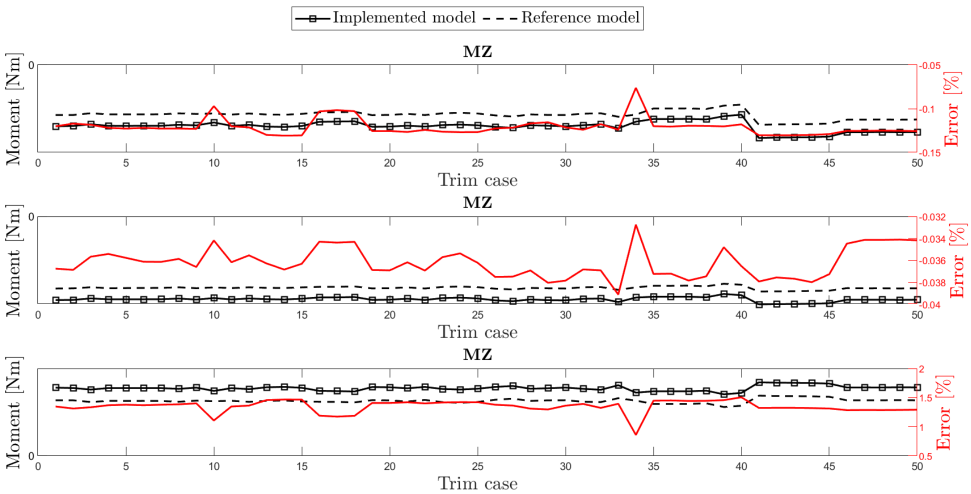

Figure 5.23: Moments produced by tail rotor in hover

5.3 Trim points in Forward flight condition

The latest results that are possible to show are related to the behavior of all the models implemented when the helicopter is in forward flight conditions. As in the previous section, since the trim points can't be evaluated because the helicopter model hasn't got the main rotor model, the results are obtained with the reduced model already introduced and further discussed in Appendix B, where there are just the wake, the aerodynamics surfaces, and the tail rotor models.

As before, a comparison with the Flightlab model of the AW09 developed by Kopter Group has been made to validate the model.

5.3.1 Wake model results

The interference generated by the wake in forward flight relies on several factors because the wake geometry depends on the helicopter velocity and the performance of the main rotor.

Figures 5.24 to 5.28 show the flow velocities on the elements influenced by the wake. In every figure, the local flow velocity components on each element are plotted, and the helicopter velocities components with respect to the body reference frame are also shown. These values are based on 50 trim points in forward flight evaluated by Flightlab, the reference model. These trim points are evaluated at speeds (CAS) between 40 and 120 *knots*. For this analysis, the helicopter body frame velocities and the main rotor inflow evaluated by the reference model are given to the implemented wake model to evaluate the flow velocities on the elements. Only for the tail rotor, since the reference model doesn't evaluate a local velocity for this component, the helicopter body frame velocity and the local interference velocity evaluated by the implemented model of the wake are plotted.

Differently from the hover condition, it can be seen that the wake influences every component. The overall velocities trend of the implemented wake model follows well enough the trend of the reference model. For the last trim cases, where the helicopter velocity is close to 120 *knots*, there are some errors, mainly on the velocity W along the Z axis. Right for this axis a strange behavior can be seen for the vertical fin, rotor head, and airframe components: for high helicopter velocities, the trend of the local velocity evaluated by the implemented model seems to be opposite to the one evaluated by the reference model. Some discrepancies also appear for the first trim points where the velocity is close to 40 *knots*, for the U component along the X axis.

5.3.2 Loads results

Finally, it's possible to analyze the loads produced by the modeled helicopter parts in forward flight conditions.

Figures 5.29 to 5.36 show the forces and moments generated by every element, expressed in components along the body reference frame X_{BODY}, Y_{BODY} and Z_{BODY}. On the x-axis there are the same trim cases evaluated by Flightlab in forward flight conditions. The figures show good accuracy, especially for the rotor head, the vertical fin, and the tail rotor. It must be noted that in hover conditions, the aerodynamic forces are minimal since the air flowing on the surfaces is due to the main rotor wake (even if the trim point evaluated by Flightlab considers anyway a very small helicopter velocity). In forward flight, instead, the forces, especially along the X_{BODY} axis and Z_{BODY} axis, are not negligible. Some significant errors appear for some conditions, but they are due to the high value of the force. Considering the force component along the X_{BODY} axis developed by the airframe (Figure 5.31), it can be seen that the error is higher than 5%. Still, since the force is very high and considering that the error doesn't evaluate a proper relative error but only an absolute error normalized, it can be understood that the error is minor.

From the chart that shows the overall forces generated by the aerodynamic surfaces (Figure 5.33), it can be seen that the main aerodynamic forces along X_{BODY} and Z_{BODY} evaluated by the implemented model overlap almost perfectly those evaluated by the reference model. A maximum error of about 1% is present for some trim cases for the forces along Y_{BODY} and Z_{BODY}. For the force component along X_{BODY} it can be seen how there isn't the influence of the airframe where the error evaluated was higher than 5%. Also, the moments (Figure 5.34) evaluated by the implemented model are closer to those calculated by the reference model, even though a small error remains. For the tail rotor, as can be seen from Figure 5.35 and 5.36, the implemented model follows the reference model perfectly in both the forces and moments produced and the errors are much more minimal. Especially for the main force developed by the tail rotor, the one along Y_{BODY}, it can be seen as the error is contained in a range between -0.1% and 0.2%

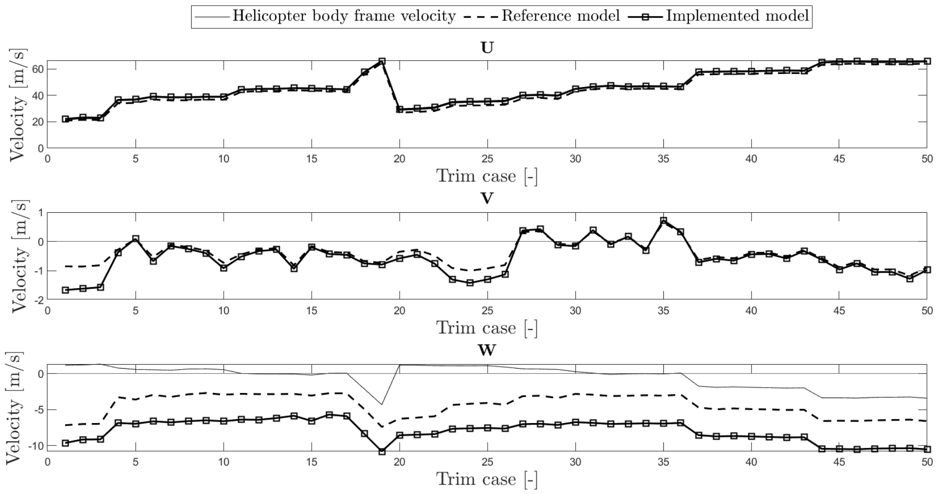

Figure 5.24: Wake interference on the horizontal stabilizer in forward flight

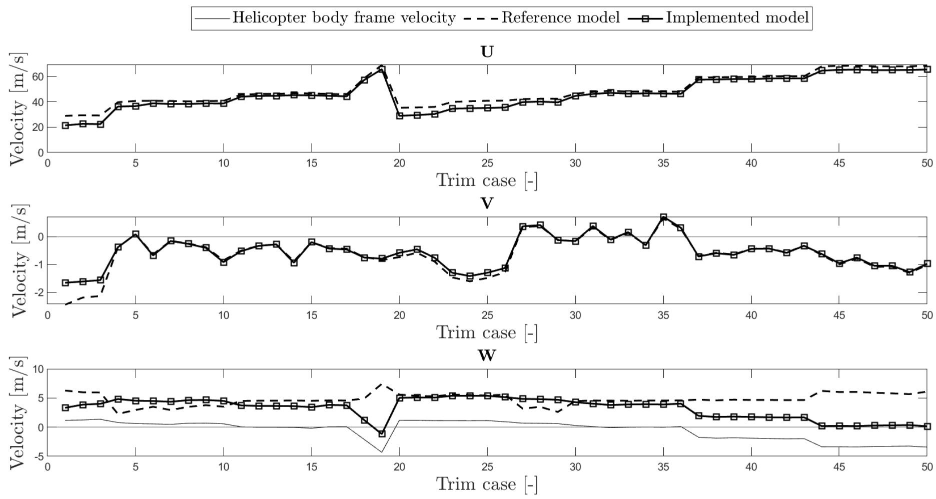

Figure 5.25: Wake interference on the vertical fin in forward flight

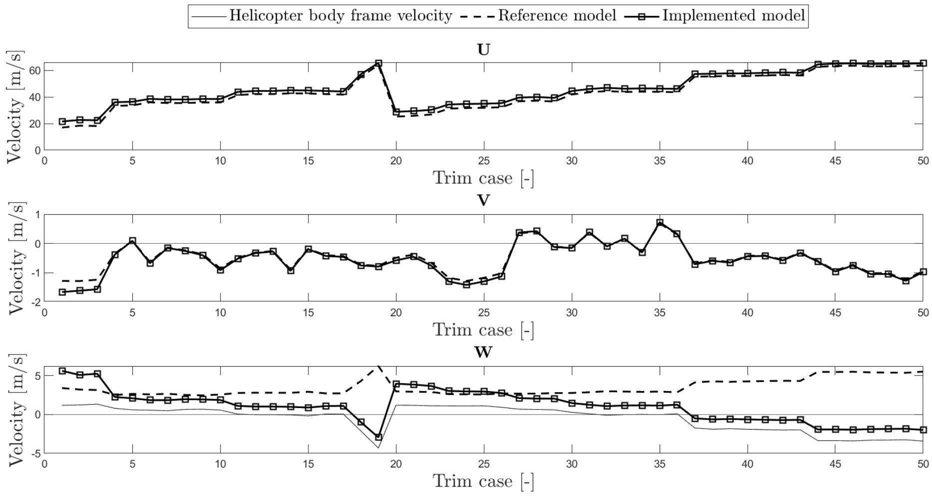

Figure 5.26: Wake interference on the airframe in forward flight

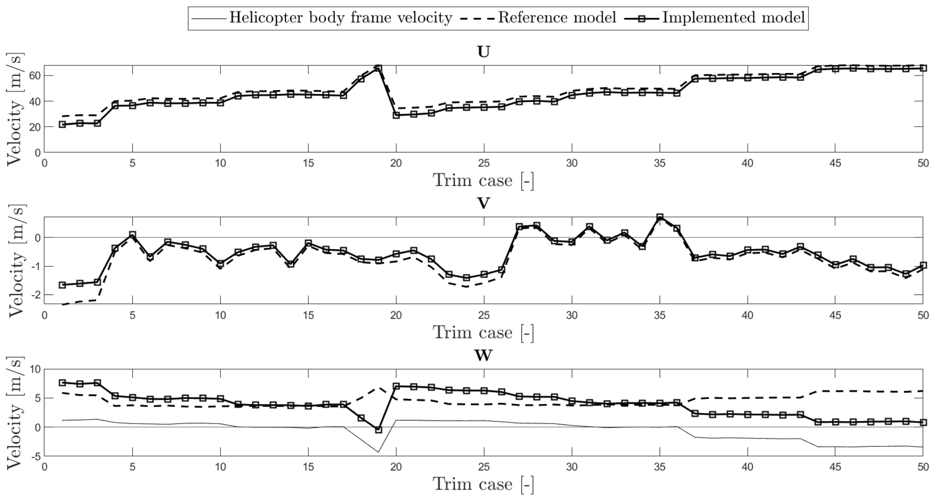

Figure 5.27: Wake interference on the rotor head in forward flight

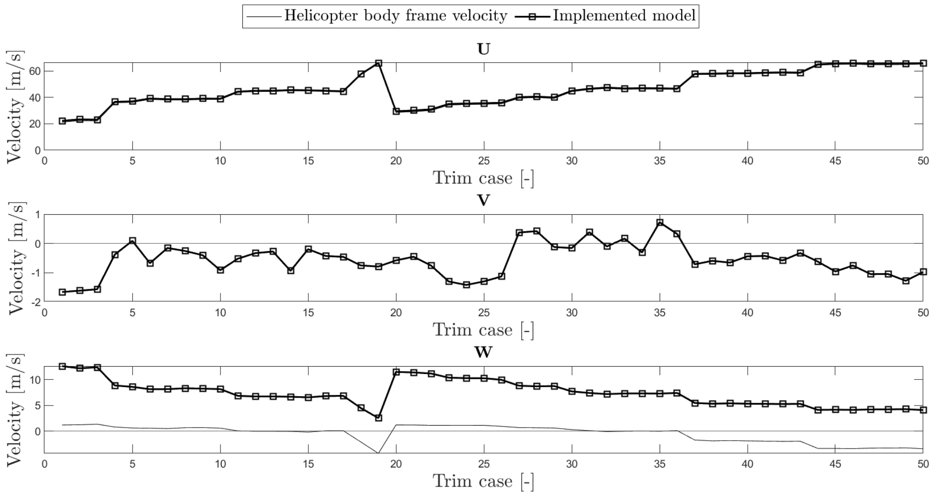

Figure 5.28: Wake interference on the tail rotor in forward flight

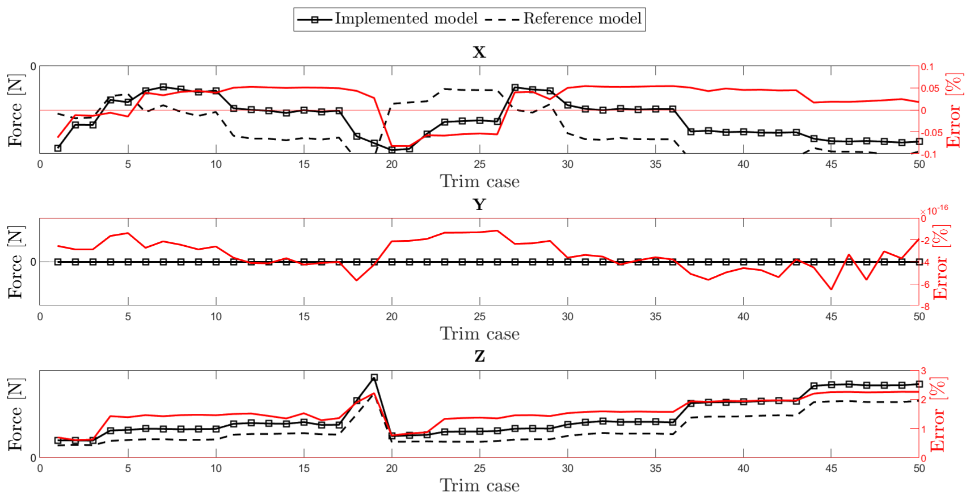

Figure 5.29: Forces produced by horizontal stabilizer in forward flight

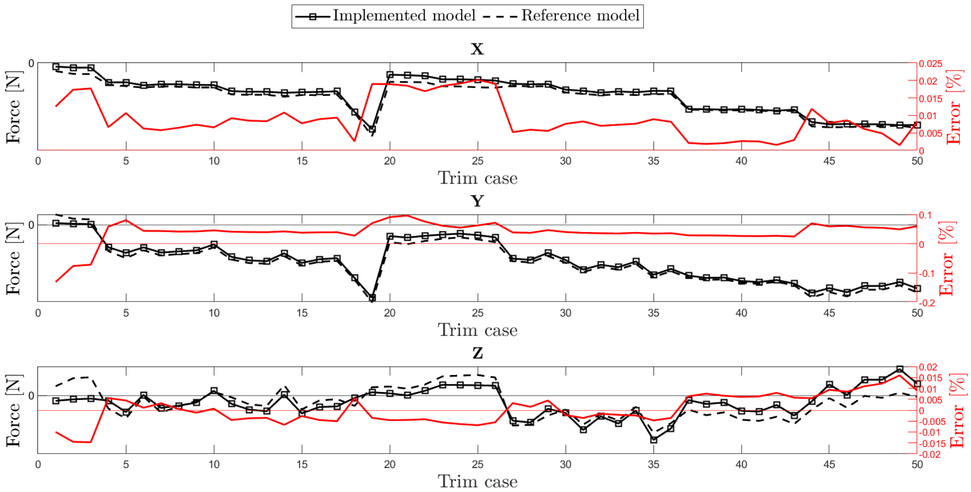

Figure 5.30: Forces produced by vertical fin in forward flight

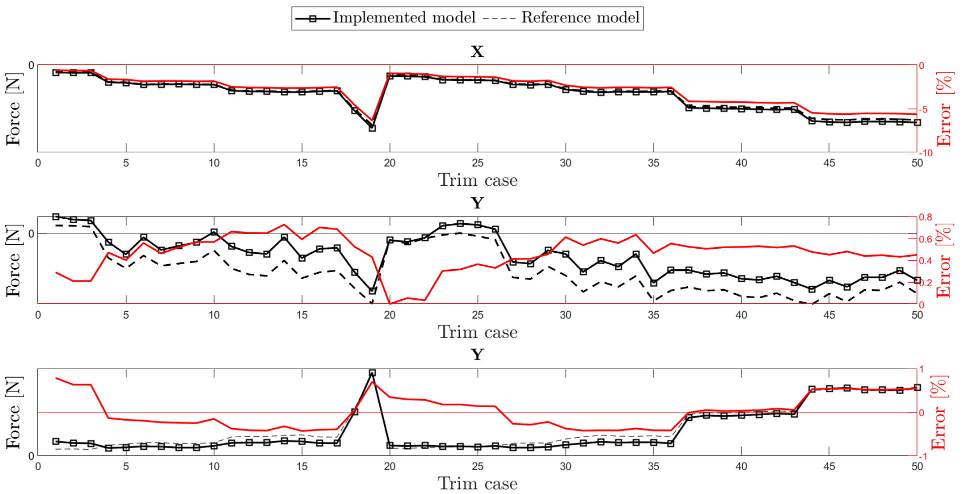

Figure 5.31: Forces produced by airframe in forward flight

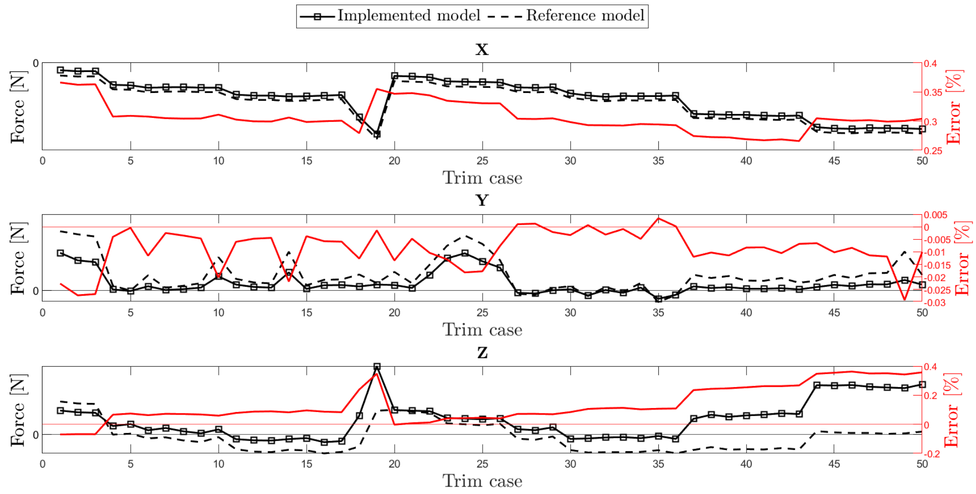

Figure 5.32: Forces produced by rotor head in forward flight

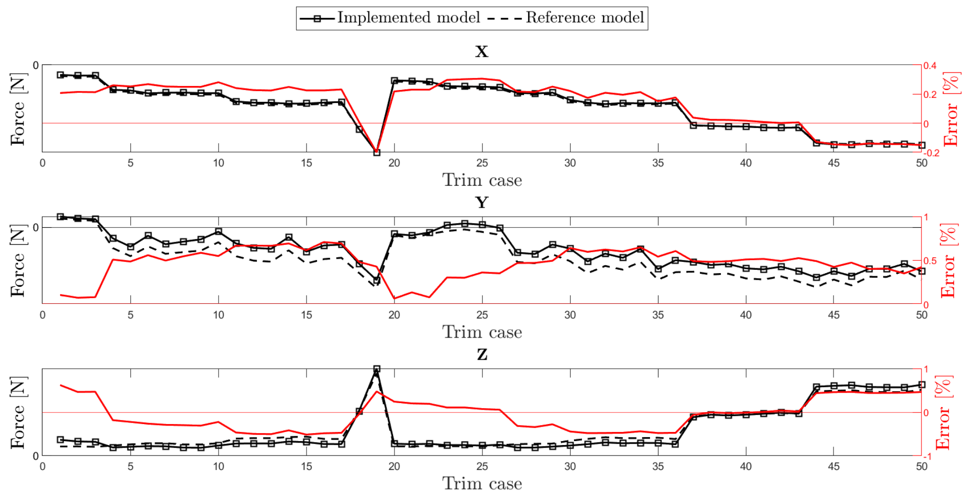

Figure 5.33: Forces produced by every aerodynamic surface in forward flight

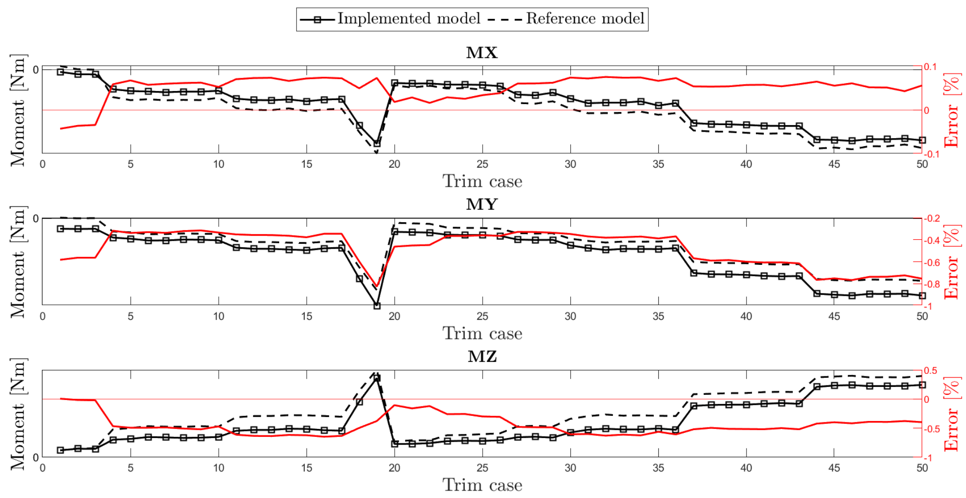

Figure 5.34: Moments produced by every aerodynamic surface in forward flight

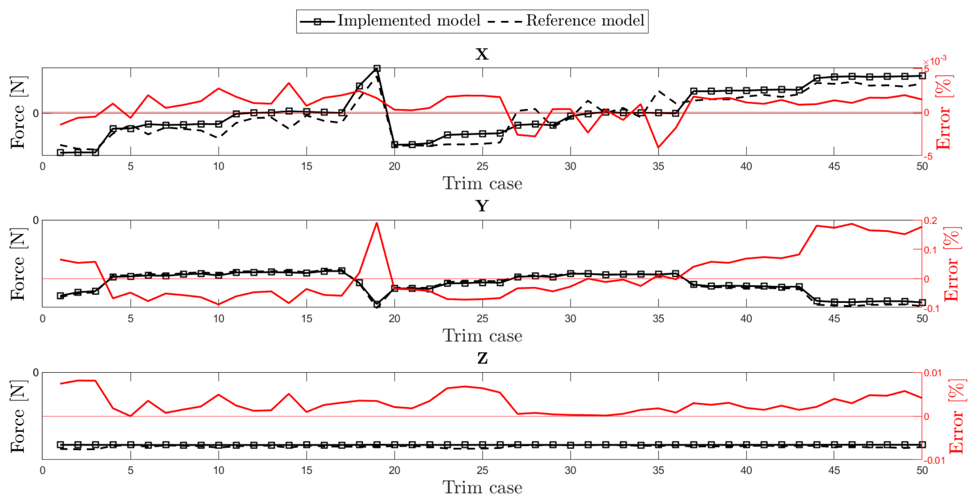

Figure 5.35: Forces produced by tail rotor in forward flight

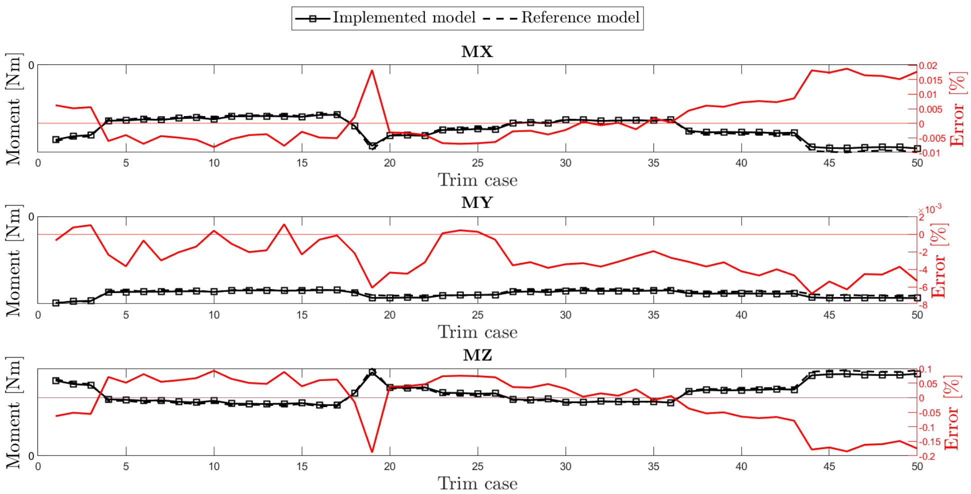

Figure 5.36: Moments produced by tail rotor in forward flight

Conclusions

The work carried out by the author led to the development of models for several helicopter components, in particular, the ducted tail rotor, the airframe, the horizontal stabilizer, the vertical fin, the main rotor head, and the wake of the main rotor. The models have also been integrated into an overall helicopter model that represents the core of the helicopter flight simulation.

The results obtained by comparing the implemented and reference models developed in the Flightlab environment generally demonstrate acceptable accuracy. In particular, the tail rotor model reflects the main result obtained by the bench test, reference model, and flight test, especially in forward flight conditions. Also, the solution for the main rotor wake model, even though simple, successfully represents the interference that the main rotor produces, especially during the forward flight with helicopter velocities contained between 50 and 100 $knots$.

Some further improvements of the models that exceed the scope of this thesis can be highlighted in order to set the future steps for an enhancement of the overall helicopter model:

- The tail rotor model implemented ignores the effect of the vortex ring generation when an external velocity is opposite to the induced velocity. Since this is a situation that can occur during normal flight activities, some further investigation must be made.

- The wake model can be improved considering the vorticity effect of the wake but always considering that the model developed must be used in a real-time simulation.

- The results in hover conditions present the most significant errors. These errors are probably due to the wake model differences, but some investigation must be made to understand the source of these errors better.

Appendix A

Reference Frames

In this appendix are reported all the reference frames of the modeled components.

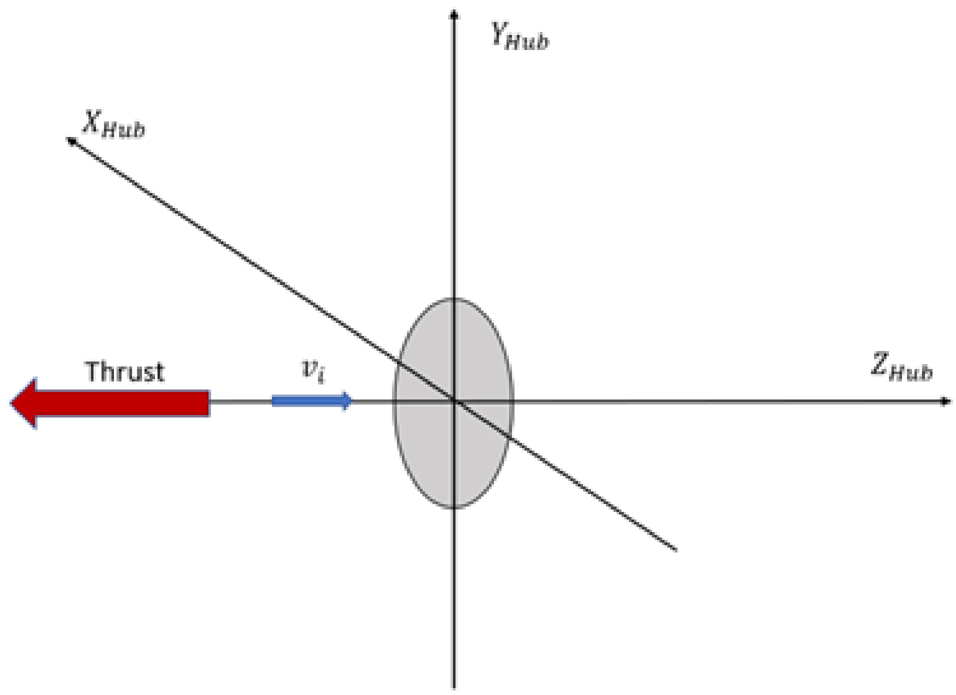

Figure A.1: Tail rotor reference frame

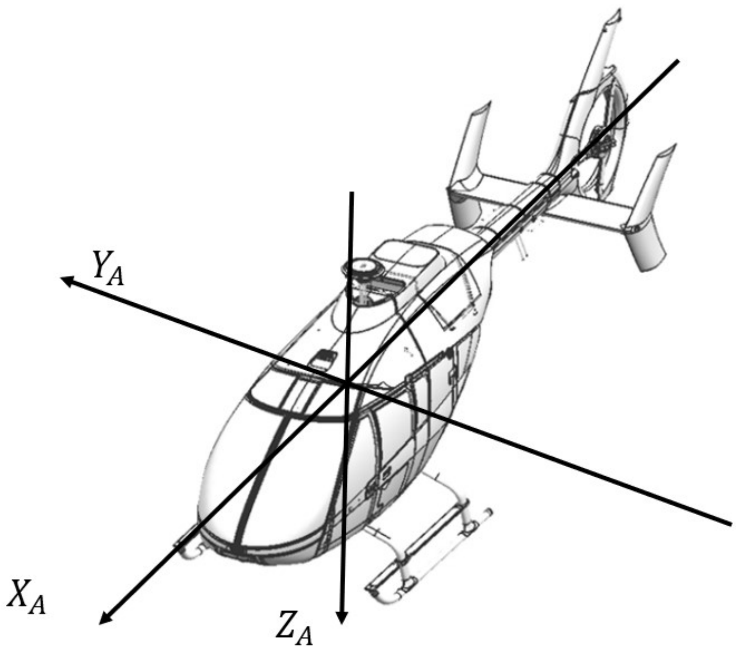

Figure A.2: Airframe reference frame

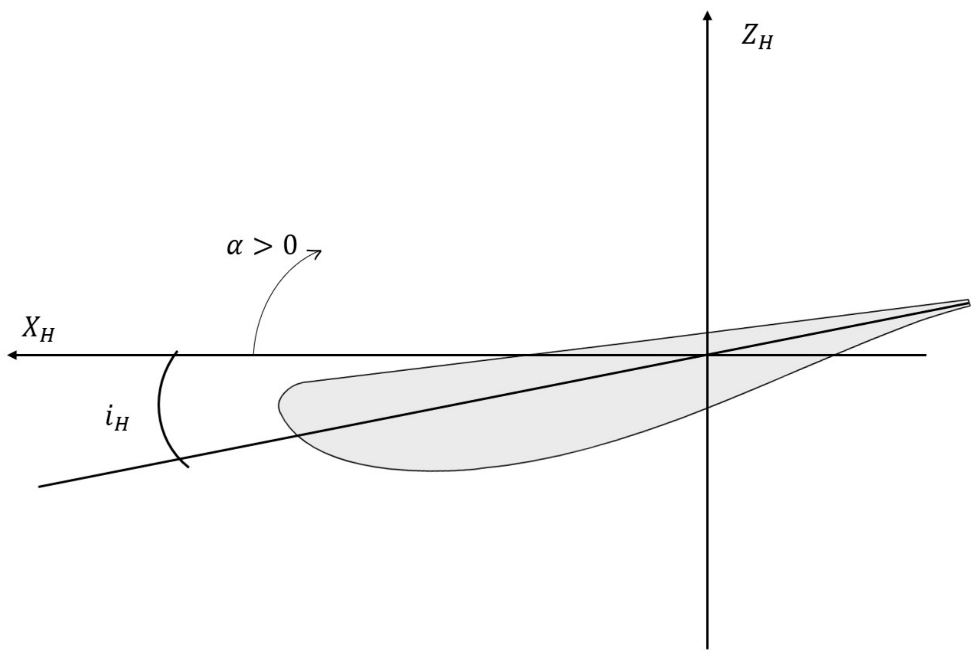

Figure A.3: Horizontal stabilizer reference frame

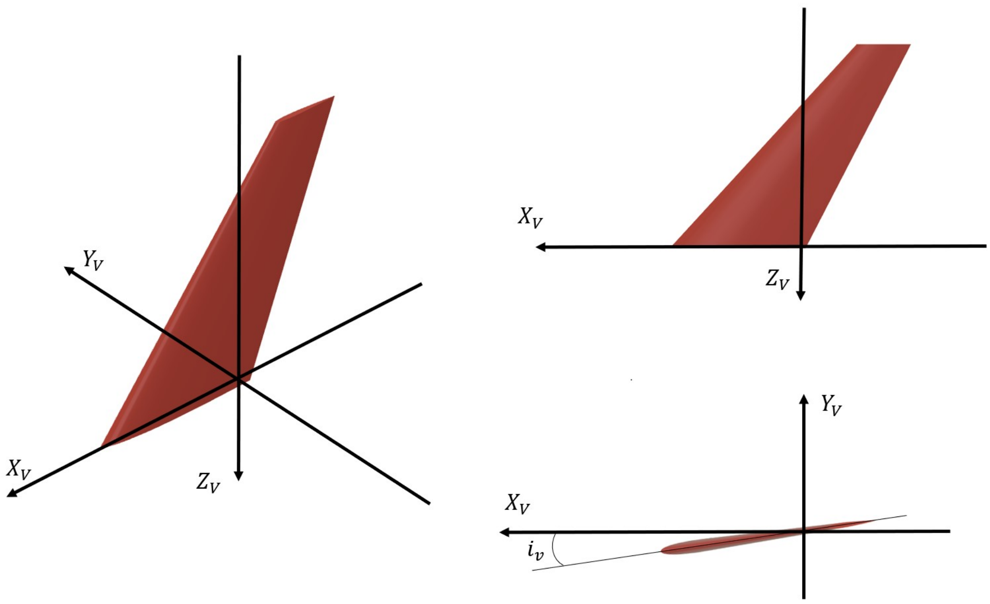

Figure A.4: Vertical fin reference frame

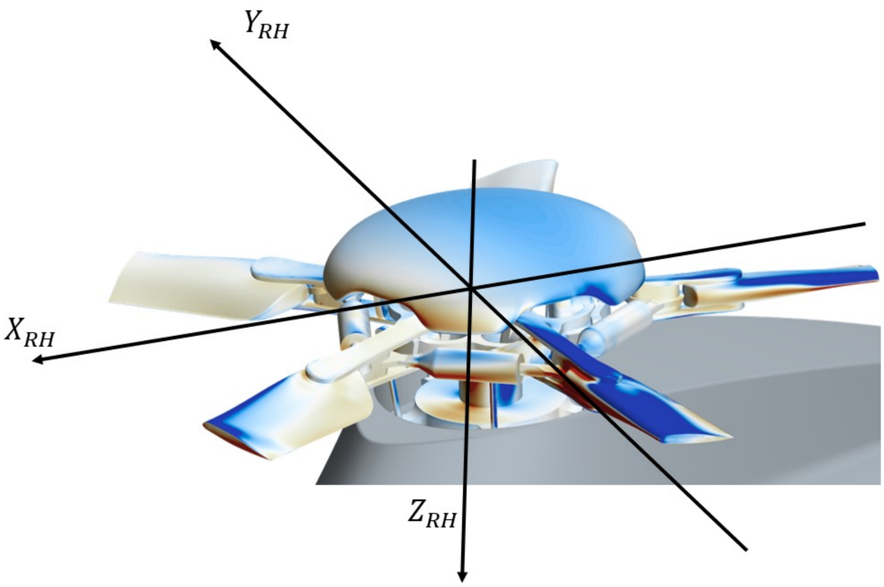

Figure A.5: Rotor head reference frame

Appendix B

Reduced helicopter model

To obtain some results from the implemented models for validation, an ad-hoc model has been developed, omitting the models that were not part of this thesis work.

This model is presented in Figure B.1, and as it can be seen, it does not include most of the blocks seen in the overall helicopter scheme of Figure 4.1. The *Main rotor* block is present, but it only contains a block for evaluating the local velocities at the rotor hub, and the *Wake* block developed.

The reduced helicopter model is not stand-alone but needs some input to work. All the inputs are taken from the Flightlab model of the AW09 developed by Kopter Group, indicated in the text as the reference model. This reference model is quite accurate and best fits the result of some flight tests, so it is considered the best reference for the validation. Taking the inputs from the Flightlab model represents an advantage since it is possible to compare the reference model results and the implemented model results starting from the same initial condition.

The output of this reduced model are the results that need to be compared in order to validate the developed models: thus, the main outputs are the tail rotor loads and the aerodynamic loads, but from this model also, the wake-induced velocity on the components are extracted to compare and validate the wake results between the reference and developed model.

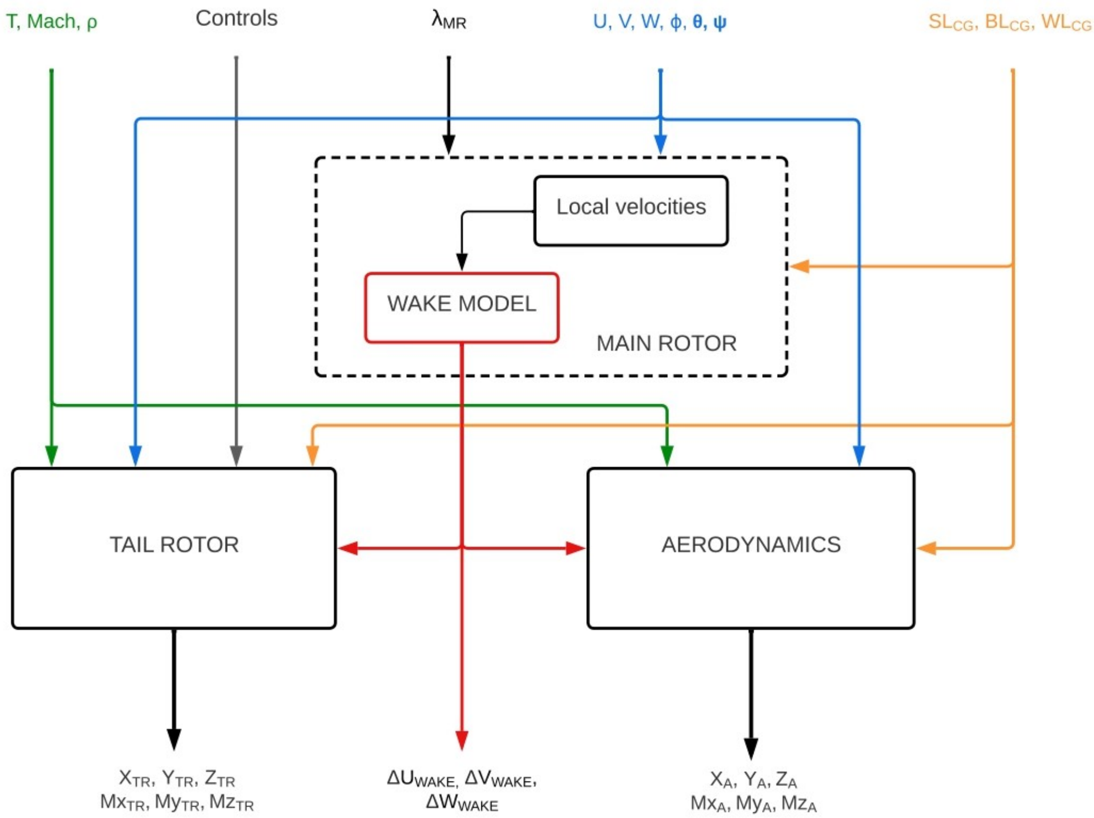

Figure B.1: Scheme of the reduced model used for validation

Bibliography

[1] Anna Abà. “Implementation of a comprehensive real-time simulation model of a tilt-rotor aircraft”. Politecnico di Torino, 2020.

[2] Kopter Group AG. *The Hybrid Helicopter Kopter’s Approach to Modern Flight*. Company Presentation. Apr. 2021.

[3] Federico Barra. “Development of a tilt-rotor model for real-time flight simulation”. In: *Proc. 15th PEGASUS Student Conference (Glasgow, UK, April 2019)*. 2019.

[4] Pierre-Marie Basset and M Brocard. “A fenestron model for improving the helicopter yaw dynamics flight simulation”. In: *30 th European Rotorcraft Forum*. 2004.

[5] Boris N Bourtsev. “Fan-in-fin performance at hover computational method”. In: *Proc. 26th European Rotorcraft Forum*. 2000.

[6] Mark E Dreier. *Introduction to helicopter and tiltrotor flight simulation*. American Institute of Aeronautics and Astronautics, 2007.

[7] Rémy Huot. *Improving the modeling of the Fenestron® in the Eurocopter Simulation Tool*. 2013.

[8] Wayne Johnson. *Helicopter theory*. Courier Corporation, 2012.

[9] Dale M Pitt and Peters A David. “Theoretical prediction of dynamic inflow derivatives”. In: *Vertica* 5 (1981).

[10] A Vuillet and F Morelli. “New aerodynamic design of the Fenestron for improved performance”. In: *12th European Rotorcraft Forum* (1987).

Websites

[11] *Airbus Flightlab Helicopter*. [Online]. URL: https://www.airbus.com/en/newsroom/press-releases/2021-01-airbus-unveils-its-helicopter-flightlab-to-test-tomorrows.

[12] *Kopter Group*. [Online]. URL: https://koptergroup.com/.

[13] *Leonardo Unmanned*. [Online]. URL: https://unmanned.leonardo.com/it/products/awhero.

[14] *Lilium Aviation*. [Online]. URL: https://lilium.com/.

[15] *Mars Helicopter*. [Online]. URL: https://mars.nasa.gov/technology/helicopter/.